Highly Spin-Polarised Chiral Transition Metal Silicide Epilayers

Priyasmita Sinha
School of Physics and Astronomy
University of Leeds

Submitted in accordance with the requirements for the degree of

Doctor of Philosophy

October 2015

Intellectual Property Statement

The candidate confirms that the work submitted is his/her own, except where work which has formed part of jointly authored publications has been included. The contribution of the candidate and the other authors to this work has been explicitly indicated below. The candidate confirms that appropriate credit has been given within the thesis where reference has been made to the work of others.

Work from the following jointly authored publication is presented in chapter one, three, four, five and six of this thesis:
P. Sinha, N. A. Porter, and C. H. Marrows. Strain-induced effects on the magnetic and electronic properties of epitaxial $Fe_{1-x}Co_xSi$ thin films. *Phys. Rev. B* **89**, 134426 (2014). **Work attributable to candidate:** $Fe_{1-x}Co_xSi$ thin films of varying Co doping were grown and characterised using XRD, LEED, and AFM by P. Sinha. She also carried out the strain characterisation, analysis of transport measurements, magnetometry, and the corresponding analysis of spin polarisation in the thin films. The manuscript was written by P. Sinha. **Work attributable to others:** Transport

measurements and TEM were jointly carried out with Dr. N.A. Porter. Dr. N.A. Porter also did the TEM analysis. Prof. Chris Marrows contributed to the overall discussion and edited the manuscript.

M. B. Ward, N. A. Porter, P. Sinha, R. Brydson, and C. H. Marrows. Preparation of plan-view Co-doped FeSi thin film TEM specimens using FIB. *Journal of Physics: Conference Series* **522**, 012044 (2014). **Work attributable to candidate:** Sample growth, characterisation. **Work attributable to others:** FIB was carried out by Dr. M.B. Ward. TEM and EDX were jointly carried out by Dr. M.B. Ward and Dr. N.A. Porter. Dr. M.B. Ward wrote the manuscript. Prof. R. Brydson and Prof. C.H. Marrows contributed to the overall discussion and analysis.

Acknowledgements

First and foremost, I would like to express my deep gratitude to my thesis advisor Prof. Chris Marrows for his constant guidance, support, encouragement, and understanding throughout the research work. Thanks for providing me the opportunities to work and interact with various researchers in various labs across the world. I am grateful to my co-advisor Dr. Gavin Burnell for his valuable inputs, incisive observations, time, patience, and enthusiasm which has helped me to improve the quality of my research work. With immense pleasure, I thank Prof. Bryan Hickey for pushing me out of my comfort zone and always prodding me to learn new things. I would also like to thank Dr. Tom Moore and Dr. Oscar Cespedes for their valuable research inputs from time to time. Thanks also to Mrs. Glenys Bowles for helping me to walk through the maze of administrative requirements.

Many thanks to Dr. Nick Porter and Dr. Mannan Ali, their help has been invaluable. Thanks to Late Phil Cale and John Turton for excellent upkeep of the cryogenics and making them available for carrying out experiments at short notice. I also thank my undergraduate research supervisors in India, Dr. Rupali Suresh and Prof. Suresh Bhalla, and my master thesis supervisor, Dr. Eva Monroy in France for initiating me into the field of scientific research.

I would also like to thank all my collaborators, Dr. Dario A. Arena, Brookhaven National Laboratory, USA; Dr. Balazs Sipos, Dr. Christoph Boedefeld, Dr. J.P.Nunez, Attocube, Munich, Germany; Prof. Herve Courtois, Dr. Clemens Winkelmenn, Institute Neel, Grenoble, France; Dr. D. Alba Venero, Dr. Christy Kinane, and Prof. Sean Langridge, Rutherford Appleton Laboratory, UK; Dr. M. Ward, Institute of Material Research, Univ. of Leeds, UK.

Thanks to my friends and colleagues Shraddha, Anna, Ankur, Sotiris, Michael, and Moa who have been with me through thick and thin. Thanks to Rowan who never fails to inspire people around him. Thanks also to Chantal, Jason, Raffa ,Philippa, Sophie, Dong, Risalat, Charles, and George for making my stay at Leeds enjoyable. Special thanks to Fatma and Kowsar for taking care of me and keeping me alive during last few toughest weeks of thesis writing.

I would like to thank all the people associated with the Condensed Matter Group at University of Leeds, I express my sincere appreciation for the learning opportunities provided by the group. I would like to specially thank the Marie Curie Q-NET network for funding my research at University of Leeds, UK without which it would have been impossible for me to carry out the research work.

Finally, I thank my parents and my sisters, Priyarupa and Priyanjana for their unstinted support and encouragement to pursue research work.

Abstract

We have investigated the Co-doping dependence of the structural, transport, and magnetic properties of ϵ-Fe$_{1-x}$Co$_x$Si epilayers grown by molecular beam epitaxy on silicon (111) substrates. Low energy electron diffraction, atomic force microscopy, X-ray diffraction, and high resolution transmission electron microscopy studies have confirmed the growth of phase pure, defect free ϵ-Fe$_{1-x}$Co$_x$Si epitaxial films with a surface roughness of ~ 1 nm. These epilayers are strained due to lattice mismatch with the substrate, deforming the cubic B20 lattice so that it becomes rhombohedral. The temperature dependence of the resistivity changes as the Co concentration is increased, being semiconducting-like for low x and metallic for $x \gtrsim 0.3$. The films exhibit the positive linear magnetoresistance that is characteristic of ϵ-Fe$_{1-x}$Co$_x$Si below their magnetic ordering temperatures T_{ord}, as well as the huge anomalous Hall effect of order several $\mu\Omega$cm. The ordering temperatures are higher than those observed in bulk, up to 77 K for $x = 0.4$. The saturation magnetic moment of the films varies as a function of Co doping, with a contribution of ~ 1 μ_{B}/ Co atom for $x \lesssim 0.25$. When taken in combination with the carrier density derived from the ordinary Hall effect, this signifies a highly spin-polarized electron gas in the low x, semiconducting regime.

To understand the electronic structure and evolution of magnetism in B20 system we used soft X-ray absorption (XAS) and X-ray magnetic circular dichroism (XMCD) spectroscopy in total electron yield mode (TEY) to probe the $L_{2,3}$ edges of Fe and Co in Fe$_{1-x}$Co$_x$Si thin films. Branching ratios ($L_3/(L_2 + L_3)$) as a function of x, suggests that the number of holes associated with Co increases from x=0.1 to x=0.5 where as that associated with Fe changes little. Variation in the occupation states of Fe and Co atoms coupled with shift in $L_{2,3}$ edges ($\sim 500\ meV$) and the evolution of the L_3 edge line shape indicates a modified band structure. The dichroism on Fe L_3 edge (TEY) varies from 0.6×10^{-3} for x=0.1 to 1.4×10^{-3} for x=0.5 and that of Co evolves from being negligible for x=0.1 to 1.7×10^{-3} for x=0.5. Whilst the magnetism in Fe$_{1-x}$Co$_x$Si system arises from the Co doping, these asymmetry spectra clearly show that the magnetic moment is delocalised on both Co and Fe sites.

Contents

CHAPTER 1

Introduction

The rich behaviour shown by ferromagnetic semiconductors arises from an interesting interplay of their electronic density of states and magnetic interactions within the crystal structure, offering new possibilities for spintronics [1]. Whilst most magnetic semiconductors to date are based on compound or oxide materials, the transition metal monosilicides are promising candidates in that they are based on silicon, by far the most common commercial semiconductor. These materials crystallize in cubic B20 structure, the ϵ-phase, and which belongs to the space group $P2_13$ [2]. They are continuously miscible with each other and form an isostructural series compounds with endmembers MnSi (a metallic helimagnet), FeSi (a paramagnetic narrow-gap semiconductor), and CoSi (a metallic diamagnet) [3]. They have been studied for many years as they exhibit a wide variety of different aspects of condensed matter physics including paramagnetic anomalies,[4; 5] strongly correlated/Kondo insulator-like behaviour,[6–9] non-Fermi liquid behaviour, [10–12] unusual magnetoresistance,[3; 13; 14] and helical magnetism [15–18] with skyrmion phases [19–22] that have associated topological Hall effects [23–26].

Almost all work to date on the monosilicide materials has been carried out using bulk single crystal samples. For technological applications, thin films that can be patterned into devices with conventional planar processing techniques are required. Epilayers of the helimagnetic metal MnSi have been grown by using molecular beam epitaxy (MBE) by Karhu *et al.*,[27–29] Li *et al.*,[30] and Engelke *et al.*[31] The properties are broadly comparable to those of the bulk material, including the presence of chiral magnetism [28] and a topological Hall effect [30], which survives in the presence of Fe doping [32]. Other monosilicides have received less attention to date as thin films. The family of alloys $\mathrm{Fe}_{1-x}\mathrm{Co}_x\mathrm{Si}$ should be of particular interest for spintronics: whilst both endmembers are non-magnetic, magnetic ordering is evident at almost all intermediate values of x [3]. For low doping levels of Co in the semiconducting parent FeSi, a magnetic semiconductor with a half-metallic state is expected [3; 33].

FeSi in its ground state is a non magnetic narrow band gap semiconductor [5]. It is the only Kondo insulator that lacks a rare earth element in composition [9]. At higher temperature the narrow band gap closes and a heavy fermion metal is obtained [7]. Various theories based on Kondo lattice [34], spin fluctuation theory [35], and two band Hubbard model [2] have been proposed to account for the observed properties. Upon doping FeSi with Co, Co substitutes onto an Fe site in the crystal structure and transforms it into a magnetic n-type semiconductor [36], before becoming metallic at high doping densities. The Co atom donates one electron to the conduction electron gas and one Bohr magneton to the net magnetisation of the system, making the it fully spin polarised [33]. The theoretical calculations by Guevara *et al.* [33] supports full spin polarisation in $Fe_{1-x}Co_xSi$ system. Manyala *et al.* [37] made some interesting discoveries based on Co doped FeSi in bulk system. $Fe_{1-x}Co_xSi$ in bulk shows a huge anomalous Hall effect [37] which they reason is due to intrinsic contribution, creation of non Fermi liquid states [38], and a positive magnetoresistance [38] that has been attributed to quantum interference of electrons [38] or Zeeman splitting [39] that leads to separation of spin density of states where minority spins have higher mobility.

Most of the studies including the ones mentioned above has been on bulk single crystal samples grown by arc melting[38; 39], levitation etc. Some attempts at growing films have been made already using Pulsed Laser Deposition[40] but they seem to lose the properties seen in bulk. $Fe_{1-x}Co_xSi$ nanowires have been synthesised by DeGrave *et al.* [41], their properties seem to be different than the bulk, the nano wires are chemically unstable and are oxidised also they are not fully spin polarised for low Co doping. Polycrystalline thin films of $Fe_{1-x}Co_xSi$ have been grown by pulsed laser deposition [38], and sputtering [42], but with properties that fall short of those (huge anomalous Hall effect, high spin polarisation etc..) in single crystal samples due to microstructural disorder and lack of phase purity.

The $Fe_{1-x}Co_xSi$ system is also important from application point of view. The full spin polarisation of $Fe_{1-x}Co_xSi$ system could be used in spintronics, they can act as spin injectors. There is, however, a significant property of the system that can perhaps change the way we store and read data. The B20 crystal structure lacks inversion symmetry which gives rise to Dzyaloshinskii-Moriya interaction in $Fe_{1-x}Co_xSi$ system. This further leads to formation of chiral spin texture called skyrmions. Skyrmions are magnetic knots or vortices that have already been observed in $Fe_{1-x}Co_xSi$ bulk crystal by Lorentz Transmission Electron Microscopy (LTEM) [21]. When electrons traverse through such a structure adiabatically, they pick up a Berry phase. The Berry phase is then manifested in the transport measurements as an extra Hall signal, this is also called Topological Hall Effect (THE). THE has already been observed in MnSi crystal [27], [28]. Small Angle Neutron Scattering (SANS) studies on MnSi crystal [44] has

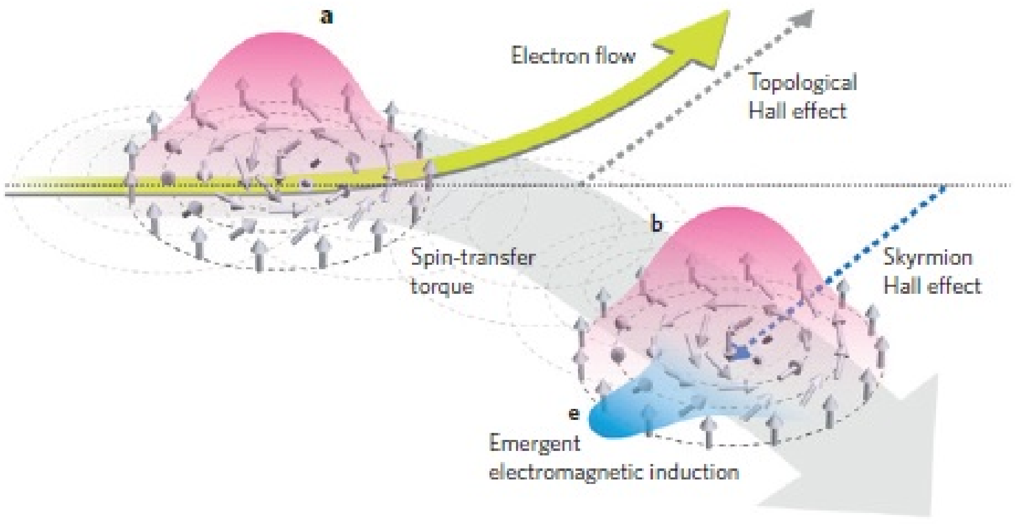

Figure 1.1: Schematic picture of skyrmion motion and associated physical phenomena under the flow of electrons. Electron current drives the flow of a skyrmion by means of the spin-transfer torque mechanism (that the direction of the charge current is the opposite to the electron flow). Electrons are deflected by the Lorentz force due to the emergent magnetic field b of the skyrmion, which results in the THE. The motion of the skyrmion is accompanied by the time-dependent emergent magnetic field (pink), and hence the emergent electric field e, that is, emergent electromagnetic induction.[43]

previously shown a rotation of the diffraction pattern of Skyrmion Lattice Phase (SLP) when an electric current exceeding the threshold current density (j_c) of 10^6 Am^{-2} [43] is applied transverse to the skyrmion motion. It is important to note that j_c is 10^5 times smaller than the current needed to induce a spin-torque based domain walls motion in a ferromagnet [43]. This also means that the excess power dissipation would be 10^{12} times lesser.

Keeping the above points in mind, this thesis presents a report on the properties of epitaxial ϵ-Fe$_{1-x}$Co$_x$Si layers grown on commercial Si [111] substrates, across the doping range $0 \leq x \leq 0.5$, using the growth methods previously developed deeveloped at Leeds [14]. The films are phase pure, with a B20 lattice that is distorted by biaxial in-plane epitaxial strain to have a rhombohedral unit cell. Although Fe$_{1-x}$Co$_x$Si is known to possess a helimagnetic ground state [15–18], we focus our research more on the properties in fields large enough to generate a uniformly magnetized ferromagnetic state. We find that these epilayers display the full range of properties expected of this material, including a characteristic temperature dependence of resistivity [13], positive linear magnetoresistance [3; 13], a very large anomalous Hall effect [37], and one Bohr magneton (μ_{B}) of magnetic moment per electron-like carrier in the low doping ($x \leq 0.25$) regime [3; 42], indicative of the presence of a half-metallic state [33]. Nevertheless, the presence of epitaxial strain, giving rise to an expanded unit cell volume, leads to some quantitative changes, the most prominent of which is a substantial enhancement of the magnetic ordering temperature with respect to bulk crystals. These epilayers are suitable for patterning into nanostructures that may find use as spin injectors into silicon [45–47] or exploit the chiral nature of the magnetism at low fields in skyrmion-based devices [48–50]. The present thesis has been laid out in a chapter wise manner and a brief description of the chapters is as follows:

The second chapter presents the theory relevant to Fe$_{1-x}$Co$_x$Si system such as spin splitting, helimagnetism, ferromagnetism etc. It essentially equips the reader with the concepts necessary to understand and interpret the results presented in further chapters. Other theoretical concepts pertaining to a particular technique or so will be explained as the reader progresses along the chapters.

The third chapter, literature review, contains a broad review of dilute magnetic semiconductors, transition metal silicides with particular emphasis laid on $\mathrm{Fe}_{1-x}\mathrm{Co}_x\mathrm{Si}$ system and a current update on recent research on $\mathrm{Fe}_{1-x}\mathrm{Co}_x\mathrm{Si}$ system.

The fourth chapter is based on growth and characterisation, reports the growth of $\mathrm{Fe}_{1-x}\mathrm{Co}_x\mathrm{Si}$ thin films by Molecular Beam Epitaxy (MBE) and further characterisation of the films by in-situ low energy electron diffraction (LEED), reflection high energy electron diffraction (RHEED), atomic force microscopy (AFM), X-ray diffraction (XRD), and transmission electron microscopy (TEM). Based on the data obtained, results were analysed to obtain various lattice parameters of the $\mathrm{Fe}_{1-x}\mathrm{Co}_x\mathrm{Si}$ unit cell. Finally, stress and strain relationship were investigated and final results are presented.

The fifth chapter is based on transport properties, patterning the $\mathrm{Fe}_{1-x}\mathrm{Co}_x\mathrm{Si}$ thin films, and doing further measurements of Hall effect including ordinary Hall effect, anomalous Hall effect and topological Hall effect. Results are presented in a very systematic manner. We saw that the $\mathrm{Fe}_{1-x}\mathrm{Co}_x\mathrm{Si}$ epilayers show characteristic positive linear MR, the films have huge AHE, the THE looks promising and needs to be investigated further.

The sixth chapter is based on Magnetic characterisation and presents the result obtained by analysing the $\mathrm{Fe}_{1-x}\mathrm{Co}_x\mathrm{Si}$ films using using various magnetic characterisation techniques such as, Vibrating Sample Magnetometry (VSM), Magnetic Force Microscopy (MFM), Soft X-ray spectroscopy etc. We see that the $\mathrm{Fe}_{1-x}\mathrm{Co}_x\mathrm{Si}$ epilayers are fully spin polarised for low Co doping. Evolution of dichroism on Fe and Co edges indicate that the magnetism in the system arises due to both Fe and Co atom.

The last chapter, seven, binds together the results from all the other chapters. It constitutes detailed analysis of the results obtained by characterising $\mathrm{Fe}_{1-x}\mathrm{Co}_x\mathrm{Si}$ epilayers in a broader picture, and finally the conclusion is presented. A future outlook and further experiments have been suggested to finally conclude the thesis.

CHAPTER 2

Theoretical Background

2.1 Ferromagnetism in $3d$ transition metals

Ferromagnetism in solid refers to a long range, spontaneous alignment of magnetic moments without any externally applied magnetic field. These materials may be divided into two classes based on the position of the magnetic moments, it could be a localised ferromagnet or an itinerant ferromagnet. A localised ferromagnet is represented by $4f$ or $5f$ rare earth metals, where magnetic moments are carried by the localised electrons. Spin lattice models have been used to treat these localised materials successfully. On the other hand magnetic moments in $3d$ metals like Fe, Co, and Ni are carried by strongly delocalised valence electrons near the Fermi level making them itinerant ferromagnets. These delocalised valence electrons can be treated collectively to explain the itinerant model. Quantum mechanical exchange is the reason for this collective phenomena. It also reflects on the balance of electrostatic energy of electrons based on their spins. As a consequence of Pauli's principle, no two electrons can have same set of quantum numbers. Electron, therefore have to be promoted to higher energy states. Hence the parallel arrangement of spins is generally accompanied by an increase in the kinetic energy. Another consequence of Pauli's principle is the reduction in electrons with same spin orientation close to each other, electron are now surrounded by exchange holes. Keeping the same charged particles apart reduced the Coulomb repulsion. For a parallel spin arrangement the electrostatic energy reduces as compared to antiparallel alignment, this is exchange energy. Net energy balance when exchange energy exceeds the kinetic energy is achieved by alignment of spin in parallel in a magnetically ordered groundstate.

In case of ferromagnetism, the energy states of valence electrons corresponds to band states in solids. This band magnetism gives rise to Stoner's criteria for ferromagnetism. It essentialy relates the balance between kinetic energy of the system and the exchange energy with the electronic states. Stoner's criteria is explained in the following section.

2.2 Stoner Criteria

In molecular field theory, all the spins in a system experience an identical exchange field (M) produced by their neighbours. Through Pauli's paramagnetism (χ_P), this molecular field in a metal can magnetise the electron gas which in turn would be responsible for the molecular field, if both M and χ_P are large enough. If ($n_\uparrow(\varepsilon_F)$

and $n_{\downarrow}(\varepsilon_F)$ be the spin up and spin down density of states at the Fermi level then M may be defined as the difference between spin up and spin down density of states in an atomic unit cell, it is given by the following equation

$$M = \int^{\varepsilon_F} (n_{\uparrow}(\varepsilon_F) - n_{\downarrow}(\varepsilon_F))d\varepsilon \tag{2.1}$$

As per Density Functional Theory (DFT), the spin dependent interactions enter an exchange correlation potential V, which is a part of the net effective potential. Interaction of M with rest of the electronic system is very small, V can therefore be given by the following equation

$$V = V^o \mp \bar{V} \cdot M \tag{2.2}$$

where V^o is the exchange correlation potential for non magnetic case. $\bar{V}$ has positive value therefore, majority or spin up electrons are strongly attracted and spin down or minority electrons feel strong repulsive potential. A constant, $I = 2\bar{V}$ is introduced in Stoner model to represent this enhancement or decrement in potential and is given by the following equation:

$$V = V^o \mp \frac{1}{2} I * M \tag{2.3}$$

I essentially represents the exchange integral or is the Stoner parameter and in a many body system it averages over all the Coulomb interactions. It also representative of the exchange interaction strength between the atoms. A ferromagnetic solution will exists if the following equation is satisfied

$$I * D(E_F) > 1 \tag{2.4}$$

This is the Stoner criterion that related exchange integral I with density of states $D(E_F)$. The condition is fulfilled for materials with strong Coulomb effects and large density of states, $3d$ transition metals are one such example. For itinerant magnetism the Stoner criteria is fulfilled by only three transition metal, Fe, Co, and Ni.

2.3 Spin-split electronic bands

One of the most important consequence of Stoner model is the spin splitting of the electronic band structure of 3*d* ferromagnets. From equation 2.2 it can be derived that the constant change (I $*$ M)/2 of the potential V does not act on the spatial part of the electronic wavefunction. The eigenvalues are however shifted by this constant. Thus the two fold degeneracy of the electronic states is lifted by the exchange interaction resulting in spin splitting of the band structure. Ignoring the spin orbit coupling, majority and minority bands can be understood as two independent set of bands separated by exchange interaction (I $*$ M). The exchange splitting is not a constant and is dependent upon the electron wave vector and symmetry of the bands. Exchange splitting is much larger for *d* bands than for *s* or *p* bands. From Fe to Co to Ni the atomic no. increases resulting in filling of *d* bands and moving it down below the Fermi level.the minority density of states is unfilled for all the three elements. However the majority band, Fe is not completely filled as Co or Ni. As a result of which Fe has more density of states at the Fermi level than Co or Ni. The same has been shown in figure 2.1.

2.4 Spin Polarisation

Spin polarisation is a direct consequence of spin split density of states of electrons leading to the polarisation of charge carriers in the system. Exchange energy $n(\varepsilon)$ is responsible for the splitting of spin density of states. Also it is important to note that the spin polarisation of the whole electron population is not representative of the polarisation of spin density at the Fermi level (ε_F), as it is different for different spins. Let ↑ and ↓ represent the majority and minority spin electrons respectively. Then net spin polarisation is given by the following equation

$$P = \frac{n_\uparrow(\varepsilon_F) - n_\downarrow(\varepsilon_F)}{n_\uparrow(\varepsilon_F) + n_\downarrow(\varepsilon_F)} \tag{2.5}$$

Fermi's Golden rule for scattering probabilities dictates the conductivity of the electrons and is proportional to the density of states available at the Fermi level. This is why spin up and spin down electrons have different mobilities and it is because of this reason that spin polarisation plays an important role in spin transport or in spintronics. The two current model described by Mott, where both the spins have parallel channel of

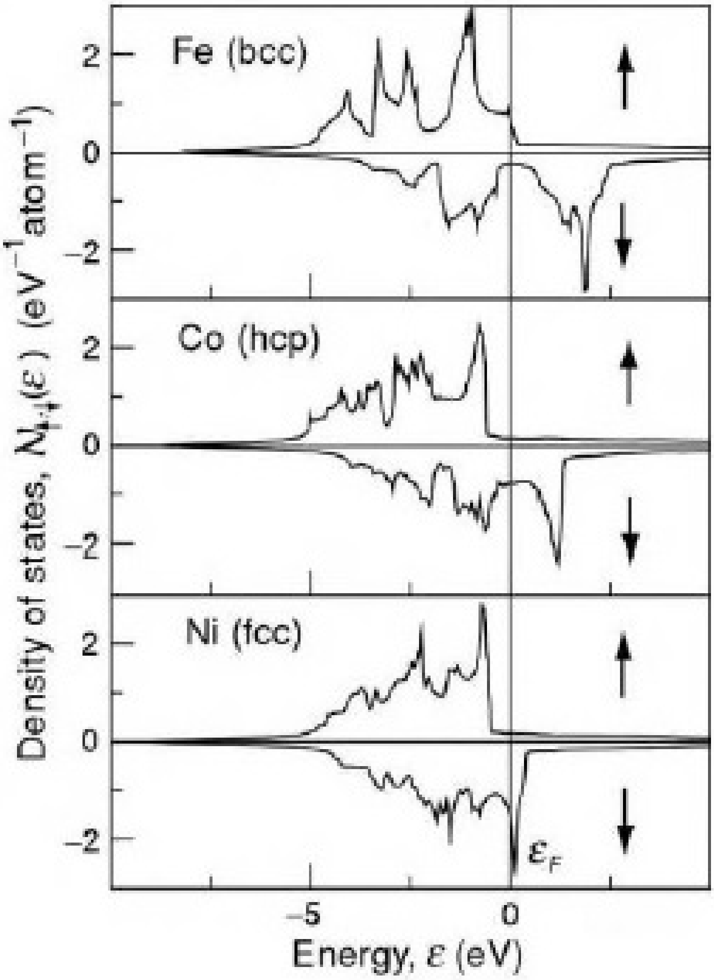

Figure 2.1: Calculated density of states of some 3d metallic elements in their ferromagnetic state. The Fermi level is denoted by ε_F. The up arrow and the down arrow represents the spin up and spin down density of states respectively. Following Stoner's criteria, if the spontaneous band splitting is sufficient enough to push the spin up d-subband completely below the ε_F, we get a strong ferromagnet (Co and Ni) else we get a weak ferromagnet (Fe). [51]

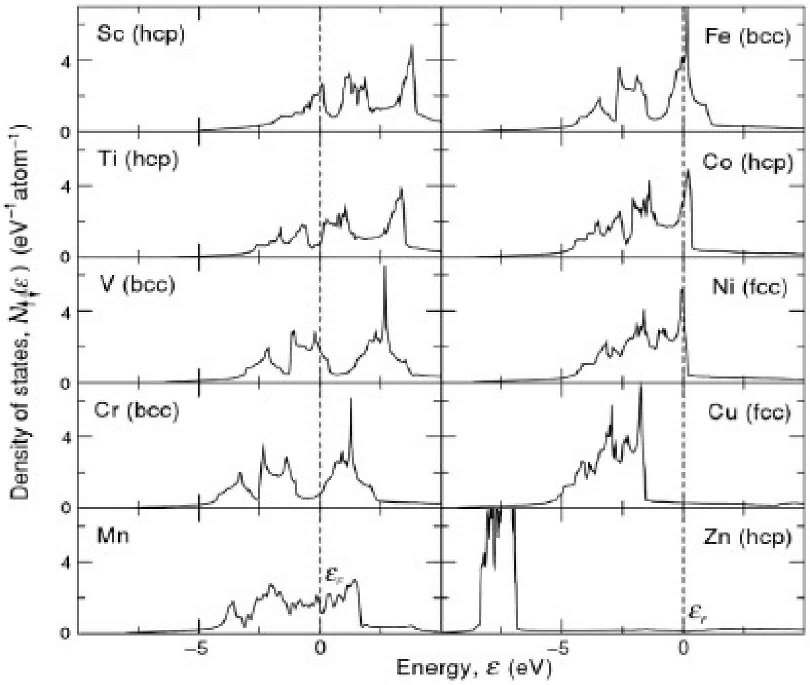

Figure 2.2: Calculated density of states of some metallic elements in their paramagnetic state where a 3d band has been superposed on a broader 4s band. The Fermi level is denoted by ε_F. [51]

conduction has successfully described the ferromagnet transport properties. Therefore, a charge current has a spin polarisation when is driven through a ferromagnet due to spin split density of states. The net spin polarisation (P) described by equation 2.4 is less than unity for a ferromagnetic magnet eg. for Fe, P is 0.44, for Co it is 0.34, and so on. However, for certain materials P can take the value 1. This in turn implies that there is only one spin split band at the Fermi level, such materials are also known as half metals. Half metals are not be confused with semi metals. In semi metals, the valence band and conduction band overlap such that there are small number of holes and equal number of electrons present eg. graphite, bismuth and antimony [52]. CrO_2 and Fe_3O_4 are examples of half metals. Half metals have long spin diffusion length which makes them suitable for various spintronics application such as, in magnetic tunnel junctions or in spin transistors.

2.5 Spin orbit coupling

The Spin and orbit angular momenta interacts via weak spin-orbit interaction. It acts as a perturbation on well defined **L** and **S** states. **L** and **S** are not separately conserved but the total angular momentum **J**=**L**+**S** is conserved. Here **L** is the orbital angular momentum and **S** is the total spin angular momentum. The Hamiltonian describing the spin orbit coupling (SOC) in second order is,

$$H_{SO} = \frac{1}{2m_0^2c^2} s \cdot (\bigtriangledown V \times p) \tag{2.6}$$

where, V is the external potential acting on the electron, p is the momentum operator, m_o is the bare mass of the electron, s is the spin operator described as $s = \hbar\sigma/2$ and σ is the pauli matrices.

2.6 Helimagnetism in transition metal silicides

Like other transition metal silicides, FeSi crystallises in a B20 cubic structure, which may be viewed as a distorted rocksalt structure with basis vectors as (u, u, u), $(\frac{1}{2} + u, \frac{1}{2} - u, \overline{u})$, $(\overline{u}, \frac{1}{2} + u, \frac{1}{2} - u,)$, and $(\frac{1}{2} - u, \overline{u}, \frac{1}{2} + u)$. The primitive cell contains four formula units of FeSi and belongs to the space group $P2_13(T^4)$. The point symmetry at Fe and Si site is C_3. The space group $P2_13$ is nonsymmorphic and contains 12 symmetry operations such that the operations involving C_3 are associated with primitive translations and the operations involving non primitive translations are combined with tetrahedral point group T. The lattice parameter (a) of FeSi as previously determined by single-crystal x-ray-diffraction study come out to be 4.489 $\mathring{A}$ and the corresponding internal atom positions for Fe and Si are 0.137 and 0.842 respectively [34].

Bak and Jensen first developed the theory to describe the helical magnetic structures in B20 materials [53]. The broken inversion symmetry in a B20 crystal gives rise to right handed or left handed crystal chirality. The inversion symmetry constitutes four main interactions that contributes to the free energy density of the structure. Zeeman interaction, exchange interaction, anisotropy exchange interaction and finally the Dzyaloshinskii- Moriya interaction that arises because of spin orbit coupling. The final expression for the free energy density(ω), resulting from interactions mentioned above is given by the equation below [29],[53].

$$\omega(M) = \frac{c_1}{2} M_S^2 (\bigtriangledown \hat{M})^2 + b_D M_S^2 \hat{M} \cdot ((\bigtriangledown \times \hat{M})) + \frac{S^2 F Q^2 (\vec{L} \cdot \hat{M})}{4a^3} - \mu_o \vec{H} \dot{\vec{M}} \tag{2.7}$$

where, M_S represents the saturation magnetization, $\vec{M}$ represents the magnetization vector, $\hat{M} = \frac{\vec{M}}{M_S}$ is an unit vector in magnetization direction, $\vec{H}$ is the applied magnetic field, $S = 0.8\ \hbar$ is the spin per unit cell, $a = 0.4489$ nm is the lattice constant of FeSi unit cell, anisotropic exchange constant is F, $\vec{L}$ is the cubic invariant that describes the anisotropy. The constants c_1 and b_D are related to the spin wave stiffness A and the Dzyaloshinskii-Moriya constant D is represented by $c = AS/(M_S^2 a^3)$ and $b_D = DS/(M_S^2 a^3)$.

The Dzyaloshinskii Moriya interaction is represented by the second term in the equation, favours the perpendicular alignment of neighbouring spins where as the first term in the equation that represents the exchange interaction favours the parallel alignment of the neighbouring spins. These two competing interaction gives rise to one dimensional modulated structures such as helical and conical phases and two dimensional skyrmions in the crystal structure.

The helical phase consists of planes of ferromagnetically aligned spins stacked on top of one another and perpendicular to the propagation vector,Q. Each of the successive planes have their spins oriented at a slightly different angles from each other, giving

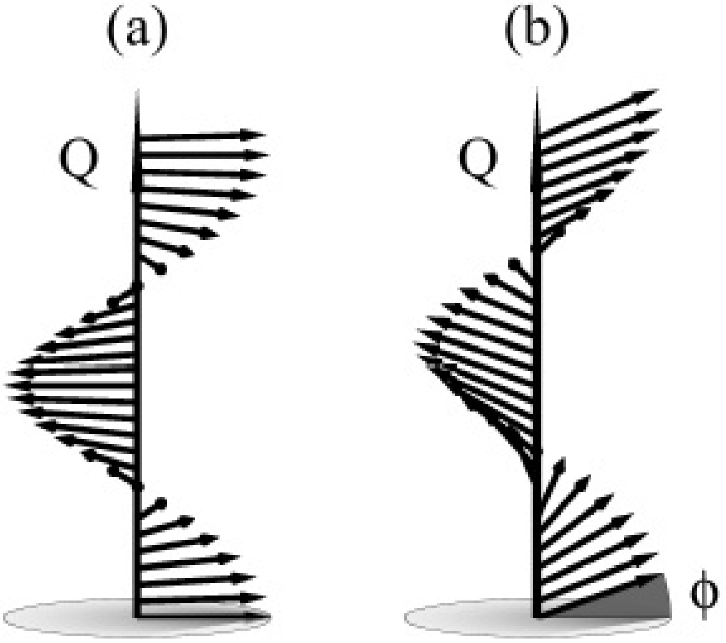

Figure 2.3: Magnetization structure where the arrows represent the direction of the magnetization at each point. (a) Helix, (b) Cone with cone angle $\phi = \frac{\pi}{9}$. [54]

rise to a twist with a fixed chirality. The angle slowly increases in a linear manner along Q and spans through 2π. The cone phase has an arrangement of spins similar to that of a helix but the spins are canted towards the propagation vector Q vector at an angle ϕ, also known as the cone angle. The equation below shows an expression to calculate the magnetization of this phase with Q as the propagation vector. Using the same expression one can calculate the magnetization for the helical phase by setting $\phi = 0$.

$$\vec{M} = M_S(sin(Q_z)Cos(\phi), cos(Q_z)cos(\phi), sin(\phi)) \tag{2.8}$$

Chapter 3

Literature Review

Ferromagnetic semiconductors (FS) have been widely researched upon mainly because of their potential use as spin-polarized carrier sources and their easy integration with other semiconductor devices. An ideal FS should have high Curie temperature and should be able to incorporate not only p-type, but also n-type dopants. The Eu chalcogenides (Eu^{2+}) were one of the early FS that were extensively studied, but were not successful as the ferromagnetic transition temperature or the Curie temperature (T_C) was much lower than room temperature. The discovery of Curie temperatures as high as 110 K in III-V based diluted magnetic semiconductors (DMS)[55] alloys where some atoms are randomly replaced by magnetic atoms (such as Mn^{2+}) generated a lot of attention and are still researched upon. Other promising materials that exhibit large spin polarisation include ferromagnetic oxides (CrO_2 and related compounds, many of which claim to be half-metallic such as magnetic Heusler alloys, various members of the mixed valence perovskites, e.g., $La_{70}Sr_{30}MnO_3$ etc. But most of them, DMS such as $Ga_{1-x}Mn_xAs$ [55][56][57] or the less studied concentrated magnetic semiconductors, such as EuS [58],[59] and EuO [60], and CrO_2[61] (half-metallic) suffer from poor electrical contact or non ohmic contact to silicon.

Transition metal silicides such as MnSi, FeSi, and CoSi crystallize in cubic B20 structure (Fig. 3.1, left), belong to $P2_13$ space group, isostructural, and are continuously miscible with each other. The B20 crystal structure has attracted attention because of its peculiar geometrical characteristics. The B20 structure can be thought of as a deformation of the rocksalt structure. The simple cubic structure becomes B20 when distorted along the [111] direction. The crystal structure of FeSi belongs to the T^4P2_13 space group. Together with FeSi other compounds involving a transition metal and a Si atom have been found to have the same crystal structure. The unit cell contains 4 Fe atoms at crystallographically equivalent positions. The sub-lattice of transition metal atoms, displayed in Fig. 3.1-right,

Figure 3.1 reveals that the basic structural element is an equilateral triangle of 3 Fe atoms. The structure is corner-sharing i.e. each Fe atom connects 3 triangles, which occur with 4 different orientations along the body-diagonals of the cubic unit cell. We focus on those binary transition metal silicides which are in the ratio 1:1 because in this case the sublattice of each element has a frustrated geometry. For two elements in order to crystallize in the $P2_13$ space group the ratio between the atomic

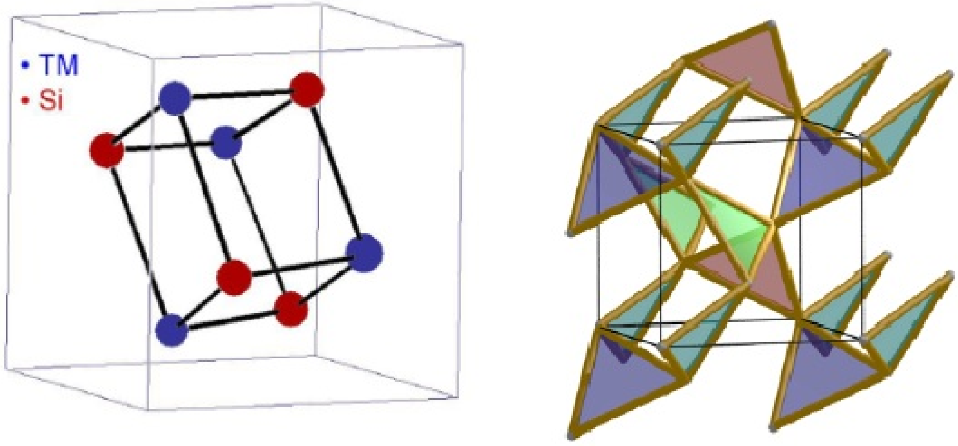

Figure 3.1: Left: The T^4P2_13 crystal structure for TM-mono silicides. Right: Fe sublattice of FeSi. The corners of the triangles, all of which are equilateral, correspond to the positions of the Fe-atoms [62]

radii has to be satisfied. The interatomic distance for these compounds is between 2.2 Å and 3 Å which means that the bond length is small. Consequently, the orbitals of the elements involved in the bonding are strongly hybridized and the compounds have a covalent nature. In case of transition metal mono silicides, elements with the tendency to localize electrons, such as transition metals, form covalent-like bonds with silicon. The interplay between localization and covalency, together with the geometrical frustration of the transition metal sublattice, leads to several unexpected phenomena. Some transition metal mono-silicides have shown non Fermi Liquid behavior[3][63].

A remarkable feature observed from the band diagram of transition metal silicides as calculated by the first principle band structure approximation[64] (Figure 3.2) is the symmetry of the B20 structure. One can see that at the X, M and R point several bands merge into a degenerate one i.e. the bands tend to stick together at certain symmetry points in momentum space. The sticking of bands around the high symmetry points has consequences on the Fermi surface topology and scattering process [65]. We observe that for MnSi several bands cross at the Fermi level and it behaves as a good metal, while FeSi has a small gap and it is a narrow bandgap semiconductor; CoSi has a low density of states (DOS) at the Fermi level and is a bad metal.

Another interesting property of the system rising from the interplay of the spin

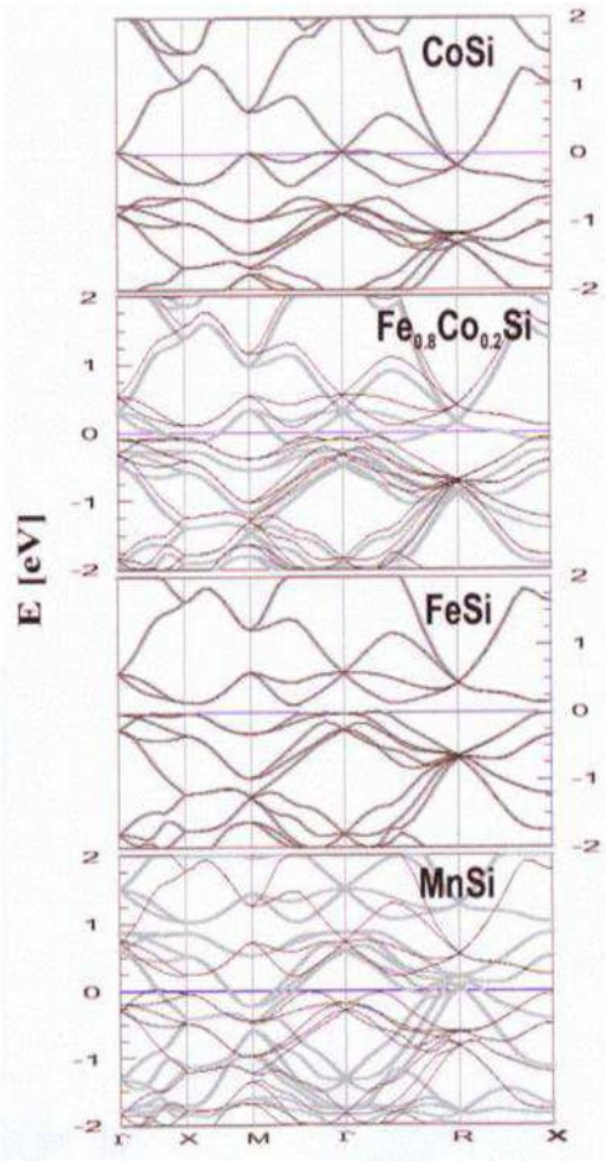

Figure 3.2: First principle band structure approximation of transition metal silicides in the momentum space. The figure shows the DOS available at the Fermi level (indicated by a zero on either left hand side or right hand side axis). [64] [62]

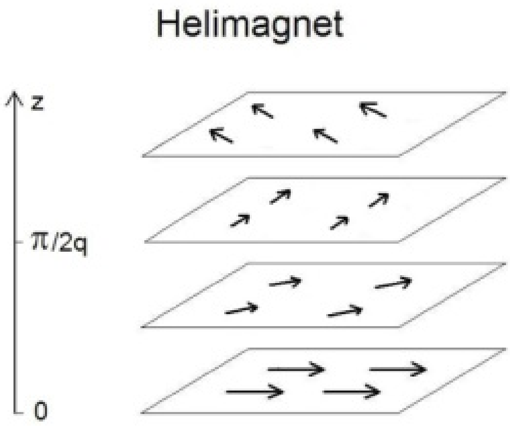

Figure 3.3: The figure above shows magnetic ordering in a helimagnet. On each plane, there is a ferromagnetic order but the direction of magnetization rotates along the helical direction. The arrow on the left denotes the direction of the helix [62].

orbit coupling and exchange interaction is the Dzyaloshinsky-Moriya interaction in the inversion symmetry broken B20 crystal which gives rise to helical spin structure in absence of any magnetic field (figure 3.3). One can find the signature of helimagnetism in transition metal silicides such as MnSi, FeSi and $\mathrm{Fe}_{1-x}\mathrm{Co}_x\mathrm{Si}$ at low temperature by application of small magnetic field which turns the direction of the wave vector of the helical spin to that of the magnetic field. When the magnetic field is increased further, a homogeneous component of the magnetic order is introduced and the direction of the magnetic moment is tilted to that of the magnetic field so that the conical spin structure emerges. The magnetisation increases linearly with the magnetic field as the tilting angle increases. Then the magnetisation shows a kink indicating the emergence of an induced ferromagnetic state. Helimagnetism has been long investigated in $\mathrm{Fe}_{1-x}\mathrm{Co}_x\mathrm{Si}$ system. Some of the earliest investigation results are from Beille et al [15], [16]. SANS and low field magnetisation measurements were used to probe $\mathrm{Fe}_{1-x}\mathrm{Co}_x\mathrm{Si}$ and it was found to have long period of helical structure. Also, low temperature resistivity measurements exhibited positive magnetoresistance which was then attributed to alloying effect as that would lead to repartion of magnetic moment in the helix structure. Helimagnetism was explained in terms of occurance of Dzyaloshinsky-Moriya spin orbit type interaction in non centriosymmetric crystal. Ishimoto *et al.* [66] further studied the long helical period in $\mathrm{Fe}_{0.8}\mathrm{Co}_{0.2}\mathrm{Si}$ single crystals by polarised neutron diffraction and observed that in as cooled state, multiple helices transform into a single clockwise helix by a magnetic field pointing in any direction. They also found out that the propagation axis lies along $< 001 >$ by SANS. Grigoriev *et al.* [67] also investigated $Fe_{1-x}Co_xSi$ system using Neutron diffraction and SQUID measurements. The helices were found to be doping dependent, they switched between left for x=0.1, 0.15 Co doping and right for x =0.2, 0.25, 0.3, 0.5 Co doping as investigated by Maleyev *et al.* [18] using polarised neutrons.

The magnetisation in these compounds has been explained in the framework of weak itinerant ferromagnetism. Itinerant magnetism in $Fe_{1-x}Co_xSi$ system has been long debated upon. Beille [68] found weak itinerant ferromagnetism in $Fe_{1-x}Co_xSi$ under high fields . Ishimoto using Polarised Neutrons (PN) Diffraction found that $Fe_{1-x}Co_xSi$ is composed of two kinds of magnetic moments, a 3d-like magnetic moment localised on Fe and Co sites and a weak negative moment diffused all over the crystal lattice, The 3d like magnetic moment was found to be 0.263 ± 0.014 μ_B/Fe,Co atom and -0.046 ± 0.014 μ_B/F.U. [69]. Chattopadhyay et al. [70] used specific studies based on Mossbauer spectroscopy, Neutron and Magnetic Resonance (NMR) to establish that the magnetic electrons in $Fe_{1-x}Co_xSi$ are itinerant in nature and that the onset of magnetism can be understood in terms of the Stoner model. They go on to show the Stoner type excitations in the H-T dependence of magnetisation in $Fe_{1-x}Co_xSi$ alloys, they also see spin fluctuation in the system that has been explained by Moriya theory of spin fluctuations (Moriya 1982).

Even though FeSi is paramagnetic [5] and CoSi is diamagnetic, $Fe_{1-x}Co_xSi$ is magnetic for intermediate compositions. $Fe_{1-x}Co_xSi$ shows positive magnetoresistance whereas MnSi shows negative magnetoresistance suggesting that the carriers contributing to the charge transport and to magnetism are the same. The negative magnetoresistance in MnSi can be explained by a suppression of spin fluctuations in magnetic fields (weak itinerant ferromagnet). In colossal magnetoresistance Manganites, the carriers contributing to the transport and those contributing to the magnetism are different and the scattering of the itinerant electrons on the localized ones gives rise to a positive magnetoresistence. In a low carrier density compound such as $Fe_{1-x}Co_xSi$ same electrons are responsible for both magnetic properties and electrical conduction. The positive magnetoresistance is either caused by a combination of disorder and correlation effects as explained by electron-electron quantum interference effects, suggested by Manyala *et al* [3] or by Zeeman splitting that decreases the density of the higher mobility minority spin band, proposed by Onose *et al* [13] or on similar lines by slight field-induced modified minority and majority spin bands that leads to small magnetic moment by Forthaus *et al*[71].

Electron doping of FeSi by substituting Co for Fe produces an n-type metal $\mathrm{Fe}_{1-x}\mathrm{Co}_x\mathrm{Si}$ (Figure 3.2 shows the band structure of $\mathrm{Fe}_{1-x}\mathrm{Co}_x\mathrm{Si}$ for x=0.253). Co replaces a Fe atom in the unit cell and the excess 3d electrons on the Co atom for $x \leq 0.5$ occupy only the majority spin band and the Fermi level lies in the band gap of the minority spin band. While for $x < 0.5$ the Fermi level lies in the conduction band, above the band gap of minority spin band. One of the ways to calculate the electronic structures of $\mathrm{Fe}_{1-x}\mathrm{Co}_x\mathrm{Si}$ is by the linear muffin-tin orbital (LMTO) method with the atomic sphere approximation (ASA) in the local spin-density approximation [72]. In this model, Fe and Co atoms in (Fe, Co) Si are treated as virtual atoms with averaged value of atomic number by the concentration. The present system with the B20-type structure contains four Fe/Co and four Si atoms in a cubic unit cell.

Figure 3.4 illustrates the DOS in $\mathrm{Fe}_{1-x}\mathrm{Co}_x\mathrm{Si}$ for various concentration of x (x=0 to x=1) as calculated by LMTO. Some other important theoretical studies include Band structure approx.-linear augmented plane wave band calculation for cubic FeSi within local density approximation by Mattheiss and Hamann [34]. Local density approximation (LDA) and generalised gradient approximation were used by Al-Sharif*et al* [2] who found out that B20 structure would become unstable as compared to B2 at a moderate pressure of 13.5 and 10.9 GPa. Theoretical results for $\mathrm{Fe}_{1-x}\mathrm{Co}_x\mathrm{Si}$ alloys were also obtained using muffin-tin orbital method and the results were analysed using Stoner, covalent magnetism and rigid band model by Punkknen *et al*[73]; it was found that disorder affects the magnetism in the system significantly. Ab initio calculation by Guevara*et al*[33] found that the Fe rich region in $\mathrm{Fe}_{1-x}\mathrm{Co}_x\mathrm{Si}$ behave like a disordered ferromagnetic half metal. They tried to explain the experimental results, at doping of 0.25 and higher, the system starts to segregate, reducing the value of magnetic moment and half metal like nature disappears . Zhi-Huiet *et al* [74] used full potential linear augmented plane wave method to study the electronic and magnetic properties of $\mathrm{Fe}_{1-x}\mathrm{Co}_x\mathrm{Si}$. It was found that in Fe rich alloys, electronic and magnetic properties

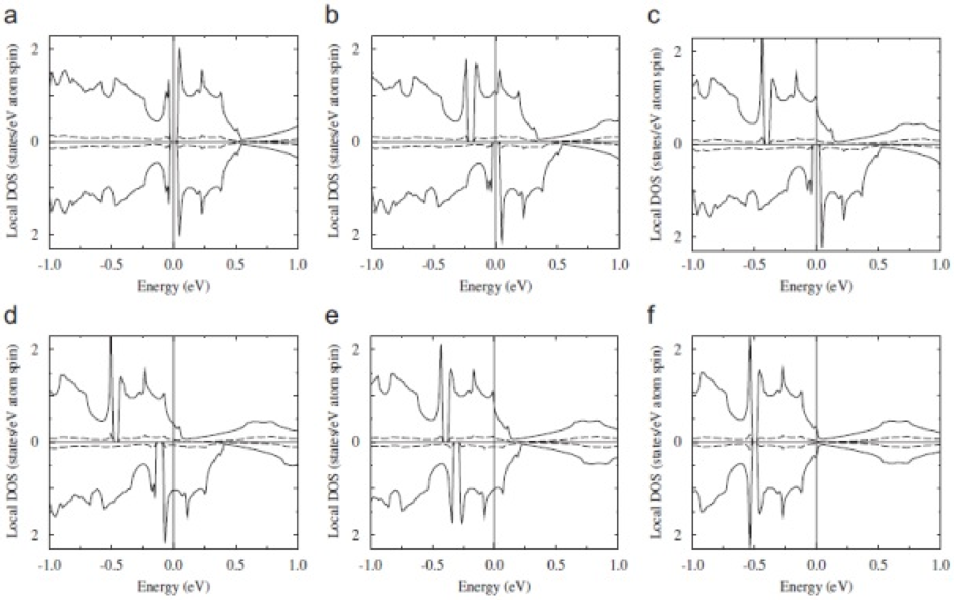

Figure 3.4: Calculated local DOS of the 3d atom (solid curves) and Si (broken curves) for Fe$_{1-x}$Co$_x$Si at x, 0.0 (a), 0.2 (b), 0.4 (c), 0.6 (d), 0.8 (e) and 1.0 (f). Upper and lower portions in each figure are those of majority and minority spin bands. FeSi (a) and CoSi (f) are in the non magnetic state. The origin of energy is the Fermi level [72]

at Fe site depends on the spin polarisation of the nearest Co atom, where as in Co rich alloys, at Co site the same properties depend on neighbour of Fe atoms. LDA combined with dynamical mean field theory was used by Mazurenko *et al* [75] to study the spectral and magnetic properties of $Fe_{1-x}Co_xSi$ system. They found out that Co doping leads to ferromagnetism in the system and its itinerant nature was successfully proved by the model.

The Density of States (DOS) gives rise to various interesting properties in $Fe_{1-x}Co_xSi$ system such as metal-insulator transition for $x > 0.1$, non Fermi liquid behaviour, contribution of one electron by Co atom for conduction, large anomalous Hall effect, increased conductivity etc. $Fe_{1-x}Co_xSi$ is believed to be a half metal [3], [33] and displays positive magnetoresistance and anomalous Hall effect [3], [37]. Also the magnetic semiconducting metal silicide $Fe_{1-x}Co_xSi$ is known to make ohmic contact to silicon[76] and therefore offers an alternative class of material that may serve as a promising injection source for silicon spintronics that is easily integrable with the current planar processing technology. So far the majority of studies on $Fe_{1-x}Co_xSi$ has been based on bulk crystals grown by melting arc method [3], [13], levitation, by pulsed laser deposition [38] etc. Some FeSi films have been synthesised by MBE previously but none have reported the successful growth of B20 structure. DeGrave *et al.* showed the synthesis of $Fe_{1-x}Co_xSi$ nanowires via CVD and with a polarisation of $28 \pm 7\%$ [41]. Recent experimental research on $Fe_{1-x}Co_xSi$ system includes studies on doping dependent transport properties of $Fe_{1-x}Co_xSi$ by Onose*et al.* [13] where they measure positive magnetoresistance in the a single crystal and attribute the result to Zeeman splitting (mentioned before) contradicting the quantum interference scenario proposed by Manyala*et al.* [3]. Doping dependence of the Hall conductivity runs parallel to the critical field and to wave vector of helical spin suggesting that Hall conductivity is proportional to spin orbit interaction. Also, the change in Seeback coefficient is attributed to electronic structural change accompanying the transition from paramagnet to a ferromagnet. They also found out that the Curie temperature decreases with increasing pressure and above 7 GPa no helical state exists. Pressure induced quantum phase transtion (QPT) study by Forthaus*et al.* [71] indicates that the stability of the ferromagnetic states decreases with increasing Co doping. The suppression of the ferromagnetic state is not due to structural instability but strongly coupled to the different degree of local crystallographic disorder. Low temperature transport, optical, thermodynamic and magnetic properties of $Fe_{1-x}Co_xSi$ were studied by Chernikov*et al.*[77] and angle resolved photoemission study of FeSi by Arita*et al.* [78], both of which emphasised on the strongly correlated metal nature of the $Fe_{1-x}Co_xSi$ system. It is further supported by observation of the large anomalous Hall effect by Manyala*et al.* [37] and is attributed to strongly correlated metal nature. They also find that the AHE is dominated by intrinsic effect due to change in band structure rather than impurity scattering.

Recent interest in $Fe_{1-x}Co_xSi$ system is attributed to wide interest in skyrmion physics. Yu *et al.* [21] observed real space skyrmions in $Fe_{1-x}Co_xSi$ bulk system using Lorentz transmission electron microscopy. They applied a magnetic field of 50 mT normal to the film and observed skyrmions in the form of a hexagonal arrangement of swirling spin textures, with a lattice spacing of 90 nm. They backed it up with T-B phase diagram that was found to be in good agreement with Monte Carlo simulations. Also, Milde *et al.* [79] used magnetic force microscopy to track the creation and destruction of the skyrmion lattice on the surface of a bulk crystal of $Fe_{1-x}Co_xSi$ (x = 0.5). They found out that the skyrmions vanish by forming elongated structures. They used numerical simulations to show that changes of topology are controlled by singular magnetic point defects and can thus be viewed as quantized magnetic monopoles and antimonopoles, which provide as source and sink of one flux quantum of emergent magnetic flux, respectively.

With a rich history of experimental and theoretical studies on $Fe_{1-x}Co_xSi$ system we studied the epitaxial growth and characterisation of $Fe_{1-x}Co_xSi$ system with the aim of preserving the properties observed in bulk, finding new and interesting physics in these epitaxially grown system.

CHAPTER 4

Growth and Structural Characterisation

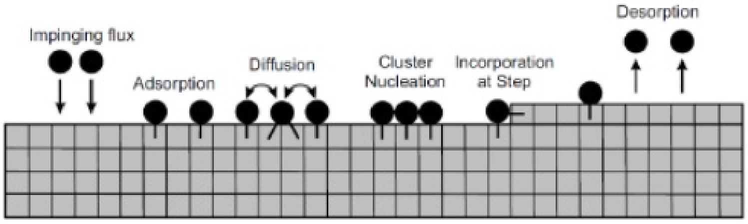

Figure 4.1: The figure above shows the adatom kinetics for basic atomic process of growth. As the impinging flux of atoms hit the surface, processes such as adsorption, diffusion, nucleation, and desorption takes place simultaneously during the growth cycle. [80]

4.1 Molecular Beam Epitaxy

Epitaxy is a process of growing thin films that are crystallographically aligned to the underlying substrate. The epitaxial growth process relies on the thermodynamical properties and adatom kinetics of the incoming target atoms and the substrate. The surface adsorption of the target atoms take place either by transfer of electrons between impinging atoms and the substrate (chemisorption) or by van der Waals interaction (physisorption). Desorption and absorption of adatoms on the substrate takes place simultaneously and is a function of the incoming flux rate, temperature of the substrate, and the source. The ones that are adsorbed can diffuse on the substrate to form the epitaxial film either by forming atomic terraces or by atom cluster nucleation as shown in fig. 4.1. If n is the number of atoms, $\frac{dn}{dt}$ will be the rate at which they are impinging on an unit area of the substrate per unit time. The following equation describes if the epitaxial growth would take place at all:

$$\frac{dn}{dt} = \frac{P}{\sqrt{2\pi mkt}} \tag{4.1}$$

where P is the pressure, k is the Boltzmann constant and m is the mass of the impinging atoms.

Various modes of epitaxial growth has been illustrated in fig. 4.2. When an epitaxial film is grown on a substrate of the same material it is called homoepitaxy, if the film is grown on a chemically different substrate it is called heteroepitaxy. In heteroepitaxy, depending on the lattice mismatch and surface free energy of the materials, the growth modes can be classified into three types as mentioned in fig. 4.3:

(a) Volmer-Weber growth: In this growth model adatom to adatom interactions are

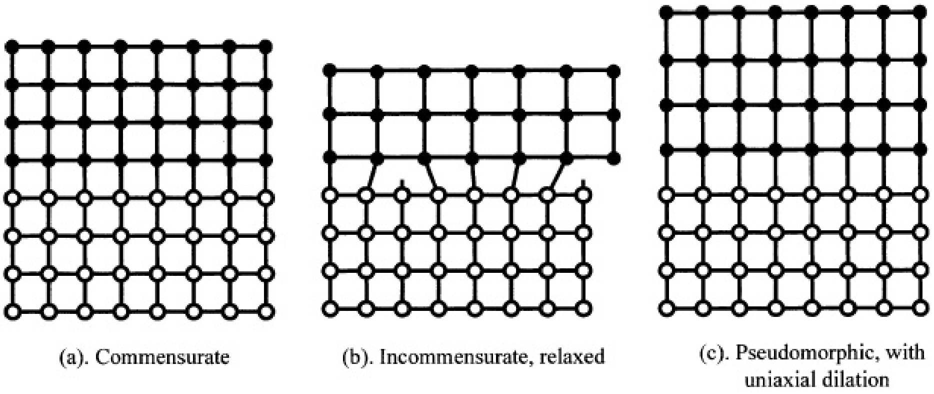

Figure 4.2: Cross-section schematic of atomic arrangement in various modes of epitaxial growth: (a) lattice-matched, commensurate growth; (b) lattice-mismatched, relaxed growth; (c) lattice-mismatched, strained pseudomorphic growth [80].

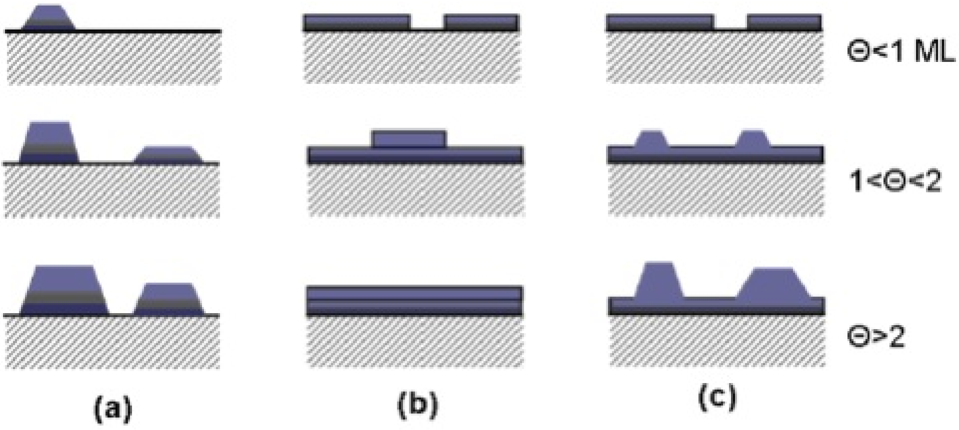

Figure 4.3: Growth mode of thin films: morphology of a growing film for (a) Volmer-Weber growth, (b) Frank-van der Merwe growth and (c) Stranski-Krastanov growth, upon increasing coverage in monolayers (ML).Each mode is shown for several different amounts of surface coverage [80].

much stronger than those of the adatom with the surface, which leads to the formation of three-dimensional adatom structures or islands.

(b) Frank van der Merwe growth: In this growth model adatoms attach themselves to surface and a complete layer of film is formed prior to growth of subsequent layers. This is a layer by-layer growth and is two dimensional in nature, resulting in atomically smooth layers.This is also the ideal condition for the film growth.

(c) Stranski-Krastanov growth: This intermediate growth model is characterized by both two-dimensional (2D) layer by layer and three-dimensional (3D) island growth. Transition from the layer-by-layer to island-based growth occurs at a critical layer thickness and is a function of the chemical and physical properties, such as surface energies and lattice parameters, of the substrate and film.

There are various ways of obtaining an epitaxial film, such as by Chemical Vapour Epitaxy, Liquid Phase Epitaxy, Molecular Beam Epitaxy (MBE) etc. We used MBE to grow high quality, single crystal, epitaxial thin films of FeCoSi by creating a molecular beam of the target material that impinged onto the surface of the substrate, forming an epilayer. MBE requires ultra-high vacuum (UHV) environment, of the order of 10^{-11} mbar which ensures minimum contamination and longer mean free path of the target atoms or molecules. The chemical composition and the atomic layer thickness of the film is controlled by controlling rate of the incoming fluxes. For most of the MBE machines, there are three main chambers in the MBE, a preparatory chamber, a growth chamber and an analysis chamber each of which is equipped with its own vaccum pump systems. The growth chamber maintains a pressure in the range of 10^{-11} mbars. It has three Knudsen cells (K-cells), three electron guns and a manipulator on which the substrate is mounted and rotated for uniform growth. The manipulator is also used for heating the substrate and can go up very high temperatures approx. 1400°C. Often growth chamber has Reflection High Energy Electron Diffraction (RHEED) system to monitor layer by layer growth of the film. On the other hand the analysis chamber is equipped with, Auger Electron Spectroscopy (AES) and Low energy electron diffraction (LEED) systems for various post growth analysis.

Heteroepitaxy implies the epitaxial growth of film on a substrate with different lattice parameter than the film. The lattice mismatch between the film and the substrate results in the film being strained, which is characteristic of a heteroepitaxial growth. There are different ways in which the grown film may be strained. In a commensurate

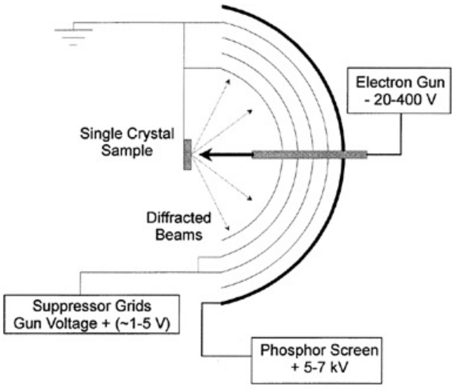

Figure 4.4: Schematic representation of a LEED instrument.

growth, the lattice mismatch is minimum i.e. grown film's lattice parameter is nearly matched with that of the substrate and has least defects in the structure. As the lattice mismatch increases, the film tries to adopt the two-dimensional spacing of the substrate and strains itself more, this is called pseudomorphic growth. If lattice mismatch is very high and strain accommodation is not possible then dislocation defects are formed at the interface and the film adopts its own lattice parameter resulting in a relaxed growth. This is also called Incommensurate growth.

There are various ways of monitoring growth, both insitu and exsitu, which will be described in the following section.

4.1.1 Low energy electron diffraction (LEED)

LEED is based on the detection of coherently backscattered diffracted electrons. A beam of collimated, monoenergetic, and low energy electrons ($\sim 100\ eV$) are accelerated towards the sample to be probed. The spatial distribution of the impinging electrons that are elastically backscattered towards the electron source is determined by the surface structure of the sample. At low electron energy, the diffraction pattern arising from electrons from large ordered domains ($>$ 10 nm) in a sample is very surface sensitive. Thus, the observation of a LEED pattern yields information about the surface structure. LEED analyser was used to give a qualitative insight into the epitaxial structure of the $\mathrm{Fe}_{1-x}\mathrm{Co}_x\mathrm{Si}$ films grown on silicon (111) substrates. The measurement requires UHV and is mounted in the preparation chamber of MBE machine (in-situ). Qualitative and quantitative analysis of the diffraction patterns can throw light on the

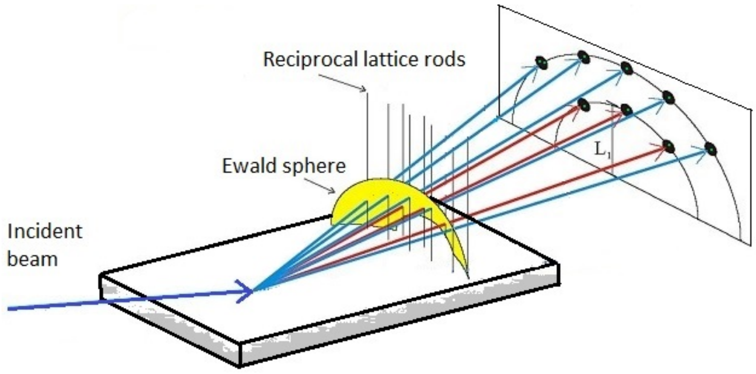

Figure 4.5: Schematic description of the RHEED measurement.

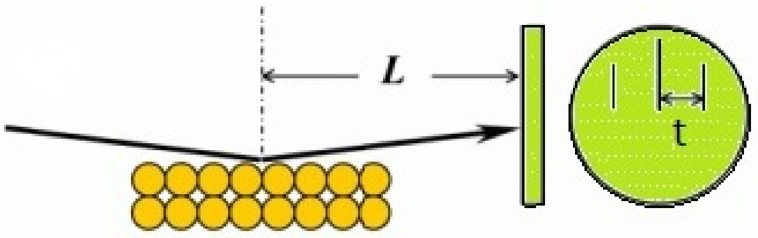

Figure 4.6: Schematic description of the labels used in equation 4.1.2 used to determine the in-plane lattice constant of the film being grown.

orientation of the film with respect to the substrate. In our films the epitaxy in the grown layer is achieved by 30° in-plane rotation of the $Fe_{1-x}Co_xSi$ unit cell relative to the Si unit cell. Figure 4.4 shows a schematic diagram of a LEED instrument. It broadly consists of a electron source, an electron grid and a phosphor screen where the image could be seen.

4.1.2 Reflection high energy electron reflection (RHEED)

Reflection high energy electron diffraction (RHEED) is an in-situ surface sensitive technique that is used to probe the real time surface evolution of an epitaxial film. A schematic of a RHEED system is shown in Figure 4.5. A high-energy electron beam (1.5 A, 20 keV) is incident on the sample surface at a grazing angle between 1^o to 3^o. If K represent the incident electron wave vector, K' the diffracted wave vector then the difference between them can be denoted by $\triangle K$. The incident electron wave vector interacts with the crystal potential, the ones that follows Laue's condition i.e. $\triangle K$ equals inverse lattice vector, interfere constructively and a diffraction pattern is

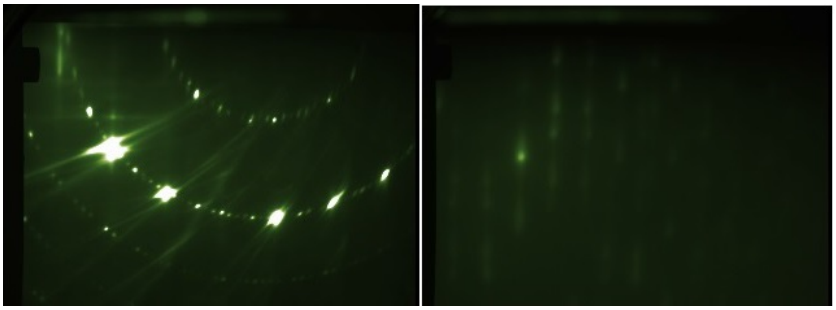

Figure 4.7: RHEED pattern of reconstructed Si 7x7 (left) and $Fe_{1-x}Co_xSi$ epilayer (right), the streaks represents the constructive interference of the beam. They are characteristic of particular system. High intensity streaks are representative of smooth surface. Also, one can find the inter planar lattice plane spacing by analysing the consecutive streaks

obtained and is recorded on a phosphorous screen. The diffracted pattern on the screen is the Fourier transform of the lattice interacting with the beam. We can analyse the diffraction pattern to obtain information about the inter-planar spacing (d) and hence the strain in the heterostructure.

$$d = \frac{L\lambda_o}{t} \tag{4.2}$$

where L is the distance between the sample surface normal and the screen, λ_o is the electron wavelength corresponding to a particular energy and t is the distance between two diffracted streaks observed on the screen. A RHEED pattern can also be used to understand the characteristics of a growing surface (real time): such as the streaks indicating an atomically flat surface, spots that move with sample rotation indicate the atomic smoothness and stationary spots indicating a 3D growth.

4.2 X-ray Techniques

$$\lambda[\mathring{A}] = \frac{hc}{\lambda} = \frac{12.398}{\varepsilon[keV]} \tag{4.3}$$

X-rays are electromagnetic waves with wavelength in the range of nano meters corresponding to the photon energy (ε) of 120 keV-6 keV as given by the equation 4.2. When an X-ray photon interacts with an atom it is either absorbed or scattered, and when it interacts with a material medium which can be treated as a continuum of atoms, it is either reflected or refracted from the material interface.

4.2.1 Scattering

The interaction of electromagnetic field of X-rays with the electrons present in a material gives rise to X-ray scattering or X-ray diffraction. Upon interaction with a material having a periodicity in space the scattering may give rise to constructive interference. The periodicity in thin films correspond to the separation between the atomic layers of different electron densities and in a crystal, the repetition of atoms from unit cells. The angle of coherent interference θ arising from the diffraction of X-rays from two scattering centres with a separation d, obeys Bragg's law [81]

$$n\lambda = 2d\sin\theta \tag{4.4}$$

Where n is the index of the diffraction and λ is the wavelength of the X-ray used. The equation however does not help us to find the intensity of the scattering. Therefore to estimate the intensity of the scattering ($|F^{crystal}|^2$) in a crystal structure for a constructive interference we use the following equation,

$$F^{crystal}(Q) = \Sigma f_j(Q)e^{iQ.r_j}\Sigma e^{iQ.R_n} \tag{4.5}$$

where Q is the scattering vector and $f_j(Q)$ represents the atomic form factor of the j'th atom. R_n are the lattice vectors that define the lattice basis and r_j are the position vectors of the atom such that all the atoms in the crystal can be mapped by $R_n + r_j$. The first term in the equation represents the Unit cell structure factor and gives the intensity of the allowed reflection. The second term is dependent on the lattice structure, gives the lattice sum, and is representative of the position of diffraction peaks and their distribution in the reciprocal space. The lattice sum would equal unity unless the scattering vector satisfies the following condition:

$$Q \cdot R_n = 2\pi \times integer \tag{4.6}$$

R_n, the lattice vector can be written as

$$R_n = n_1 a_1 + n_2 a_2 + n_3 a_3 \tag{4.7}$$

where (a_1, a_2, a_3) are the basis vectors and (n_1, n_2, n_3) are integers. For an unique solution to the equation 4.2.1, we use the concept of reciprocal lattice, the reciprocal lattice vectors are given by the following equations

$$a_1^* = 2\pi \frac{a_2 \times a_3}{a_1 \cdot (a_2 \times a_3)}, \quad a_2^* = 2\pi \frac{a_3 \times a_1}{a_1 \cdot (a_2 \times a_3)}, \quad a_3^* = 2\pi \frac{a_1 \times a_2}{a_1 \cdot (a_2 \times a_3)} \tag{4.8}$$

Any lattice site in the reciprocal lattice can be mapped by the following relation

$$G = ha_1^* + ka_2^* + la_3^* \tag{4.9}$$

where (h,k,l) are integers. The product of G and R_n gives us the following,

$$G.R_n = 2\pi(hn_1 + kn_2 + ln_3) = 2\pi \times integer \tag{4.10}$$

On comparing the equation with equation 4.2.1, we find the following solution

$$Q = G \tag{4.11}$$

This implies that for diffraction to take place the scattering vector should equal the reciprocal lattice vector. This is also known as Laue condition and is equivalent to Bragg's law.

4.2.2 Absorption

X-ray absorption is based on the principle of photoelectric effect wherein an x-ray photon is absorbed by an atom, the excess energy is subsequently transferred to an electron such that the electron is then expelled from the atom leaving the atom ionised. When the vacancy or hole thus created is filled by an electron at a higher energy level, emitting a photon, the process is called florescence. However, if the energy that was used to emit the photon is rather used to expel another electron from the atom, the process is called Auger electron emission. The photoelectric absorption cross-section varies as a function of atomic number (Z) of the absorber, given by $\propto$ Z^4. Absorption can be quantified using the linear absorption coefficient μ. If dz be the infinitesimal thickness of the material at a depth z from the surface, μdz would be the attenuation of the incident beam. The absorption equation can then be written as

$$-dI = I(z)\mu dz, \tag{4.12}$$

Let $I(z = 0) = I_0$ be the incident beam intensity at $z = 0$, the solution to the differential equation is the following, using which μ can experimentally determined.

$$I(z) = I_0 e^{-\mu z}, \tag{4.13}$$

4.2.3 Refraction

The phenomena of refraction takes place at the interface of two matter having different refractive indices (n). The matter can be assumed to be homogeneous, having uniformly distributed scattering centres, and boundaries separating them to be sharp at the interface. The refractive index of vacuum is 1 and that of optically transparent materials for visible wavelengths ranges between 1.2 and 2. For X-rays the refractive index can be written as the following

$$n = 1 - \delta + i\beta, \tag{4.14}$$

where δ is of the order of 10^{-5} in solids and 10^{-8} in air. β is imaginary and is smaller than δ. Therefore n is less than unity for X-rays. Since the velocity in a material is given by c/n, it would seem to imply that the light travels faster in a medium than in vacuum. this however is not the case as c/n is the phase velocity, not the group velocity which is evaluated as $d\omega/dk$, and is less than c.

Quantitatively refraction can be defined by Snell's law that relates the incident grazing angle α to the refracted angle $\alpha^{'}$ by the equation below.

$$\cos\alpha = n\cos\alpha^{'}, \tag{4.15}$$

A refractive index less than unity leads to total external reflection. The X-rays upon entering a medium are refracted away from the normal and in the case of total internal reflection they don't penetrate into the medium and are completely reflected

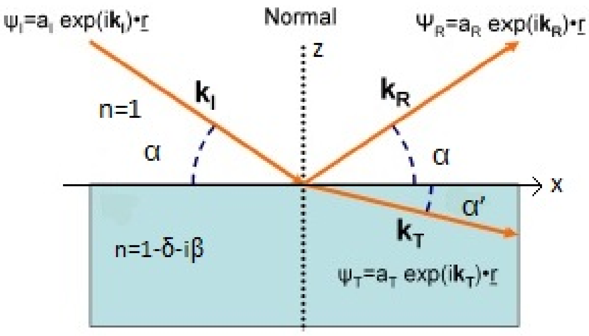

Figure 4.8: A plane wave (k_I) is incident on the boundary between two homogenous, isotropic, and lossless media; k_R and k_T are the reflected and transmitted waves respectively.

back. The incident glancing angle less than which the total external reflection takes place, is called the critical angle α_c and can be numerically obtained by expanding the equation above and assuming β to be zero, it is then given by,

$$\alpha_c = \sqrt{2\delta} \tag{4.16}$$

4.2.4 Reflection

We consider reflection from a homogeneous slab of finite thickness as shown in fig 4.8. Let the wave vector k_i be incident at an angle α_i, its amplitude be a_i, in a similar way we can describe the parameters for transmitted wave k_T (amplitude be a_T) making an angle $\alpha^{'}$ and reflected wave k_R (amplitude be a_R) making an angle α_r with the surface parallel to the slab. We consider a particular case of specular reflection wherein $\alpha_i = \alpha_r = \alpha$. In the X-ray region, Snell's law (eq 4.2.4) and Fresnel's (eq 4.2.4) equations can be derived by imposing boundary conditions i.e the inplane component (k_x) of the wave vectors and its derivatives should be continuous at the interface of the slab. We thus arrive to the equations below (readers can refer to text by Als-Nielsen and Des MacMorrow for detailed derivation [81])

$$\cos\alpha = n\cos\alpha^{'} \tag{4.17}$$

and

$$r \equiv \frac{a_R}{a_I} = \frac{\alpha - \alpha^{'}}{\alpha + \alpha^{'}} \qquad t \equiv \frac{a_T}{a_I} = \frac{2\alpha}{\alpha + \alpha^{'}} \tag{4.18}$$

To determine the slab thickness(Δ or r_{slab}) we consider multiple reflection from the surface of the slab as well as transmission across its interface. Taking into account the phase shift during transmission and summing over the all the possible cases of transmission and reflection, we obtain a geometric series that converges to the equation below, yielding an expression for total amplitude reflectivity.

$$r_{slab} = \frac{r_{01} + r_{12}p^2}{1 + r_{01}r_{12}p^2} \tag{4.19}$$

Where $p^2 = e^{iQ\Delta}$ is the phase factor of the rays reflected from the top and bottom of the slab, Δ is the thickness of the slab, r_{01}, and r_{12} are the reflections at the top and bottom interfaces of the slab respectively. The reflected intensity $\|r\|^2$ is plotted against the scattering vector Q in fig 4.9. The oscillations or the Kiessig fringes are due to the constructive (in phase) and destructive (out of phase) interference from the top and bottom interfaces of the slab. The angular separation of Kiessig fringes can be used to obtain the thickness of the slab as shown in fig 4.10 by using the Kiessig equation,where θ_c is the critical angle,θ_n is the angle of the n^{th} peak

$$n\lambda = 2\Delta(\sin^2\theta_n - \sin^2\theta_c)^{1/2} \tag{4.20}$$

A Bruker D8 Discover system was used at Leeds, the x-ray beam is produced from a Cu anode, collimated via slits and, passed through a monochromator to obtain the characteristic Cu Kα wavelength (1.54 $\AA$). The filtered beam is then passed through a scintillator detector and finally through the data logger. The system is equipped with a Eulerian-cradle, a five-axis (x-y-z- $\chi - \phi$) precision sample stage. High incidence angle scans in a symmetric $\theta - 2\theta$ mode were used to determine the out of plane interplanar distance of the planes lying parallel to the sample surface. In such a scan the angle θ of the incident beam with respect to the sample surface is varied, keeping the detector angle at 2θ with respect to the incident beam. The scan reveals information about the crystal structure, film quality, crystallographic orientation etc. of the crystal lattice. One such spectrum is shown in fig 4.11. Grazing angle incidence X-ray diffraction, where beam is almost parallel to the surface of the film, was used to determine the inplane orientation of the crystal lattice and hence the associated lattice parameters.

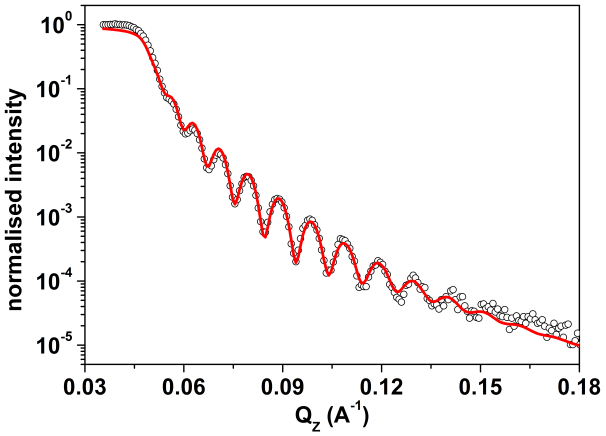

Figure 4.9: Kiessig fringes as obtained from an epitaxially grown $Fe_{1-x}Co_xSi$ film. The fringes arise due to the constructive interference from the film. The solid curve shows the calculated reflectivity ($\|r\|^2$) as a function of scattering vector Q, surface roughness of the film can also be determined from the fitted curve. The periodicity of these fringes can be used to determine the thickness of the film grown on the substrate.

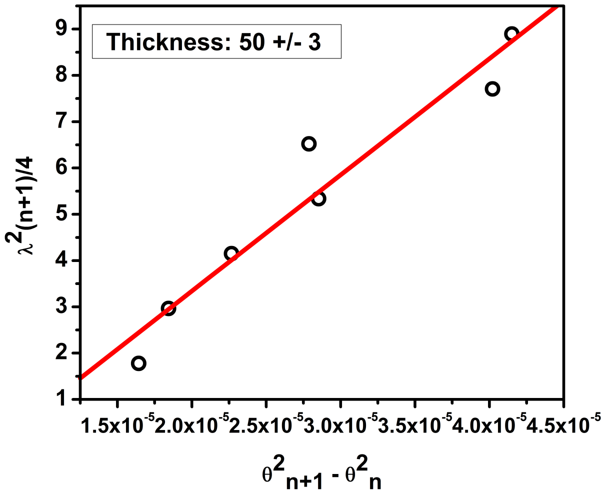

Figure 4.10: Film thickness (nm) was calculated from the adjacent Kiessig fringes for a epitaxially grown $Fe_{0.5}Co_{0.5}Si$ thin film. The red line shows the linear fit of the data points that were obtained from fig 4.9.

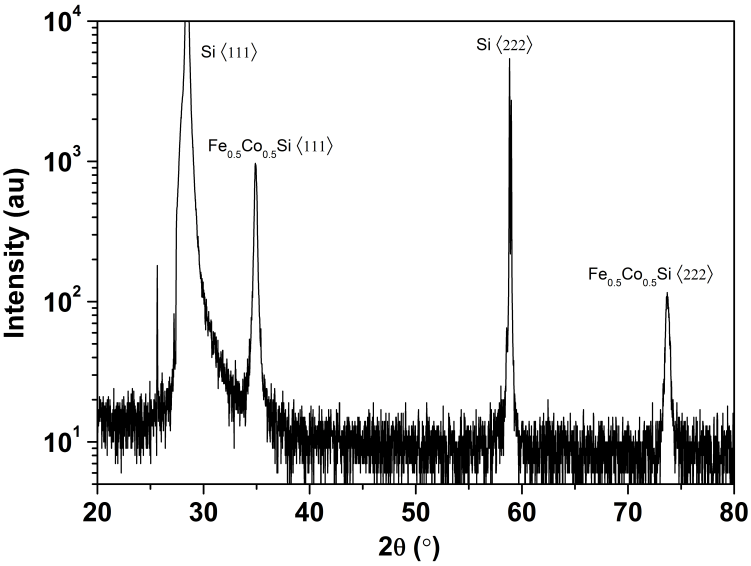

Figure 4.11: A high angle scan of $\mathrm{Fe}_{1-x}\mathrm{Co}_x\mathrm{Si}$ epilayer with $x = 0.5$. One can see the characteristic (111) and (222) B20 peaks aligned parallel to corresponding Si peaks.

4.3 Atomic force microscopy

AFM is a scanning probe microscopy (SPM) technique that is used to map the surface topology by measuring the short range van der Waals interaction between the tip and the sample surface. The tip is made of either Si or SiN is mounted normal to the cantilever. The cantilever used was approx. $125\mu\ m$ long, $40\mu\ m$ wide, had a resonating frequency of 320 kHz, and stiffness/spring constant(k) of 42 N/m. We used the tapping mode of AFM tip, the other two modes being contact and non-contact. The tapping mode overcomes problems associated with friction, adhesion, electrostatic forces by placing the tip in contact with the surface to provide high resolution and then lifting the tip off the surface to avoid dragging. The resonating frequency ω of the tip is given by the following equation

$$\omega_o = \sqrt{k/m}, \tag{4.21}$$

During the scan the tip experiences van der Waals forces that leads to modification of the resonating frequency to the following

$$\omega = \omega_o \sqrt{1 - \frac{\partial F}{\partial z}}, \tag{4.22}$$

where $\partial F/\partial z$ is the minimal detectable force gradient.

$$\frac{\partial F}{\partial z} = \frac{1}{A}\sqrt{\frac{4B\kappa K_B T}{\omega_o Q}}, \tag{4.23}$$

where A is the rms (root mean square) oscillation amplitude, B the detection bandwidth, and $Q = \Delta\omega/\omega$ the quality factor of the resonance. The oscillating frequency of the cantilever is monitored by a laser beam reflected from top of the tip and then incident onto a photodetector. The oscillating amplitude is kept constant using a piezoelectric actuator and a PID regulator controls the tip-sample distance, maintaining a constant oscillation amplitude. The laser beam tracks the motion of the tip and using a computer software a topographic image of the sample surface is thus obtained.

4.4 Transmission electron microscopy

A TEM has a tungsten filament on top that acts as an electron source. A voltage of the order of 100-300 keV is applied to the filament to generate a high energy electron beam by thermionic emission. The beam then passes through a vacuum chamber where pairs of electromagnetic lens are used to focus the beam and vary the spot size before transmitting it through the sample. The sample to be measured has to be thin enough so as the electron beam passes through it. For our experiments, the samples were prepared in Institute of Material Science, Univ. of Leeds using Focussed Ion Beam (FIB). The scattered and diffracted electrons are then focussed onto a phosphor detector and an image is obtained. Various qualitative and quantitative analyses could be done. We used the images to confirm the epitaxial growth and perform strain analysis. Element specific Energy-dispersive X-ray spectroscopy (EDS or EDX) was done to verify the chemical composition of the films which are in good agreement with what we expected.

4.5 Elastic Properties/Stress and Strain

In solids stress can be defined as force acting per unit area. When a body undergoes stress, the elastic properties of the material determines the corresponding strain response. Within the framework of linear elastic limit, stress and strain tensors are related by Hooke's law as follows

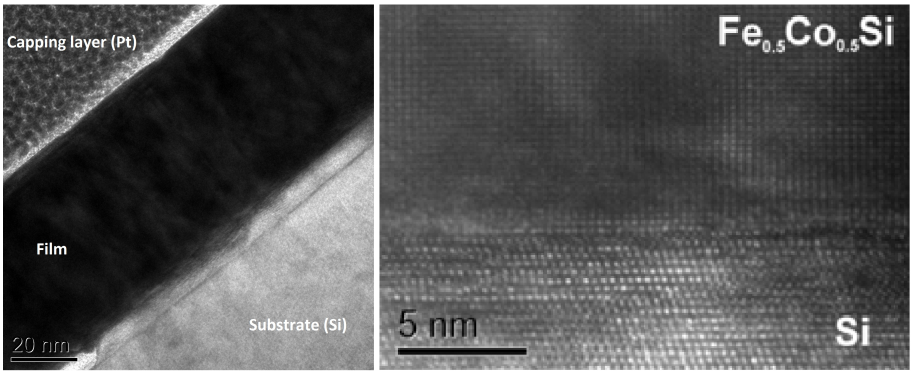

Figure 4.12: Fe$_{1-x}$Co$_x$Si epilayer with $x = 0.5$ on the [112] zone axis, showing the upper (left) and lower (right) interfaces. The film can be seen to be an epitaxial single crystal.

$$\sigma_{ij} = C_{ijkl}\varepsilon_{kl}, \tag{4.24}$$

$$\varepsilon_{ij} = S_{ijkl}\sigma_{kl}, \tag{4.25}$$

where σ_{ij} and ε_{ij} are the components of the stress and the strain tensors, C_{ijkl} and S_{ijkl} constitute the stiffness and compliance tensors respectively. The stress component σ_{ii} for which the force is acting on the ith face and is normal to the ith face is called normal component and the σ_{ij}, where $i \neq j$ for which force acting on the jth face is parallel to the ith face is called a shear component. Stress forms a nine component symmetrical 2nd rank tensor which can be written in the matrix form as shown below

$$\sigma_{ij} = \begin{bmatrix} \sigma_{11} & \sigma_{12} & \sigma_{13} \\ \sigma_{21} & \sigma_{22} & \sigma_{23} \\ \sigma_{31} & \sigma_{32} & \sigma_{33} \end{bmatrix} \tag{4.26}$$

The number of stress components can be reduced from nine to six under static situation when angular acceleration vanishes and therefore the total torque equals zero ($\sigma_{ij} = \sigma_{ji}$).

If $x_{i,j,k}$ represents the Cartesian coordinates x, y, and z respectively, the displacement in each of the coordinates is represented by $v_{i,j,k}$, the external forces acting on the material causing a deformation can then be described by the strain tensor:

$$\varepsilon_{ij} = \begin{bmatrix} \varepsilon_{11} & \varepsilon_{12} & \varepsilon_{13} \\ \varepsilon_{21} & \varepsilon_{22} & \varepsilon_{23} \\ \varepsilon_{31} & \varepsilon_{32} & \varepsilon_{33} \end{bmatrix} \tag{4.27}$$

where

$$\varepsilon_{ii} = \lim_{x_i \to 0} \frac{\delta v_i}{\delta x_i} \tag{4.28}$$

and

$$\varepsilon_{ij} = \frac{1}{2}\left(\lim_{x_i \to 0} \frac{\delta v_j}{\delta x_i} + \lim_{x_i \to 0} \frac{\delta v_i}{\delta x_j} \right) \tag{4.29}$$

The elastic stiffness tensor or the moduli of elasticity C_{ijkl} describes the physical property of the material. The C_{ijkl} is a fourth rank tensor, has 81 components and relates strain and stress. Because of stress and strain symmetries the number of the component it transforms into a rank 2, thirty six component tensor (using Voigt notations). For a cubic crystal the stiffness tensor has three independent components:

$$C_{cubic} = \begin{bmatrix} C_{11} & C_{12} & C_{12} & 0 & 0 & 0 \\ C_{12} & C_{11} & C_{12} & 0 & 0 & 0 \\ C_{12} & C_{12} & C_{11} & 0 & 0 & 0 \\ 0 & 0 & 0 & C_{44} & 0 & 0 \\ 0 & 0 & 0 & 0 & C_{44} & 0 \\ 0 & 0 & 0 & 0 & 0 & C_{44} \end{bmatrix} \tag{4.30}$$

Values of some elastic constants for transition metal silicides are shown in the fig. 4.13. For isotropic body the C_{ijkl} constants depend only on two parameters (Young's modulus and Poisson's ratio), and they do not change with direction in the body.

4.6 Result and Discussion

The $Fe_{1-x}Co_xSi$ thin films were prepared by simultaneous co-evaporation of Fe, Co, and Si by molecular beam epitaxy (MBE) on a lightly n-doped silicon (111) substrates with 2000-3000 Ωcm resistivity at room temperature. The level of Co-doping x of the various $Fe_{1-x}Co_xSi$ films was determined by controlling the individual rates of incoming flux. We adopted the growth protocol described in ref. [14]. The base pressure of growth

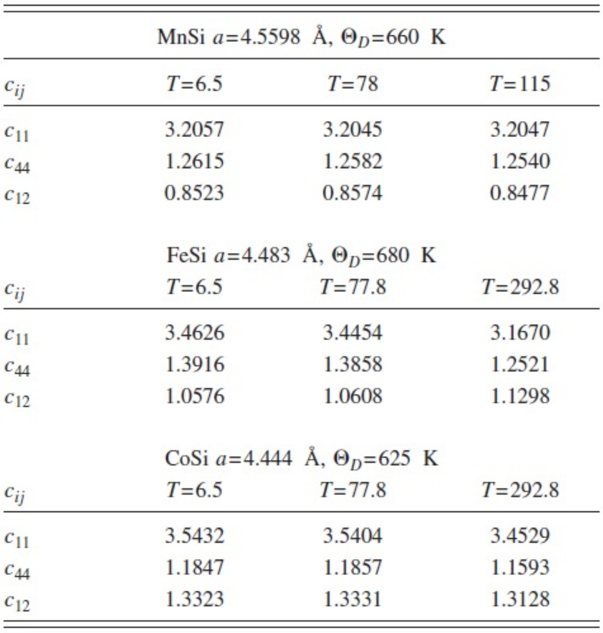

	MnSi a=4.5598 Å, Θ_D=660 K		
c_{ij}	T=6.5	T=78	T=115
c_{11}	3.2057	3.2045	3.2047
c_{44}	1.2615	1.2582	1.2540
c_{12}	0.8523	0.8574	0.8477
	FeSi a=4.483 Å, Θ_D=680 K		
c_{ij}	T=6.5	T=77.8	T=292.8
c_{11}	3.4626	3.4454	3.1670
c_{44}	1.3916	1.3858	1.2521
c_{12}	1.0576	1.0608	1.1298
	CoSi a=4.444 Å, Θ_D=625 K		
c_{ij}	T=6.5	T=77.8	T=292.8
c_{11}	3.5432	3.5404	3.4529
c_{44}	1.1847	1.1857	1.1593
c_{12}	1.3323	1.3331	1.3128

Figure 4.13: The table above shows the elastic constants of MnSi, FeSi, and CoSi, Debye temperature (Θ_D), calculated from the elastic constants. [82]

chamber was maintained in the range of 2.8-4.8$\times10^{-11}$ mbar. Prior to the deposition of the film, the substrates were annealed at 1200°C until a well ordered 7×7 reconstructed Si (111) surface was obtained. The Si(111)-7×7 reconstructed surface lowers the energy of the surface and can be explained by the DAS (dimer-adatom-stacking fault) model [83].

The reconstruction affects the surface atom layer and the top four layers, resulting in a diamond shaped 7 × 7 unit cell. As per this model, each diamond shaped unit

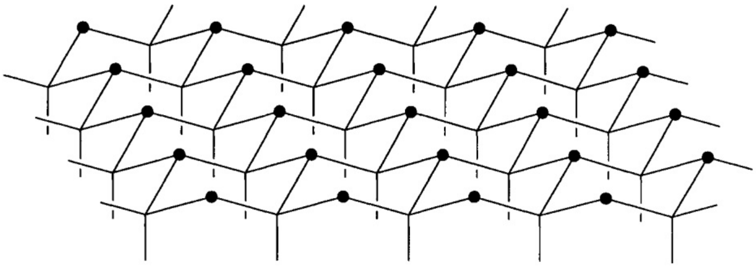

Figure 4.14: Structure of unreconstructed Si (111) surface with dangling bonds marked with a dot (•)[83].

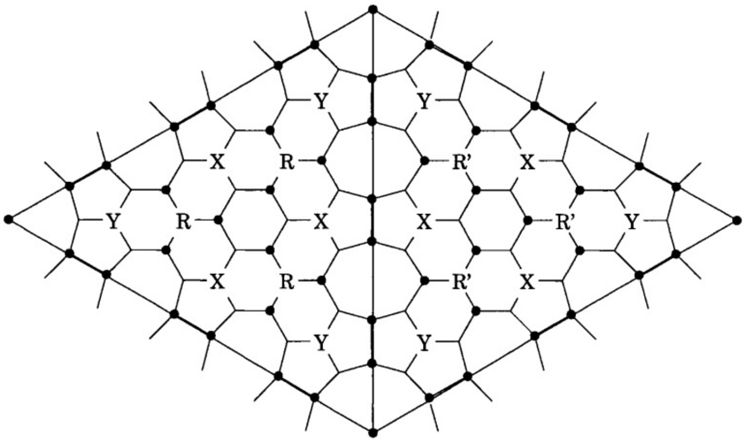

Figure 4.15: Top view of the reconstructed Si(111)-(7x7) surface due to the DAS model. Six adatoms are marked X, six corner adatoms are marked Y, R and R' are the rest atoms, [83].

cell consists of two triangular subunits each surrounded by nine Si dimers. On the surface there are six triply coordinated Si atoms divided equally between faulted half subunit and unfaulted half subunit cell, also called rest atoms. The top layer has twelve adatoms, six corner adatom and six centre adatoms. Each 7x7 unit cell contains 19 dangling bonds against the 49 originally contained in the unreconstructed unit cell: 12 for the adatoms, six for the rest atoms and one for the atom in the center of the corner hole. A low energy electron diffraction pattern demonstrating this reconstruction is shown in Fig. 4.16(c). The films were then grown by depositing a seed layer of Fe of $\sim$ 5.4 Å thickness at room temperature, followed by the deposition of a $\sim$ 50 nm thick $\mathrm{Fe}_{1-x}\mathrm{Co}_x\mathrm{Si}$ layer at a net flux rate of $\sim$ 0.4 Å/s at 400°C. The films were then further annealed at 400°C for 15 minutes, before being allowed to cool to room temperature for further characterization.

The films grew in the (111) orientation, as can be seen from the Cu K_α X-ray diffraction (XRD) spectrum shown in Fig. 4.16(a), and are ϵ-phase pure. In-plane epitaxy of the $\mathrm{Fe}_{1-x}\mathrm{Co}_x\mathrm{Si}$ films is seen to be achieved by a 30° in-plane rotation of the surface unit cell with respect to the Si, such that the $\mathrm{Fe}_{1-x}\mathrm{Co}_x\mathrm{Si}$ $[11\bar{2}]$ direction is aligned parallel to Si $[1\bar{1}0]$, demonstrated by the LEED pattern of a completed epilayer in Fig. 4.16(d). Atomic force microscopy (AFM) was used to map the surface topography of the films: an representative micrograph is shown in Fig. 4.16(b). The r.m.s. roughness of the films were estimated from these images to be around 1 nm.

For further structural verification, high resolution transmission electron microscopy

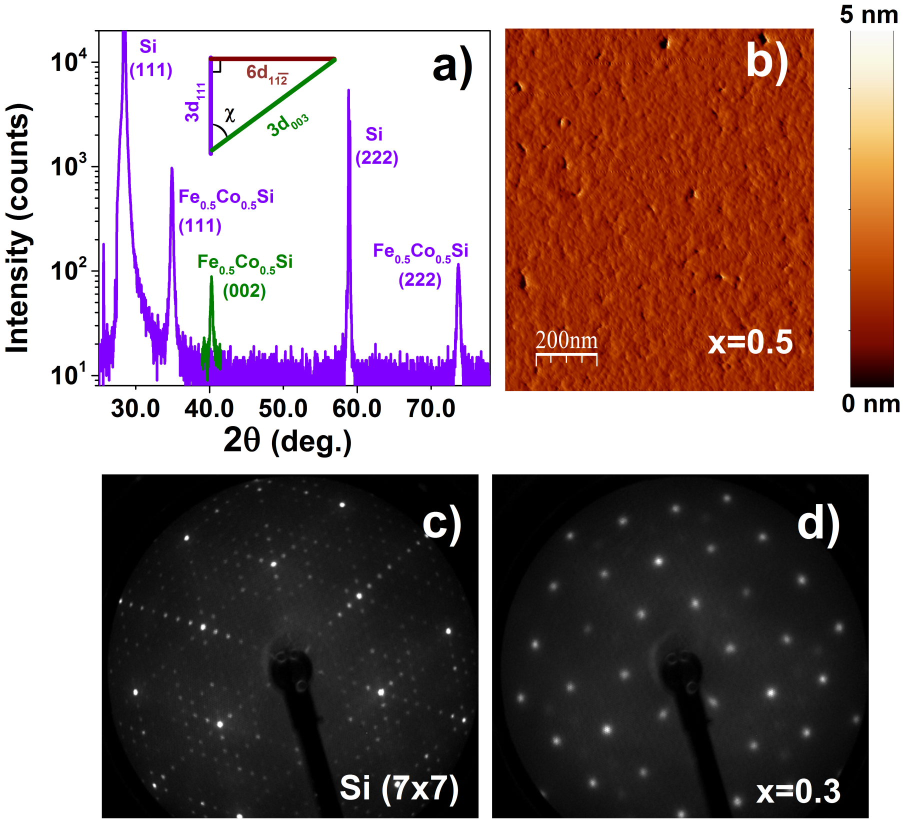

Figure 4.16: Structural characterization of the 50 nm thick $Fe_{1-x}Co_xSi$ epilayers. (a) Specular XRD spectrum of a $x = 0.5$ film, illustrating the phase purity of the B20 structure and the (111) epitaxial orientation of the film. A scan showing the off-specular (002) peak at the appropriate detector angle 2θ is also shown, with the geometrical relationship between the lattice constants measured by these two crystallographic peaks shown as an inset, defining an angle χ between the two crystallographic directions. (b) Atomic force micrograph of the top surface of an $Fe_{1-x}Co_xSi$ epilayer with $x = 0.5$. The r.m.s. roughness is ~ 1 nm. (c) LEED pattern of an annealed Si (111) substrate prior to film growth. The 7×7 surface reconstruction is evident. (d) LEED pattern from an $Fe_{1-x}Co_xSi$ film $x = 0.3$, demonstrating epitaxial growth in the (111) orientation.

(HRTEM) and energy dispersive X-ray analysis (EDX) were carried out on cross-section specimens prepared by focussed ion beam (FIB). Fig. 4.17(a) and (b) show the top and bottom interfaces of a $\mathrm{Fe}_{1-x}\mathrm{Co}_x\mathrm{Si}$ film with $x = 0.5$. The films look well-ordered throughout and epitaxial growth can be observed with the orientation:
$(111)\mathrm{Fe}_{1-x}\mathrm{Co}_x\mathrm{Si}\|(111)\mathrm{Si} : [11\bar{2}]\mathrm{Fe}_{1-x}\mathrm{Co}_x\mathrm{Si}\|[1\bar{1}0]\mathrm{Si}$.
Sample cross sections were mapped with EDX which confirmed the homogeneous chemical composition of the films.

We also measured plan-view TEM sections made by mechanical polishing. The diffraction along the [111] surface normal for a $\mathrm{Fe}_{1-x}\mathrm{Co}_x\mathrm{Si}$ epilayer with $x = 0.3$ is shown in Fig. 4.17(c). Double diffraction arising from the incommensurate film and substrate lattices is observed surrounding the primary diffraction spots. An enlargement of the spot circled in panel (c) is shown in Fig. 4.17(d) from which a line scan (depicted in Fig. 4.17(e)) was used to determine the spot separation. From this double diffraction spot separation Δg, and using the methods of Karhu *et al.*,[27] the in-plane strain for this particular layer, averaged over the 50 nm film, was determined to be 0.92 ± 0.07 %.

4.7 Strain characterization

Heteroepitaxy gives rise to strained growth of films as a result of the lattice mismatch between substrate and the film. The lattice parameter of Si is 5.431 Å, whilst that of bulk FeSi is 4.482 Å, falling to 4.4635 Å for $\mathrm{Fe}_{0.5}\mathrm{Co}_{0.5}\mathrm{Si}$. It is to accommodate this large difference that the film grows with the 30° in-plane rotation demonstrated above by LEED (see fig. 4.16(c) and 4.16(d)) and HRTEM (Fig. 4.17(b)). This gives rise to an in-plane lattice mismatch at the interface that is 4.98 % for FeSi, rising to 5.35 % for $\mathrm{Fe}_{0.5}\mathrm{Co}_{0.5}\mathrm{Si}$. The heteroepitaxy induces biaxial tensile strain in the in-plane directions of the $\mathrm{Fe}_{1-x}\mathrm{Co}_x\mathrm{Si}$ layers, with corresponding compression in the out-of-plane direction, which distorts the cubic B20 lattice to have a rhombohedral form.

The position of the $\mathrm{Fe}_{1-x}\mathrm{Co}_x\mathrm{Si}$ [111] and [222] Bragg peaks, obtained from θ-2θ high angle XRD scans, were used to determine the out-of-plane [111] inter-planar spacing of our $\mathrm{Fe}_{1-x}\mathrm{Co}_x\mathrm{Si}$ films using Braggs' law. We define the parameter d_{hkl} as a measured interplanar spacing associated with a particular set of lattice planes (hkl). A systematic decrease in out-of-plane inter-planar spacing, d_{111} is observed with increasing Co content x in the films, as shown in Fig. 4.18(a). The linear variation of the out-of-plane lattice parameter with x shows that Vegard's law [84] is followed, as is

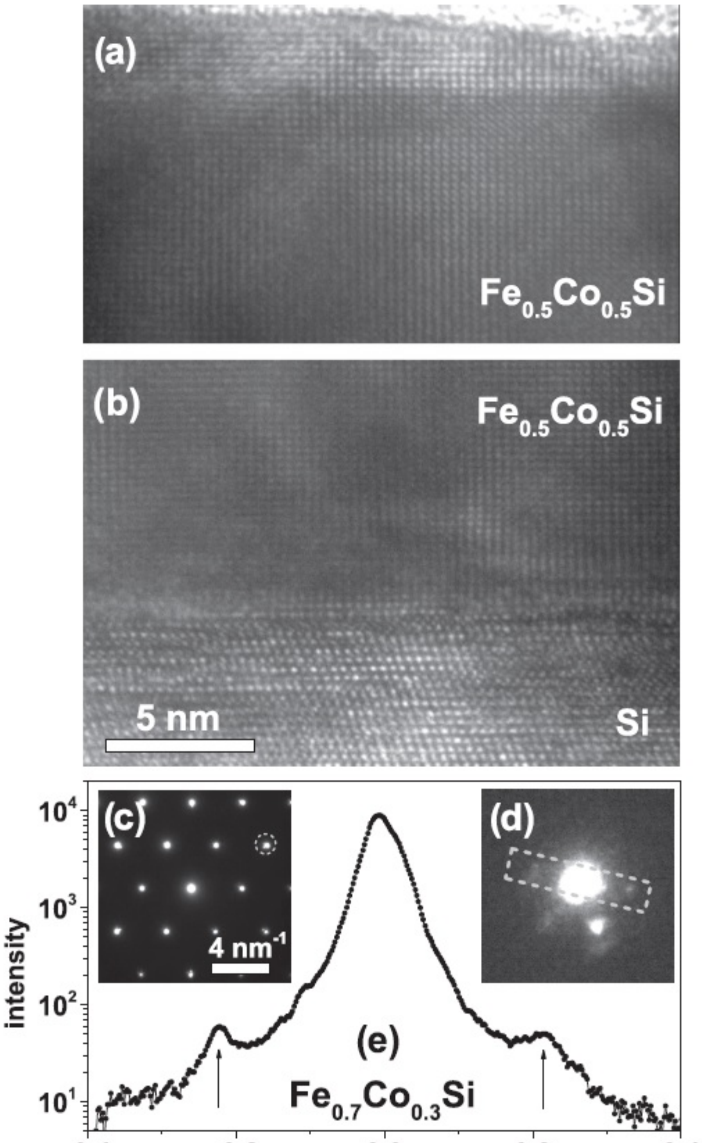

Figure 4.17: HRTEM analysis of (a-b) an $x = 0.5$ epilayer cross-section and (c-e) an $x = 0.3$ plan view section. (a) Surface of the $Fe_{0.5}Co_{0.5}Si$ layer viewed along the $[11\overline{2}]$ zone axis. (b) $Fe_{0.5}Co_{0.5}Si$ [112]/Si $[1\overline{1}0]$ interface, viewed along the same same zone axis for the epilayer. (c) Plan view diffraction pattern of $Fe_{0.7}Co_{0.3}Si$ viewed along the [111] zone axis. The double diffraction pattern from the combined Si $[20\overline{2}]$ and $Fe_{0.7}Co_{0.3}Si$ $[\overline{1}2\overline{1}]$ spot circled in (c) is shown enlarged in (d). (e) A line scan, arising from intergrating across the strip marked by a dashed line in (d), through the double diffraction spots (indicated by arrows, which are separated by $2\Delta g$).

the case in bulk crystals of this material.[85] However, there is also the large in-plane lattice mismatch with the Si substrate that was discussed above in the case of thin films. In order to determine this in a consistent manner, the [002] peak was found and measured (see Fig. 4.16(a)) to yield d_{002}, which can then be used to calculate the in-plane inter-planar spacing $d_{11\bar{2}}$. This is plotted as a function of x in Fig. 4.18(b). This is seen to be of similar size (~ 1 %) as that measured using double diffraction in the plan-view TEM. The small discrepancy at $x = 0.3$ between the values measured with the two techniques can be attributed to the fact that these are two different samples, and that the thinning of the substrate needed for TEM means that there can be some strain relaxation in both film and substrate that is not possible when a bulk substrate is used.

Based on data from Fig. 4.18(a) and 4.18(b), the out-of-plane compressive, $\varepsilon_{\perp}$, and in-plane tensile, $\varepsilon_{\parallel}$, strains in the crystal structure were calculated using the following expression:

$$\varepsilon^{hkl} = \frac{d_{hkl}^{\mathrm{epi}} - d_{hkl}^{\mathrm{bulk}}}{d_{hkl}^{\mathrm{bulk}}}, \tag{4.31}$$

where d_{hkl}^{epi} is the inter-planar spacing as measured for a given epilayer and d_{hkl}^{bulk} is the corresponding bulk inter-planar spacing.[37] The results are shown in Fig. 4.18(c) and (d). In both the cases strain follows a nonlinear relationship with the Co-doping level x. For higher values of x the lattice is more compressed out-of-plane, whilst it is less expanded in-plane.

The XRD and plan-view TEM methods we have used to determine the in-plane inter-planar spacings give information averaged over the film depth. Inspection of the TEM image shown in Fig. 4.17(b) indicates that at the interface the film is fully strained as the lattice fringes are coherent on both sides of the interface. Nevertheless, it is clear that this situation does not persist to any significant depth into the film, which soon relaxes to its own strained lattice constant for a rhombohedral crystal structure which is somewhere in between that of Si and the $\mathrm{Fe}_{1-x}\mathrm{Co}_x\mathrm{Si}$ cubic assumption of crystal structure. This is shown as a function of x in Fig. 4.19(a), where the layer-averaged $d_{11\bar{2}}$ (determined form XRD) in our layers is seen to be slightly strained away from the bulk value towards d_{220} in the Si substrate. The variation of volume strain with shear strain in $\mathrm{Fe}_{1-x}\mathrm{Co}_x\mathrm{Si}$ film is shown in the Fig. 4.19(b) for various Co doping ranging from $x = 0$ to $x = 0.5$. The linearity in the relationship confirms that the epitaxial strain in $\mathrm{Fe}_{1-x}\mathrm{Co}_x\mathrm{Si}$ film changes only the angle of the unit cell as shown in Fig. 4.18(f)

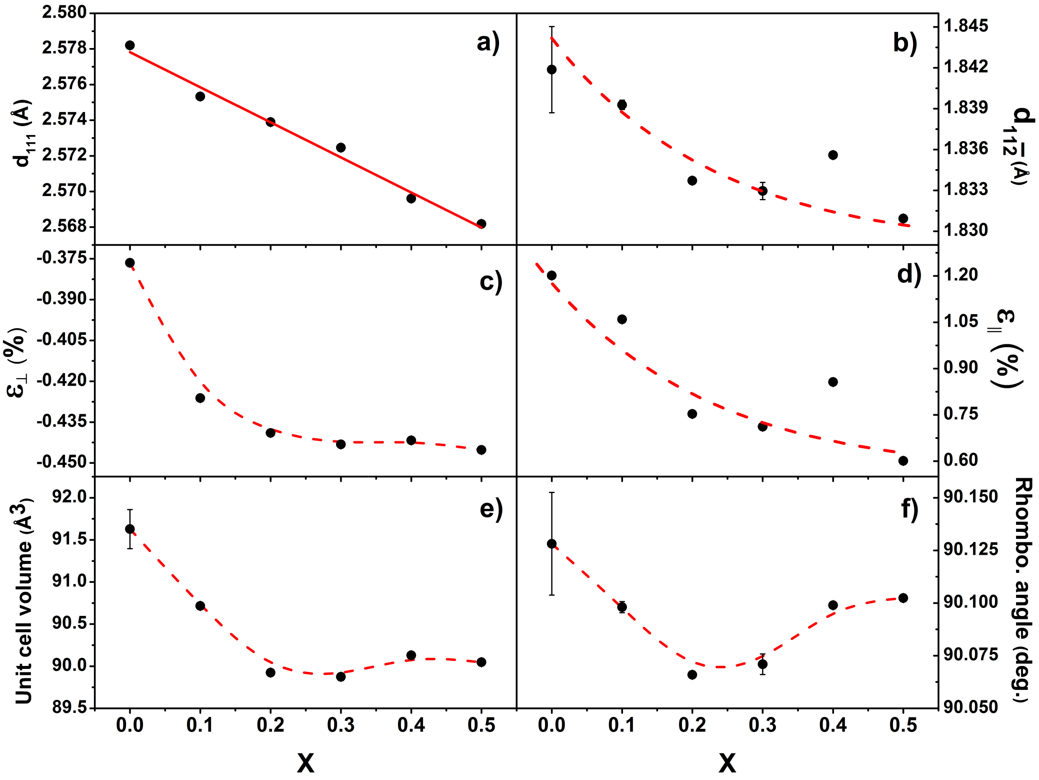

Figure 4.18: Strain analysis. (a) Out-of-plane inter-planar spacing d_{111} of $Fe_{1-x}Co_xSi$ films based on data from XRD, which is seen to follow the Vegard's law. (b) In-plane inter-planar spacing $d_{11\bar{2}}$, based on data from XRD. (c) Out-of-plane of strain determined from data in (c). (d) In-plane strain determined from data in (b). (e) Rhombohedral unit cell volume as a function of x. (f) Rhombohedral angle as a function of x. The solid line is a linear fit; the dashed lines are guides to the eye.

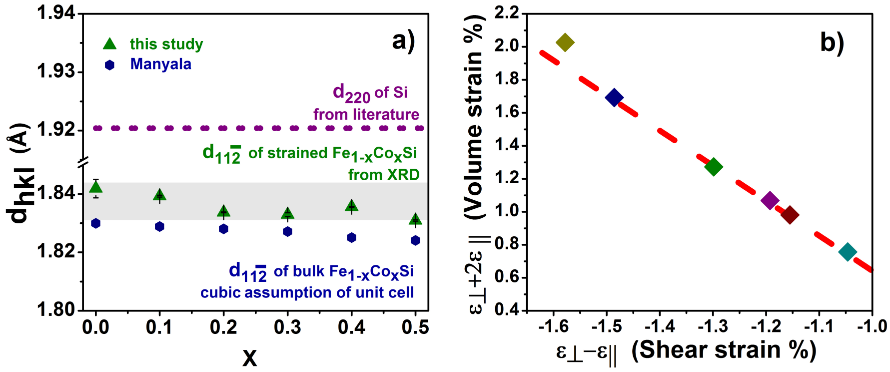

Figure 4.19: Epitaxial strain analysis. (a) Comparison of evolution of inter-planar spacing $d_{11\bar{2}}$ of epitaxial $Fe_{1-x}Co_xSi$ films as a function of cobalt content x from data obtained by XRD, with that of a bulk $Fe_{1-x}Co_xSi$ crystal (from Manyala *et al.*) and silicon d_{220}. The shaded region shows the spread of data points obtained in this study. (b) Variation of volume strain with shear strain for various levels of Co doping in $Fe_{1-x}Co_xSi$ films (represented by different coloured data points). The dashed line is a straight line best fit to the data.

and that there are no structural phase changes associated with the strain. Thus, even though the strained $Fe_{1-x}Co_xSi$ films have a rhombohedral unit cell, they are phase pure, consistent with the XRD data (Fig. 4.16(a)) and HRTEM images (Fig. 4.17(a) and (b)).

Knowledge of the in-plane and out-of-plane lattice constants give a full determination of the geometry of the rhombohedral unit cell. The volume of the unit cell as function of x is plotted in Fig. 4.18(e). The unit cell volume decreases in a non-linear fashion with x, and always exceeds that for a bulk crystal. We have also calculated the variation of the rhombohedral angle as a function the varying Co doping, shown in Fig. 4.18(f), which is always slightly more than 90°.

4.8 Thickness varying $Fe_{0.8}Co_{0.2}Si$ thin films

On the lines of investigating the variation of Co doping in $Fe_{1-x}Co_xSi$ epitaxial system, we investigated the thickness dependence of $Fe_{1-x}Co_xSi$ epilayers too. $Fe_{1-x}Co_xSi$ epilayers with $x = 0.2$ of varying thickness, 2.5 nm, 5 nm, 7.5 nm, 10 nm, 20 nm, 50 nm were grown using the same protocol as mentioned earlier in the chapter. X-ray diffraction was used to structurally characterise the films using Bragg's law. Both in-plane [002] and out of plane [111] Bragg peaks were identified using $\theta - 2\theta$ scans and

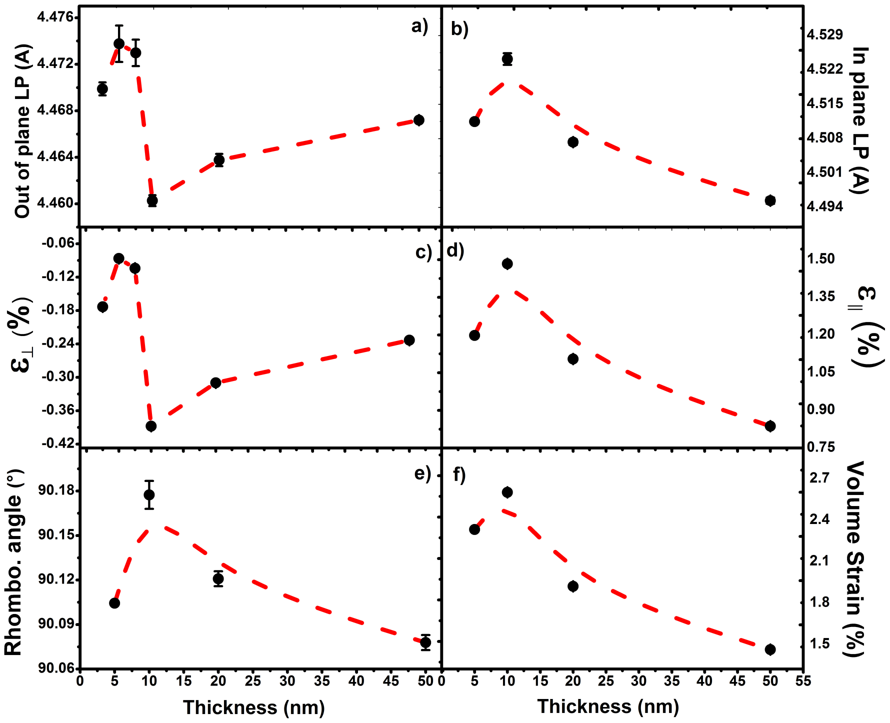

Figure 4.20: Strain analysis. (a) Out-of-plane lattice parameter a_{111} of $Fe_{0.8}Co_{0.2}Si$ films based on data from XRD. (b) In-plane lattice parameter $a_{11\bar{2}}$, based on data from XRD. (c) Out-of-plane of strain determined from data in (a). (d) In-plane strain determined from data in (b).(e) Rhombohedral angle as a function of thickness. (f) Rhombohedral unit cell volume as a function of x. The dashed lines are guides to the eye.

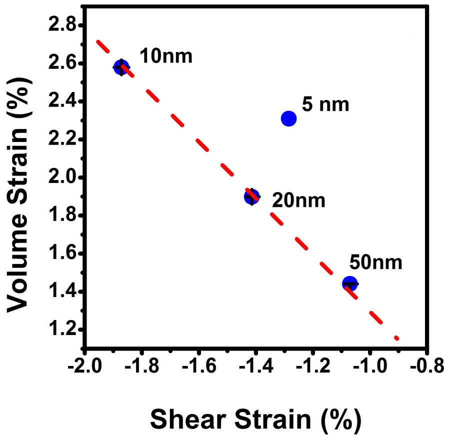

Figure 4.21: Epitaxial strain analysis, variation of volume strain with shear strain for various thicknessess of $Fe_{0.8}Co_{0.2}$ films. The dashed line is a straight line best fit to the data.

the analysis is shown in figures 4.20 and 4.21. The out of plane Lattice parameter (LP) increases with increasing thickness upto 4.474 $\AA$ for 5 nm and then decreases slowly upto 7 nm before dropping down drastically to 4.460 $\AA$ at 10 nm thickness. It slowly increases further upto 4.466 $\AA$ for a 50 nm thick film (see fig.4.20 a). Similar behaviour is observed for out of plane strain too (see fig.4.20 c). Due to biaxial strain in the films the unit cell is no longer cubic but rhombohedral. The variation in rhombohedral angle as a function of varying film thickness is shown in Fig. 4.20 e), it is slightly more than 90° for all films with varying thickness. Overall, the film is compressively strained in out of plane direction and tensile strained in in-plane direction with maximum magnitude of strain at 10nm thickness for both the orientations. In plane LP, inplane strain, volume strain, and unit cell angle angle follow similar pattern. The values increase upto 10 nm thickness and then decreases down to 50 nm thick film. It is important to note that 10 nm seems to be the critical thickness for an $Fe_{1-x}Co_xSi$ thin film with $x = 0.2$ doping. The structural behaviour of the film and hence that of the unit cell is very different before and after the film critical thickness of 10 nm is reached. Figure 4.21 shows a linear relationship between volume strain, shear strain for films thickness 10 nm and above indicating that there is no phase change. The preliminary results have been presented in this section. The results look promising and would pave way for further investigations.

Overall, $Fe_{1-x}Co_xSi$ thin films of varying Co doping as well as varying thickness (for Co= 0.2) were successfully grown by MBE on Si (111) substrate. The films were structurally characterised by LEED, RHEED, XRD, and TEM. The qualitative and quantitative analysis as presented in the chapter shows that the films are epitaxial, phase pure, and are of high quality. The lattice mismatch between the substrate and the epitaxial film gives rise to a biaxial strain which in turn distorts the cubic structure of the unit cell (in bulk system) to a rhombohedral in the epitaxial form. These changes in unit cell geometry induced by epitaxial strain can be expected to give rise to modifications to various properties such as the band structure, density of states, transport properties, magnetization and magnetic anisotropy, which we will explore in remainder of the chapters.

CHAPTER 5

Transport Properties

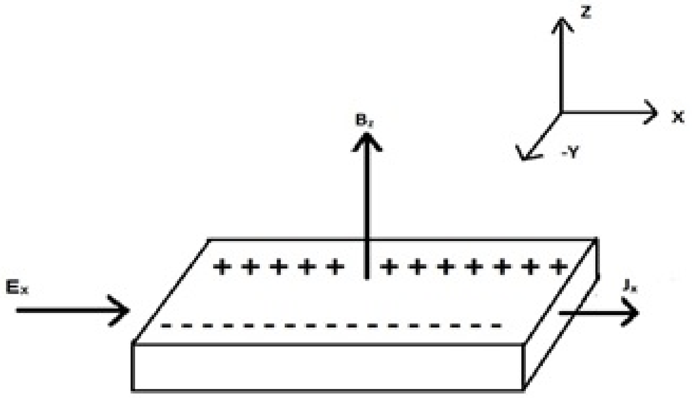

Figure 5.1: Hall effect- A current carrying conductor with applied magnetic and electric fields

Various transport properties of Fe$_{1-x}$Co$_x$Si epilayers were measured using devices made out of lithographically patterned films. Ordinary Hall effect, anomalous Hall effect and topological Hall effect were measured. Below, is a brief description of Hall effect in a current carrying wire after results are presented.

5.1 Hall Effect

We consider the Hall effect for a current carrying wire. An electric field E_X is applied along x direction (longitudinal), causing a current density j_x to flow in the wire. When a magnetic field B_z is applied along the z direction (transverse), the electrons are deflected to the sides of the wire, in a direction perpendicular to both the applied electric and magnetic field due to the Lorentz force F_L acting on the charge carriers.

$$F_L = q(E + v \times B) \tag{5.1}$$

The deflection of charges causes an additional voltage to build up along the sides of the wire which is called Hall voltage. The resulting Hall field E_Y is in the negative y direction. The Hall coefficient R_H is given by the equation 5.2

$$R_H = \frac{E_Y}{j_X B} \tag{5.2}$$

Where j_x is the current density given by the equation 5.3, n is number of charge carriers, e is charge, τ is the mean free time between two successive collisions and m is the mass of the charge carriers.

$$j_x = ne^2\tau\frac{E_x}{m} \tag{5.3}$$

Assuming that no current flows out in the y direction, E_Y is given by equation 5.2 below, where ω_C is the cyclotron frequency of an electron under the influence of magnetic field.

$$E_Y = -\omega_C\tau E_X = \frac{-eB\tau}{m}E_X \tag{5.4}$$

On substituting value of j_X and E_Y in equation 5.5 below we obtain R_H in terms of number of charge carriers per unit volume.

$$R_H = \frac{-1}{ne} \tag{5.5}$$

If Hall resistivity (ρ_H) is plotted against the applied magnetic field ($\mu_o H$), it is observed that in the weak field limit the resistivity increases sharply with increasing $\mu_o H$ and might be linear in nature. However, at higher fields the magnetisation (M) is saturated, the Hall resistivity is linear and has relatively smaller slope. The Hall resistivity therefore can be written as equation 5.6 below :

$$\rho_H = R_o H + 4\pi R_s M \tag{5.6}$$

It is sum of contribution from both the ordinary Hall effect (term on the right) and anomalous Hall effect (second term on the right). R_o is the ordinary hall coefficient which arises due to the Lorentz force and depends only on the carrier density. R_s is the anomalous Hall coefficient which arises due to the intrinsic property of the material. So even when there is no applied magnetic field the the extra ordinary Hall effect is present and is a spontaneous contribution, since, in a ferromagnet there is spontaneous magnetisation. In a ferromagnet, R_s should be zero at absolute zero in a perfect lattice and it increases as the temperature increases until the Curie temperature is reached.

Magnetoresistance: An ideal free electron gas will have no magnetoresistance when the Lorentz force balances the induced electric field E_Y. However in non ideal metals the conduction electrons have a velocity distribution and the mean velocities are different. Though Hall electric field balances the magnetic field, the individual electrons move in curled orbits or paths due to the Lorentz force. They travel further, scatter more and hence the resistance increases due to the presence of the magnetic field as compared to the resistance in absence of the field. This gives rise to the positive magnetoresistance in metals. Magnetoresistance can be expressed by the equation 5.7 below as the difference in the resistivity of the metal in presence and absence of magnetic field. This MR arises due to the Lorentz force.

$$MR = \frac{\rho(B) - \rho(0)}{\rho(0)} \tag{5.7}$$

Anomalous Hall Effect: Another phenomenon observed in case of metals and ferromagnets is the Anomalous Hall Effect (AHE) or Extraordinary Hall Effect (EHE) along with the Ordinary Hall Effect (OHE) explained above. The anomalous Hall effect is due to the large localised magnetic moment in the material. It varies as a function of temperature. The origin of AHE is debatable but three main contribution or mechanisms are widely accepted, they are as described below.

$$\rho_{AHE} = \rho_{intr} + \rho_{skew} + \rho_{side\ jump} \tag{5.8}$$

Intrinsic contribution (ρ_{intr}): Karplus and Luttinger [86] proposed that when an electric field is applied, the electrons (Bloch wave) in the solid gain an additional contribution to the group velocity that is perpendicular to the electric field and therefore contributes to the net Hall effect. Therefore $\rho_{intr} \propto \rho_{xx}^2$, where ρ_{xx} is the longitudinal resistivity. The additional velocity when summed over all the occupied bands in a ferromagnet gives a non zero term. The additional contribution depends on the band structure, is independent of scattering, is a consequence of spin orbit coupling, and therefore is an intrinsic property of the material system being probed. In recent theories, the intrinsic contribution is interpreted in terms of change in Bloch wave states in momentum space or in real space Berry phase [87].

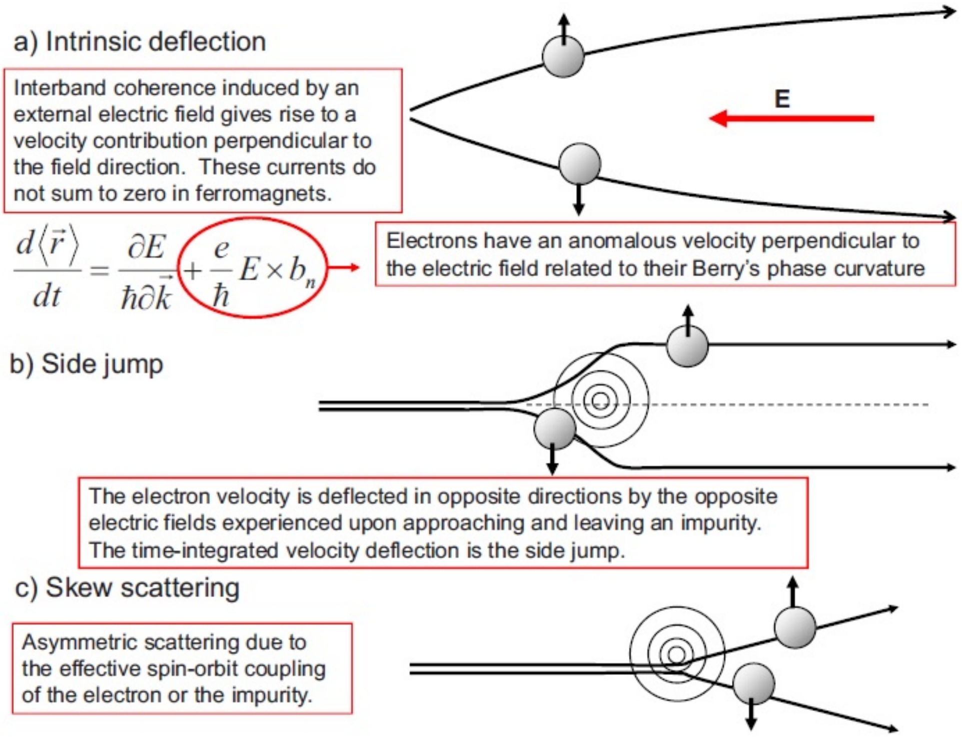

Figure 5.2: Illustration of the three main mechanisms that can give rise to an AHE. In any real material all of these mechanisms act to influence electron motion [88].

Extrinsic contribution ($\rho_{skew} + \rho_{sidejump}$): The spin orbit coupling (SOC) not only modifies the impurity scattering but also contributes to the extrinsic mechanism. Extrinsic contribution can further be divided into skew scattering (ρ_{skew}) and side jump ($\rho_{sidejump}$) mechanisms. Skew scattering is an asymmetric scattering arising due to SOC of the impurity or electron and can be expressed as $\rho_{skew} \propto \rho_{xx}$ [89]. In a side jump, an electron approaches an impurity and is deflected in opposite directions by opposite electric fields. The time integrated velocity deflection of an electron is the side jump and can be expressed as $\rho_{sidejump} \propto \rho_{xx}^2$ [90].

Topological Hall Effect(THE): Unlike AHE that arises due to nontrivial topology in momentum space, THE arises due to nontrivial topology in real space [91]. When an electron moves through a two-dimensional electron gas and encounters a chiral texture that has a spatially varying magnetic field, the electron acquires a Berry phase. The Berry phase depends on the solid angle that is subtended by the local magnetisation of the chiral structure as the electron follows its path. Whithin the adiabatic limit, the electron moving through a skyrmion aligns its spin with the spatial magnetisation which generates a gauge field of one quantum of flux per single skyrmion [92]. As a result the electron experiences the emergent gauge field during the transport [93]. The emergent gauge field generates a Hall voltage that is perpendicular to the sample plane and unlike the AHE it doesn't directly originate from SOC, although SOC is needed for DMI that for instance gives skyrmions. This voltage that contributes to the net Hall effect is termed as THE. Helimagnets that have skyrmion lattice or that have topologically trivial chiral spin texture show THE. Hall signal thus measured for these B20 material system have a THE component and therefore, is a signature of skyrmion or chiral phase in the system [94] [32][24][95][30].

5.2 Result I -Transport Properties

The transport properties of our $\mathrm{Fe}_{1-x}\mathrm{Co}_x\mathrm{Si}$ films were measured in a gas-flow cryostat with a base temperature of 1.4 K capable of applying magnetic fields of up to 8 T. The films were patterned into Hall bars that were 5 μm wide using optical lithography, etched by Ar ion milling, and bonded onto a chip carrier for measurement.

Measurements of the electrical resistivity $\rho(T, H)$ of the films as a function of temperature T and magnetic field H applied perpendicular to the sample plane are shown in Fig. 5.3. A bias current of 30 μA was used. The solid lines show the $\rho(T)$ in the absence of a magnetic field and the dashed lines show $\rho(T)$ in presence of an 8 T magnetic field. Fig. 5.3(a) shows the resistivity variation of an FeSi film. FeSi is a narrow band-gap semiconductor,[5] and upon decreasing the temperature the resistivity increases reaching 3700 $\mu\Omega$cm at 1.4 K. We determined the band-gap of the epitaxial FeSi to be $\Delta = 30.1 \pm 0.2$ meV using the following relation:

$$\ln \rho \propto \left(\frac{\Delta}{2kT}\right), \tag{5.9}$$

where k_B is the Boltzmann constant, fitted to the high temperature data (above 50 K).

Doping FeSi with Co introduces electron-like carriers and a lowered resistivity. At the opposite extreme, the $\rho(T)$ relation for the film with $x = 0.5$ has a metallic form, shown in Fig. 5.3(f), increasing with T for all temperatures. Intermediate values of

x yield hybrid $\rho(T, 0)$ dependences, with a gradual crossover from semiconductor-like to metal-like behavior as x rises (shown in Fig. 5.3(b)-(e)). For these values of x the $\rho(T, 0)$ curve is often non-monotonic, combining regions with both positive and negative temperature coefficients of resistance. The curves are similar to those measured for bulk crystals at a qualitative level,[3; 13], but differ quantitatively.

In the intermediate doping regime ($0 < x < 0.5$), we observe some distinctive features such as points of local maximum (T_{max}) and minimum (T_{res}) in the resistivity that vary with the degree of Co doping. For instance, in Fig. 5.3 (for $x = 0.15$) we observe a broad maximum in ρ around 125 K. As the Co doping increases this maximum shifts towards higher temperatures, reaching 175 K for $x = 0.3$, then becoming less pronounced until it vanishes for $x = 0.5$. The observed broad maximum is a feature reminiscent of the narrow band-gap semiconducting parent compound FeSi [13]. The maxima and associated temperature shift can be explained in the framework of epitaxial strain and Co doping. Substituting Co for Fe not only introduces volume strain (as previously shown in Fig. 4.19(b)), but also changes the band structure, resulting in a broadening of bands and reduced band gap.[96] Thus, increased Co doping provides more carriers to be available for conduction, giving rise to the hybrid semiconducting-metallic behaviour that we see. It is the competition between the temperature dependence of mobility, importance of thermally activated carriers (particularly at low x) and the carrier concentration that gives rise to such difference in $\rho(x, T)$. $\mathrm{Fe}_{1-x}\mathrm{Co}_x\mathrm{Si}$ films thus lose the low T insulating behaviour of FeSi as x rises.

As the temperature decreases further below T_{max}, the resistivity decreases until a minimum (T_{res}) is reached. This minimum in the resistivity curve is related to the magnetic behaviour of the films and signifies the onset of magnetic ordering in the $\mathrm{Fe}_{1-x}\mathrm{Co}_x\mathrm{Si}$ crystal structure.[96] The position of the minimum T_{res} varies with Co doping and is found to follow the same trend as the magnetic ordering temperature T_{ord}, as we shall discuss later in chapter on magnetic characterisation. Ideally, $T_{\mathrm{res}} \approx T_{\mathrm{ord}}$, but in the samples studied here, we find that T_{res} is actually slightly higher. The value of T_{res} increases with increasing Co doping and reaches the maximum value of ~ 92 K for $x = 0.4$ before decreasing again. The transport properties of $\mathrm{Fe}_{1-x}\mathrm{Co}_x\mathrm{Si}$ epilayers are dominated by short-ranged ferromagnetic interactions in the crystal structure.[13] When the mean free path is of the same order as the ferromagnetic correlation length, T_{ord} and T_{res} almost coincide, as is the case for $x = 0.1$ and 0.5. However, if the mean

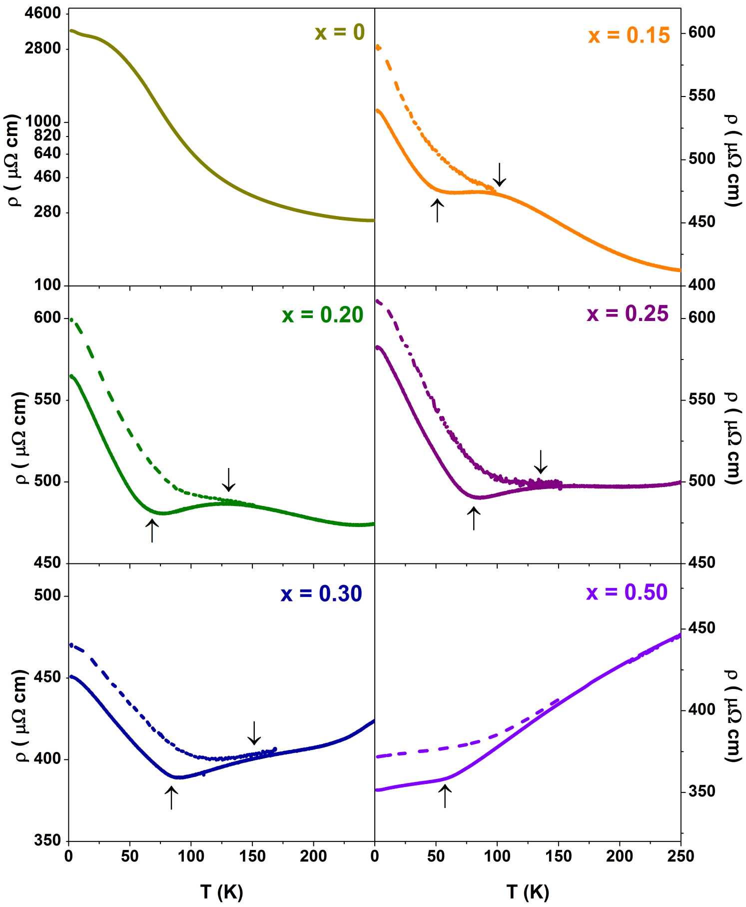

Figure 5.3: Temperature dependence of resistivity in ∼ 50 nm films of $Fe_{1-x}Co_xSi$ in magnetic fields of 0 T (solid lines) and 8 T (out of plane field, dashed lines). Increasing cobalt concentration x changes the temperature coefficient of resistivity from negative (semiconductor-like) for $x = 0$ to positive (metallic-like) for $x = 0.5$, with mixed behavior seen for intermediate values of x. The arrows ↑ and ↓ illustrate temperatures at which there is a minimum, T_{res}, and maximum, T_{max}, in the resistivity, respectively.

free path is longer, then T_{res} is higher than T_{ord}, as we observe for $\text{Fe}_{1-x}\text{Co}_x\text{Si}$ films in the range $0 < x < 0.5$ (and discuss later in chapter on magnetic characterisation). Also this may be due to magnetic fluctuations occurring above the ordering temperature which may contribute to the discrepancy between the magnetic ordering temperature and T_{res}.[10] When the temperature is decreased below T_{res}, the resistivity further increases for the $\text{Fe}_{1-x}\text{Co}_x\text{Si}$ films with $0 < x < 0.5$, as has been pointed out in previous studies.[3; 16]

Overall we observe semiconducting behaviour of the films for low x and metallic for high x. This remains the case when the measurements were performed under a $\mu_0 H = 8$ T field applied perpendicular to the sample plane (dashed lines in Fig.5.3). In the high temperature region (above $\sim T_{\text{max}}$), the resistivity is almost unchanged with field for all our $\text{Fe}_{1-x}\text{Co}_x\text{Si}$ films. In the lower temperature regime, after the onset of magnetic ordering, the magnetoresistance (MR) gradually rises in the semiconducting regime, washing out any maximum in $\rho(T)$. Positive MR is a very typical property of the $\text{Fe}_{1-x}\text{Co}_x\text{Si}$ system, and shall be discussed in more detail in the next section.

5.3 Result II -Magnetoresistance

Unlike most other ferromagnetic metals, which show negative MR at high fields,[97] $\text{Fe}_{1-x}\text{Co}_x\text{Si}$ systems show unusual positive MR in the form of bulk crystals and epilayers.[3; 13; 14] The high field MR in these $\text{Fe}_{1-x}\text{Co}_x\text{Si}$ samples, shown in Fig. 5.3 for a perpendicular field orientation, is not only linear for $x > 0$, but also isotropic for $T < T_{\text{res}}$. For an FeSi film, the MR has a quadratic dependence on magnetic field. Introducing Co doping to FeSi, changes the nature of the curve from quadratic to linear at $x = 0.1$, with a large MR ratio $\Delta\rho/\rho$ of almost 12% in an 8 T field at 5 K.

Fig. 5.4(a) shows the MR ratio observed in $\text{Fe}_{1-x}\text{Co}_x\text{Si}$ epilayers for different Co doping for a field of 8 T at 5 K. As the Co content is increased from $x = 0.1$ to $x = 0.5$, we observe that the MR remains linear at low temperatures ($T < T_{\text{res}}$), i.e. in the presence of magnetic ordering. As the temperature is increased the linearity of the MR is lost, and above T_{max} it becomes quadratic for all our $\text{Fe}_{1-x}\text{Co}_x\text{Si}$ films. The maximum MR should be observed near the metal-insulator transition, where there is the highest Coulomb interaction. This is observed here for $x = 0.1$, as shown in Fig. 5.4(b) where we observe an MR ratio of almost 12%. The MR ratio decreases with increasing Co content up to $x = 0.3$, and then flattens off at a level of $\sim 5\%$ for all

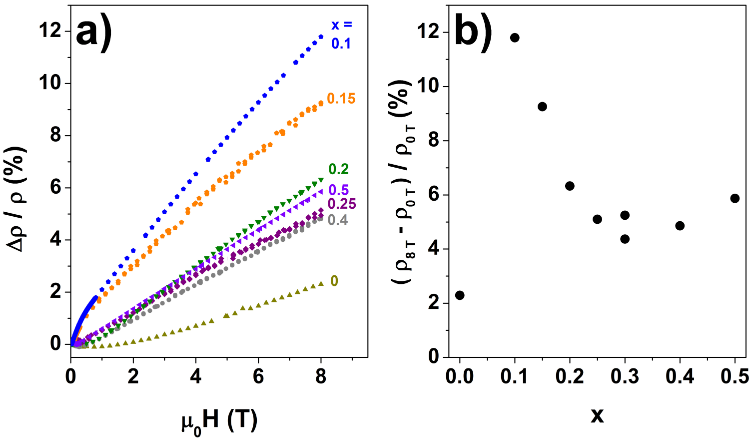

Figure 5.4: Magnetoresistance in an out-of-plane field. (a) MR isotherms at 5 K for $Fe_{1-x}Co_xSi$ films of varying Co doping x. (b) MR ratio at 8 T and 5 K as a function of cobalt concentration x.

higher values of x. The explanation of this low T positive linear MR is contested: both quantum interference effects,[3] and Zeeman splitting of the majority and minority spin bands, which reduces the high mobility minority spin carriers and in turn increases the resistivity,[13] have been cited as causes.

5.4 Result III -Hall Effect

Hall measurements were made simultaneously with the longitudinal resistivity measurements. As an example, the Hall resistivity $\rho_{xy}(H)$ for an $Fe_{1-x}Co_xSi$ thin film with $x = 0.4$ is shown in Fig. 5.5(a) for various temperatures. There is low field hysteresis (for fields $\mu_0 H \leq 0.3$ T) and a high field linear regime. (Inset in Fig.5.5(a) are data measured at 5 K showing the high field response.) The high field slope is due to the ordinary Hall effect. This high field Hall slope, measured at 5 K for $Fe_{1-x}Co_xSi$ films with different values of x, was used to determine the type of charge carrier and carrier density, as shown in Fig. 5.5(b), and was combined with the longitudinal resistivity to give the mobility of the carriers in the film, as shown in Fig.5.5(c). In the bulk, each Co dopant contributes one conduction electron to the electron gas over the whole x range.[3] The data shown in Fig.5.5(b) show that there is a small shortfall in our samples, with close to, but not quite, one electron-like carrier per Co dopant. It is possible that there are defects in our film, too subtle to pick up by XRD or HRTEM,

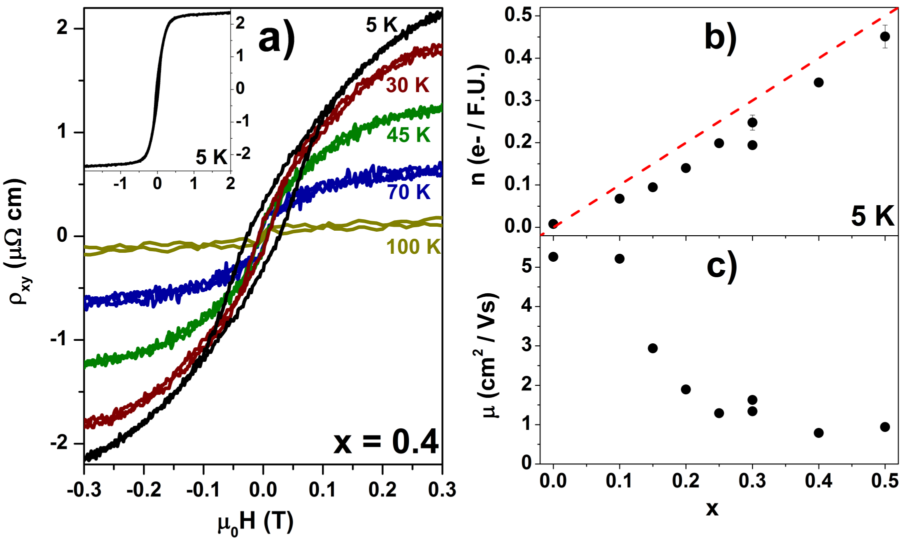

Figure 5.5: Hall measurements. (a) Hall resistivity ρ_{xy} as a function of field for Fe$_{1-x}$Co$_x$Si epilayers with $x = 0.4$ for selected temperatures. Hysteresis is observed in the extraordinary Hall effect which diminishes at elevated temperatures. The ordinary Hall effect was extracted at high fields above the saturation field. A hysteresis loop (M-H) at 5 K is shown inset up to higher magnetic fields. (b) Charge carrier density expressed as electrons per formula unit inferred from measurements of the high field ordinary Hall effect at 5 K. The dashed line illustrates the ideal case of one electron added to the electron gas per cobalt atom. (c) Carrier mobility μ as a function of cobalt doping x at 5 K.

that act as traps preventing all the electrons released by the Co dopants from acting as carriers. As shown in Fig.5.5(c), the mobility μ of the charge carriers drops with increasing Co doping in the films, which can be accounted for if the Co dopants act as scattering centres.

The hysteretic part of the the Hall signal arises due to the anomalous Hall effect that is present in magnetically ordered materials.[98] The Hall resistivity in a ferromagnetic material is given by

$$\rho_{xy} = R_{\mathrm{o}}H + 4\pi R_{\mathrm{s}}M, \tag{5.10}$$

where R_{o} is the ordinary Hall coefficient and R_{s} is the anomalous Hall coefficient. The anomalous contribution to the Hall resistivity $\rho_{\mathrm{AH}} = R_{\mathrm{s}}\mu_0 M$ was determined by extrapolating the high field Hall slope, where the magnetization M is saturated, so any topological contribution of the Hall resistivity[23; 24] is neglected in the present analysis. ρ_{AH} for the $x = 0.4$ sample, shown in Fig.5.5(a), is as large as 2 $\mu\Omega$cm at 5 K,

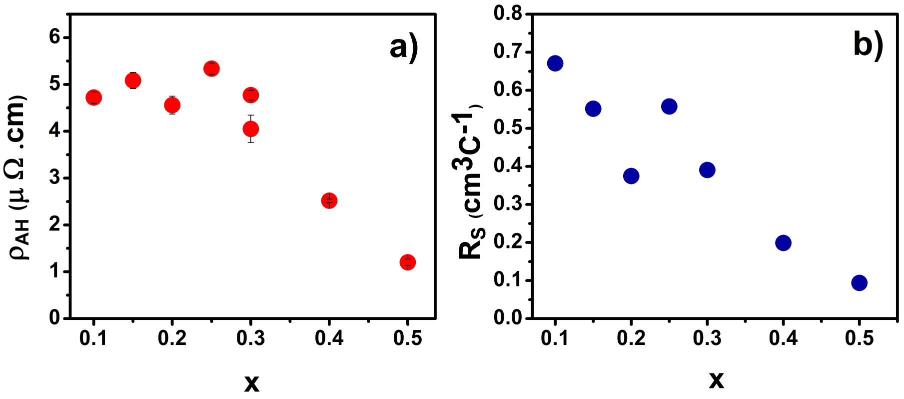

Figure 5.6: Anomalous Hall effect. (a) Variation of anomalous Hall resistivity ρ_{AH}, and (b) anomalous Hall coefficient R_{s} as a function of x at 5 K for $\mathrm{Fe}_{1-x}\mathrm{Co}_x\mathrm{Si}$ films.

and diminishes as T rises, becoming almost negligible at 100 K or beyond. As shown in Fig.5.6(a), even larger values of ρ_{AH} can be found for lower values of x. $\mathrm{Fe}_{1-x}\mathrm{Co}_x\mathrm{Si}$ layers with $x \lesssim 0.3$ have $\rho_{\mathrm{AH}} \sim 5\mu\Omega$cm. The highest value we observe is 5.5 $\mu\Omega$ cm for $x = 0.25$. In Fig. 5.6(b) we plot anomalous Hall coefficient R_{s} as a function of x and observe that highest value is reached for $x = 0.1$, up to 0.67 ± 0.04 cm^{3}C^{-1} before decreasing almost linearly to 0.09 ± 0.01 cm ^{3}C^{-1} for $x = 0.5$. The large value of R_{s} observed in our epilayers is of similar order, but a little higher than, that observed in bulk $\mathrm{Fe}_{1-x}\mathrm{Co}_x\mathrm{Si}$ crystals by Manyala *et al.*[37] This may be attributed to the strained epitaxial structure of $\mathrm{Fe}_{1-x}\mathrm{Co}_x\mathrm{Si}$ films, in which strain increases the effective spin-orbit coupling.

5.5 Result IV -Topological Hall Effect (THE)

Signature of Skyrmions or topologically protected magnetic vortex like structures in B20 material have previously been investigated by measurement of Topological Hall Effect. Yokouchi *et al* [32] and Kanazawa *et al* [99] have come up with an unique way of treating these skyrmionic structures in MnFeSi and FeGe system. They postulate that when applied magnetic field (external) is inclined at an angle from the normal to the film surface, the skyrmions stretching along the field direction have an out of plane modulation which destabilises the magnetic system. Increasing the inclination angle suppresses the skyrmion formation completely and therefore reduces the THE arising due to skyrmions. The same has been illustrated in figure 5.7 (a)-(d) by Kanazawa *et* *al.*[99]. Measuring the Hall resistance or Hall resistivity through a range of angles would give us an understanding about the formation and annihilation of skyrmion in the B20 system.Presence of skyrmions or similar chiral structure in epitaxial $\mathrm{Fe}_{1-x}\mathrm{Co}_x\mathrm{Si}$ thin film has been investigated by Porter *et al*[100] using Polarised Neutron Reflectometry (PNR) and THE. We try to reconfirm the presence of skyrmions and understand the dynamics of formation in $\mathrm{Fe}_{1-x}\mathrm{Co}_x\mathrm{Si}$ thin films by measuring the angular dependence of THE following the protocol mentioned above.

The devices that were used for measurements of the Hall Effect were used for these angle dependent measurements as well. The sample holder had a stepper motor that could tilt the device such that the normal to the film made an angle of inclination (θ) with the applied magnetic field (see inset of fig.5.8). A series of devices patterned out of $\mathrm{Fe}_{1-x}\mathrm{Co}_x\mathrm{Si}$ epilayers with varying x were measured at 5 K with applied magnetic field values extending up to 3 T. The results for $\mathrm{Fe}_{1-x}\mathrm{Co}_x\mathrm{Si}$ ($x = 0.3$) is shown in the figures 5.8 and 5.9 measured at angles of $\theta = 0°$,2°,4°,6°,8°,20°, and 30°$(see fig.$5.9$)$.

In figure 5.7 (a)-(d), Kanazawa *et al.*[99] show the variation of the angular dependence of normal Hall resistivity (ρ^N_{yx}) and anomalous Hall resistivity (ρ^A_{yx}) as a function of $\mu_o H$ Cosθ instead of $\mu_o H$. By doing so they align the angle dependent curves such that at low magnetic fields they lie on the *universal curve* as shown in the figure. Topological Hall resistivity is present only at low fields and is eliminated at higher fields. It (topological Hall resistivity) is then extracted as a difference ($\Delta\rho_{xy}$) of the Hall resistivity measured at $\theta = 0^o$ and 30^o. The difference gets rid of the normal and anomalous Hall components and is representative of the topological Hall resistivity arising due to skyrmions. 30^o is the critical angle above which no topological hall component is observed by Yokouchi *et al.*[32] in $B20$ systems [32]. However an anomalous Hall component is still observed in their data and to remove it they scale the difference ($\Delta\rho_{xy}$) by multiplying it by the scaling factor:

$$\frac{cos0^o - cos30^o}{cos\theta^o - cos30^o} \tag{5.11}$$

We followed the protocol described above to analyse the variation of Hall resistance with varying angle of inclination. The difference in the Hall resistance ΔR_{xy} is described by the equation below when plotted against $\mu_o H$ Cosθ:

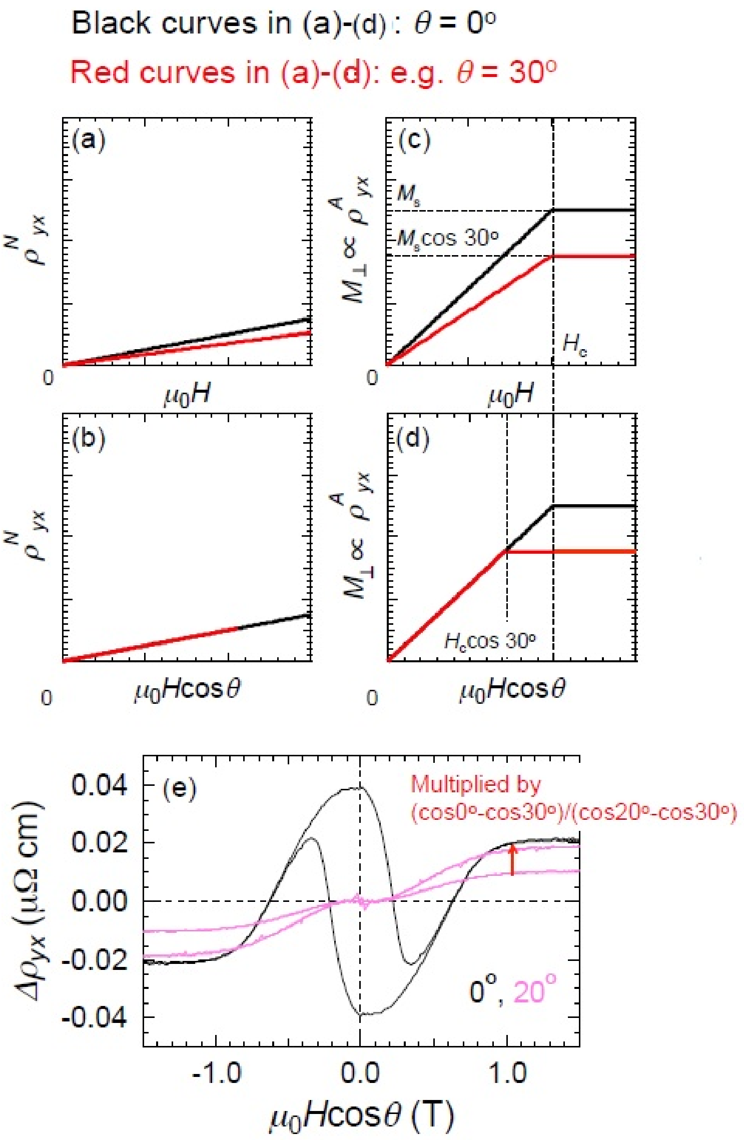

Figure 5.7: In the graphs above, (a)-(d) are conceptual graphs used by the author to show the comparison between ΔR_{xy} and M measured at 30^o (red) with respect to the one measured at 0^o (black) when plotted against $\mu_o H$ and $\mu_o H$ Cosθ respectively. The black curve is referred to as the universal curve in the main text. Graph (e) shows the comparison between the scaled and the unscaled ΔR_{xy} for Hall resistances measured at 20^o and 0^o [99].

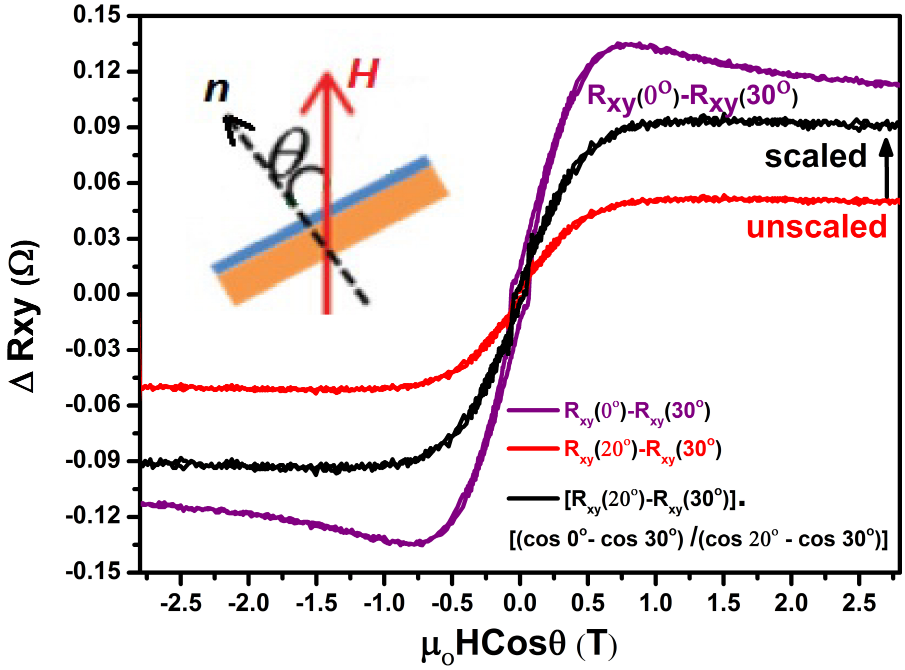

Figure 5.8: The figure shows comparison between the scaled (black) and the unscaled (red) ΔR_{xy} measured at 20^o (red, black)with respect to the one measured at 30^o (purple), when plotted against $\mu_o H$ Cosθ. The inset illustrates the angle θ between the surface normal of the film and the applied magnetic field.

$$\Delta R_{xy}(unscaled) = R_{xy}(\theta^o) - R_{xy}(30^o) \tag{5.12}$$

where θ is the angle of inclination between the sample normal and the applied magnetic field. To get rid of the anomalous Hall component we use the scaling factor described by the equation below:

$$\Delta R_{xy}(scaled) = [R_{xy}(\theta^o) - R_{xy}(30^o)] \cdot \frac{cos0^o - cos30^o}{cos\theta^o - cos30^o} \tag{5.13}$$

The results are shown in figure 5.8 and 5.9 for a device made from Fe$_{1-x}$Co$_x$Si ($x = 0.3$) epilayer. Figure 5.8 shows the comparison between the scaled and the unscaled ΔR_{xy} for Hall resistances measured at 20^o with respect to the one measured at 30^o, after they have been subtracted from R_{xy} measured at 0^o inclination. As skyrmions cease to exist beyond the critical angle[32], the low angle data represents all the Hall components viz. normal, anomalous and topological where as the high angle data contains only the

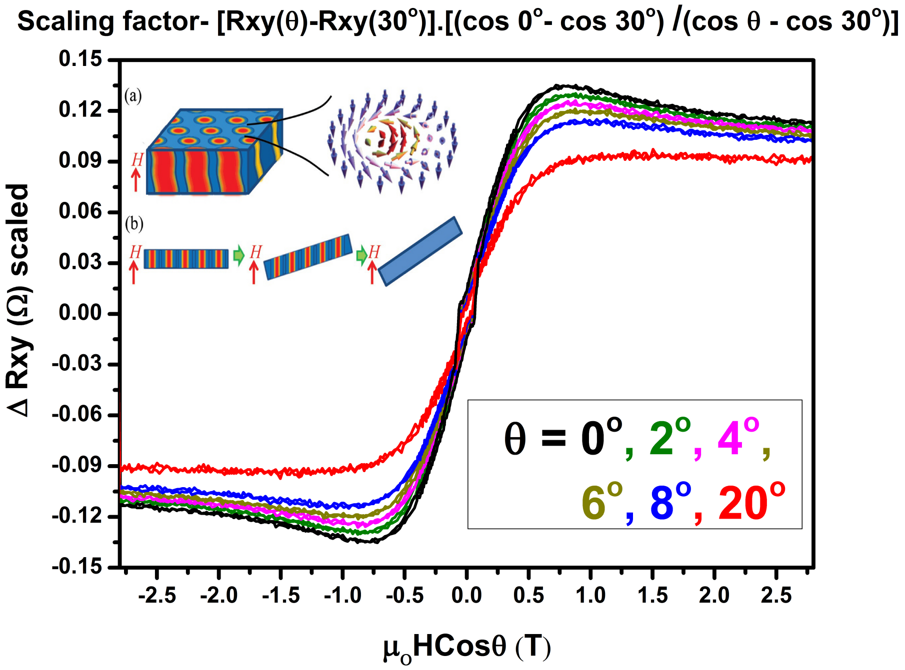

Figure 5.9: The figure shows comparison between scaled ΔR_{xy} at various angles (shown above) plotted against $\mu_o H$ Cosθ. Figure in the inset shows the creation and destruction of skyrmions as the sample plane is tilted with respect to the applied magnetic field.

normal and anomalous Hall components. Subtracting high angle data from low angle data, normal and anomalous Hall component are eliminated at low fields. Therefore as per the protocol, $\Delta R_{xy}(0^o) - \Delta R_{xy}(30^o)$ and $\Delta R_{xy}(0^o) - \Delta R_{xy}(20^o)$ should represent only the topological Hall component at low field. We, however, observe in Fig. 5.8 that at higher fields (upto 3T), even after scaling to get rid of any anomalous Hall component, $\Delta R_{xy}(0^o) - \Delta R_{xy}(20^o)$ doesn't quite scale up to $\Delta R_{xy}(0^o) - \Delta R_{xy}(30^o)$.

This indicates that THE extends up to higher fields but it is highly unlikely if M is saturated or the skyrmions are not fully suppressed. Hysteresis in the B20 system has been attributed to skyrmions [99]. Figure 5.9 shows the angle dependent Hall resistance that were scaled scaled using equation 5.13. We observe that at low fields the hysteresis that has been attributed to Topological Hall effect decreases with increasing angle of inclination. In FeGe system Kanazawa *et al.* [99] showed that the hysteresis completely vanishes at higher angles 5.11 indicating the absence of THE and hence the skyrmions. But unlike FeGe system , the hysteresis does not completely vanish at 20^o. Also, resistance ΔR_{xy} for different angles does not converge at higher field values even after

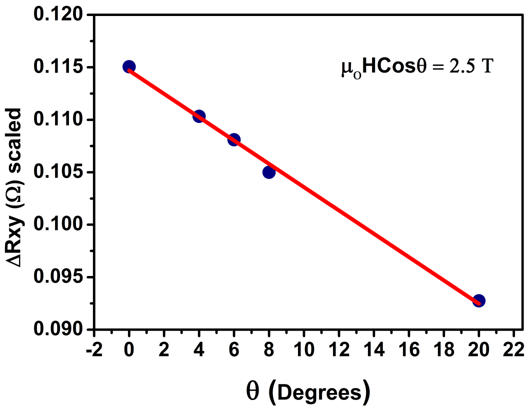

Figure 5.10: The figure shows variation of scaled ΔR_{xy} as a function of varying angle of inclination at 2.5 T. The red line is a linear fit.

scaling up. In fig. 5.10, we can see the variation of ΔR_{xy} as a function of θ measured at 2.5 T. As the angle of inclination increases the magnitude of ΔR_{xy} decreases following a linear trend and drops down significantly for $\theta = 20^o$. But nevertheless, ΔR_{xy} doesn't go down to zero for $\theta = 20^o$. Using $y = mx + c$, we see that if we go up to 90^o, ΔR_{xy} may go down to zero, 90^o in which case would be the critical angle. To understand the skyrmion formation and annihilation mechanism better we compare the graphs from our experiments(fig. 5.9) with that obtained by Kanazawa *et al.* (5.11). We see that the nature of graphs are very different from each other, especially the hysteresis loop close to 0 T. To remove any other leftover component of AHE we used linear fitting to fit the data experimentally obtained by us and subtract the slope from the loops. That resulted in fig. 5.12. Upon comparing fig 5.11 with fig 5.12 we can clearly see that the nature of the hysteresis is completely different. In case of fig 5.12 obtained by Kanazawa *et al.* for FeGe system the hysteresis peaks at around 0 T. However, for fig 5.12 for $\mathrm{Fe}_{1-x}\mathrm{Co}_x\mathrm{Si}$ system the the hysteresis peaks at around ±0.08 T. Also the unlike FeGe system the hysteresis does not quite converge to zero in $\mathrm{Fe}_{1-x}\mathrm{Co}_x\mathrm{Si}$ system.

The observations above suggest that there are various parameters that control the skyrmion or chiral structure formation in B20 system. The experiment based on changing the inclination angle between the surface normal of the sample and the external applied field needs to be backed up by micro-magnetic simulation or some other form of theoretical calculations to support the experimental evidence. The critical angle 30^o

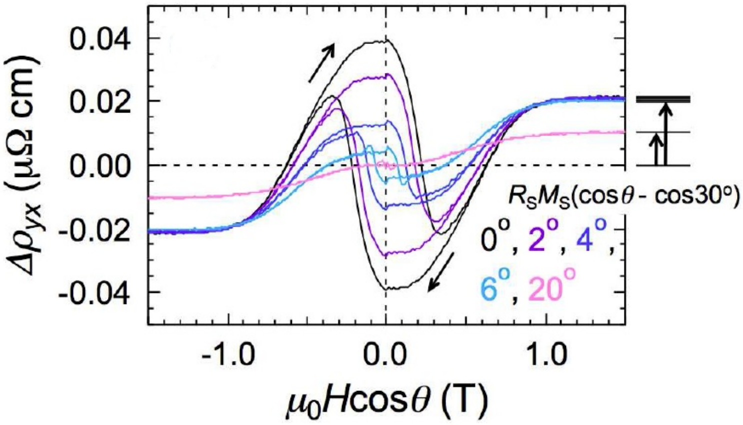

Figure 5.11: The figure above shows $\Delta\rho_{yx}$ at various inclination angles at 2 K in a 10 μm wide circuit. A sudden shrinkage of hysteresis loops represents declines in skyrmion numbers in FeGe system [99].

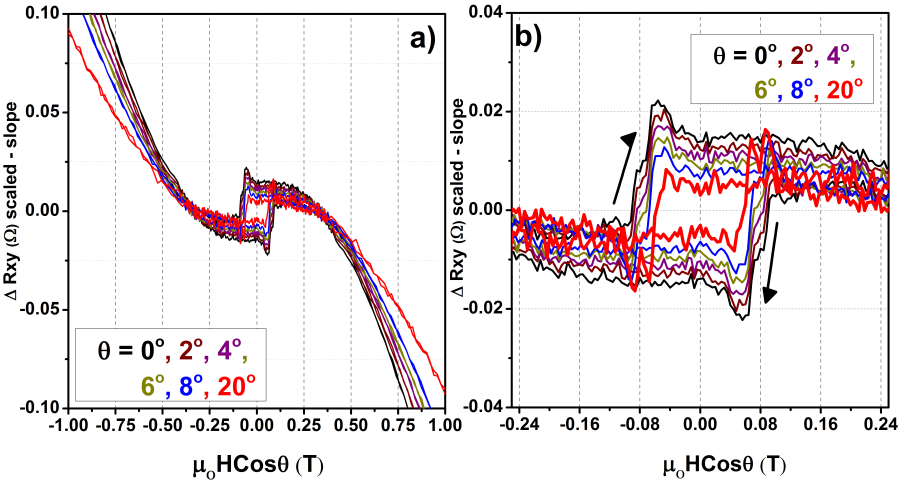

Figure 5.12: The figure above shows modified ΔR_{xy} obtained by subtracting a slope (obtained by linear fitting of the curves between suitable values). Panel a) shows the modified loops at higher fields, whereas, panel b) shows loops at lesser fields.

found by [32] for FeGe and MnFeSi system does not necessarily represent the critical angle for rest of the B20 material system. At least it may not be the critical angle for $Fe_{1-x}Co_xSi$ epilayer system. We may need to go to higher angles perhaps to completely destroy the skyrmion or such chiral structure. Also, going to higher magnetic field values might throw light on whether at the ΔR_{xy} curves converge or not and hence gives us a better insight in the physics involved in skyrmion formation. We, currently at Leeds can go up to 3T with the particular cryostat used to measure the angle dependent THE. The scaling factor used by Kanazawa *et al.* [99] to eliminate the remaining anomalous Hall component from ΔR_{xy} doesn't eliminate the anomalous Hall component completely as we have shown for the $Fe_{1-x}Co_xSi$ system where ΔR_{xy} at 20^o doesn't scale up at higher fields. The above discrepancies propels us towards newer methods to find skyrmion signature in these B20 material system.

Finally, we have shown various transport properties related to $Fe_{1-x}Co_xSi$ epilayers. OHE was used to determine the charge carriers and their mobility in $Fe_{1-x}Co_xSi$ epilayers. A positive MR was observed for the system which is a characteristic of this system and has been explained in the framework of quantum interference of electrons. A huge AHE was observed too. Angle dependent THE done with 3 T of applied magnetic field is inconclusive and needs to be done at higher magnetic field.

CHAPTER 6

Magnetometric characterisation

Various magnetometric characterisation techniques such as SQUID, MFM, XMCD etc. were used to understand the magnetic response as well as understand the evolution of magnetism in the $Fe_{1-x}Co_xSi$ thin films.

6.1 Vibrating sample magnetometry

VSM was used to measure the magnetisation in thin films as a function of applied magnetic field and variable temperature. It works on the principle of Faraday's Law which states that the electro motive force (emf) in a circuit is equal to the rate of change of the magnetic flux enclosed by the circuit and can be written as:

$$\varepsilon = -\frac{d\phi}{dt} \tag{6.1}$$

The sample is vibrated at a frequency of 55 Hz and any change in current generated due to the change in the magnetic flux in pick-up coil is amplified and interpreted by the lock-in. One can either measure the magnetisation in-plane or out of plane.

6.2 Superconducting quantum interference device (SQUID)

A Quantum Design Magnetic Property Measurement System (MPMS) SQUID magnetometer was used to measure the magnetic moment of the thin films over a wide range of applied magnetic field and temperatures. An MPMS system has four main components: a detecting coil; a superconducting quantum interference device; a magnetic shield; and a magnetic coil. SQUID is based on two main physical phenomena: Flux quantization in a superconducting ring and the Josephson effect.

Flux quantization, as long as the superconducting ring remains in superconducting state, the magnetic flux remains trapped within it. The trapped magnetic flux cannot change inside the ring in a continuous manner. It can only change by discrete levels i.e. the magnetic flux is quantized and exists in multiples of the flux quantum Φ. The quantization of the magnetic flux is due to the assumption that the Cooper pairs form standing waves inside the superconducting ring. Φ_o is given by the following equation

$$\Phi_0 = \frac{h}{2e} \tag{6.2}$$

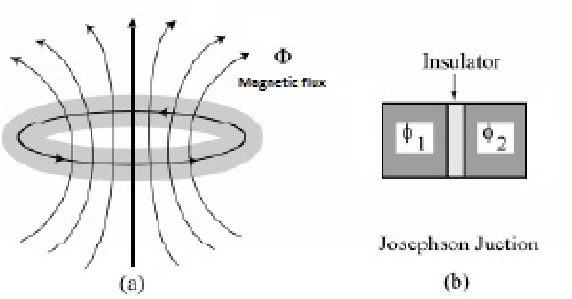

Figure 6.1: Left, Current circulating in a circular ring and the resulting magnetic lines of force. Right, a Josephson junction.

and the total flux in the superconducting ring is given by the following equation, n is an integer.

$$\Phi_T = n\Phi_0 \tag{6.3}$$

Josephson effect, when a current flows in a superconducting ring as shown in Figure 6.1 (a), then the magnetic flux in the ring can only be an integral multiple of the flux quantum. Any external field adds to the internal flux enclosed by the ring. Since external flux is not quantized, the current in the ring so adjusts that the net flux inside the ring becomes quantized. If two superconductors are separated by an insulator, as shown in Figure 6.1 (b), the waves of Cooper-pair electrons in different superconducting regions have different phase. These electron-pairs can tunnel across the insulating junction and the electron-pair waves between the two regions are coupled. This phenomenon is called the Josephson effect and the junction between the two superconducting regions is called the Josephson junction.

There are two type of SQUIDs, the dc-SQUID (direct current) having two Josephson junctions and the rf-SQUID (resonant frequency) which has only one junction. At Leeds, we used a Quantum Design MPMS SQUID VSM magnetometer. It uses a rf Josephson junction to detect magnetisation. The sample is moved up and down or vibrated in the detection coil with a frequency ω leading to a current in the detection coil, which is a function of the sample position (z). The induced current in the detection coil is inductively coupled to the SQUID ring that serves as a current to voltage converter. The SQUID voltage is given by the following equation

$$V(t) = AB^2 \sin^2(\omega t) \tag{6.4}$$

for small vibrations $V(z) = Az^2$ where $z(t) = B\sin(\omega t)$. A is a scaling factor related to the magnetic moment of the sample, B is the amplitude of sample vibration. The current in the detection coil is nulled by the SQUID feedback and no current actually flows through it and the feedback thus yields the actual SQUID voltage. Various instrument electronics are used to amplify the SQUID voltage. The DC component of the signal is proportional to 2ω of the measured signal and can be extracted from other noise signals. Quantum Design MPMS can measure in a temperature range of 1.8 K to 400 K and can apply a magnetic field up to 7 T. Samples can be measured in both in plane and out of plane geometry.

6.3 Magnetic force microscopy

Magnetic force microscopy is an imaging technique that is derived from tapping-mode atomic force microscopy [101]. In AFM, the van der Waals interaction is taken into account, whereas in MFM the magnetic stray fields or the magnetic force gradients emanating from the sample surface are measured to image the magnetic feature of interest. A cantilever with a tip coated with a ferromagnet is used to measure the stray field from the sample via the force $\vec{F}$, given by the following equation

$$\vec{F} = \nabla(\vec{m} \cdot \vec{B}) \tag{6.5}$$

where $\vec{m}$ is the magnetic moment of the cantilever tip and $\vec{B}$ is the stray field from the sample. The magnetic interaction of the cantilever with the sample surface forces the resonant frequency to change as a function of variation in the magnetic field gradient. The change in the frequency and the phase is used to map a magnetic surface profile of the sample. The MFM images are recorded in a two step process, the first step or the forward scan maps the topography of the sample surface, the tip is then retracted up to 20 nm and a backward scan collects the magnetic forces or maps the magnetic field gradient of the sample surface.

6.4 Soft X-ray spectroscopy

We used soft X-ray spectroscopy, U4B beamline stationed at Brookhaven National Laboratory, New York, USA to probe the origin of magnetism in $\mathrm{Fe}_{1-x}\mathrm{Co}_x\mathrm{Si}$ epilayers. U4B is a bending magnet beamline that has two monochromators, one that provides white x-rays in the energy range 80-1200 eV and the other, VUV branch that extends down to 20 eV. We used the 80-1200 eV branch for our experiments. The x-ray beam is then focused by a set of focusing mirrors and finally enters the entrance slit of the monochromator that is located further down the beamline. The entrance and exit slits can be adjusted so as to have either more intensity or better energy resolution. The endstation that was used had UHV, a magnet that could go up to 1.5T and a cryostat that could go down to liquid helium temperature. Samples were mounted onto a holder and a blob of sliver paint was used to drain the current from the sample. A current to voltage amplifier was used to measure the current that was drained in the total electron yield (TEY) mode. The intensity of the beam was normalised continuously by a Au grid beam monitor. Also, a magnetite sample is used as a reference for correction of systematic errors associated with the monochromator.

X-ray absorption spectroscopy (XAS)

XAS can be measured in many ways such as by transmission, where the intensity attenuation corresponds to absorption of photon leading to a core electron transition to an empty state. We, however, used total electron yield (TEY) and total fluorescence yield (TFY) modes to obtain XAS spectra of $\mathrm{Fe}_{1-x}\mathrm{Co}_x\mathrm{Si}$ thin films. In TEY mode like transmission a core electron makes a transition to an empty state leaving a hole behind. That hole is then filled by another electron, triggering a cascade of Auger electrons. The Auger electrons are typically emitted from the very surface of the sample ($\sim 2\ nm$) and can be measured using a picoammeter. In the case of TFY, an electron is excited to a higher energy state, decays to a meta stable stable state before relaxing back to the ground state by emitting a photon, giving rise to fluorescence. In the soft X-ray region the signal from TEY dominates over TFY. XAS measurements were done at room temperature using a linearly polarised light with high energy resolution of the monochromator. An absorption resonance occurs when the incoming photon has the same energy as that of the transition energy of an electron in the atom. We probed the L edges corresponding to $2p \rightarrow 3d$ transition of Fe and Co atoms in $\mathrm{Fe}_{1-x}\mathrm{Co}_x\mathrm{Si}$

thin films. Due to SOC the orbital degeneracy of the p orbital is lifted and we get two different peaks, L_3 and L_2 corresponding to $2p_{3/2} \rightarrow 3d$ and $2p_{1/2} \rightarrow 3d$ transitions respectively. The subscript with p represents the total angular momentum (J), which is a sum of azimuthal quantum number (l) and spin quantum number (s) The structure of the resonance peak reveals the electronic band structure and the chemical environment of the associated element.

X-ray Magnetic Circular Dichroism

The underlying mechanism of XMCD is similar to that of XAS but unlike XAS where a linearly polarised light is used, a circularly polarised light is used for XMCD. The XMCD experiment essentially consists of measuring the difference in the absorption spectra of the left handed and right handed circularly polarised light. Photons of different helicity have different angular momentum ($\hbar$), it could be parallel ($+\hbar$) or antiparallel ($-\hbar$) to the wave propogation vector **k**. In the case of 3d ferromagnets, d band or the valance band is already exchange split into spin up and spin down bands and act as a spin detector. On the other hand, upon application of external magnetic field the core level p orbital loses orbital degeneracy due to Zeeman splitting and results in $2p_{3/2}$ and $2p_{1/2}$ orbitals. The orbitals thus created have opposite spin orbit coupling (j), L_3 edge ($j = l + s$) and L_2 edge ($j = l - s$), where l is the angular momentum, s is the spin moment. XMCD can be explained using a two step model as proposed by Stohr et al. The first step consists of transfer of angular momentum from the incident circularly polarised photons to the excited photoelectrons in the p orbital. The angular momentum is conserved by transferring the moment to spin via spin orbit coupling and the photo electrons thus generated are spin polarised. The quantisation axis of the spin polarised electrons is identical to that of the photon spin. The second step consists of the exchange split d band acting as spin detector for the excited photoelectrons. By setting the magnetisation **M** of the d band parallel to **k** the occupation of spin down states is larger than the spin up states. Due to spin conservation photoelectrons undergoing $2p_{3/2} \rightarrow 3d$ ($2p_{1/2} \rightarrow 3d$) by spin up photons (spin down) mainly probe spin up states (spin down states) above the Fermi level. The dipole operator doesn't interact with the spins and thus no spin flip is involved. The selection rules are as follows:

$$\Delta l = \pm 1 \tag{6.6}$$

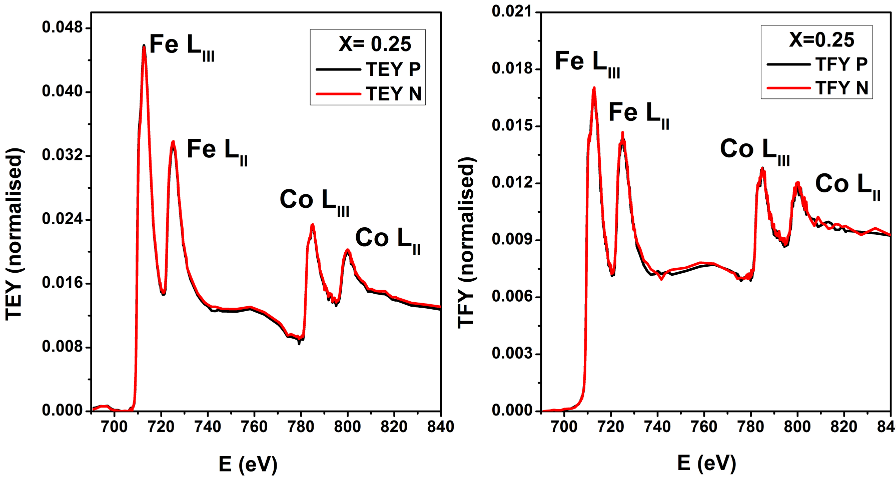

Figure 6.2: XMCD spectras obtained by TEY mode (left) and TFY mode (right) for $Fe_{0.75}Co_{0.25}Si$. The red and black spectra are obtained using right circularly polarised light and left circularly polarised light respectively. The difference between these spectra gives us the dichroism in the material.

$$\begin{aligned} \Delta m &= +1, \textit{Right circularly polarised photons} \\ &= -1, \textit{Left circularly polarised photons} \end{aligned} \tag{6.7}$$

Fig 6.2 shows a typical XMCD spectra for $Fe_{1-x}Co_xSi$ thin film obtained by both TEY and TFY modes. The difference in the intensity by left and right circularly polarised light can be by given by following equation

$$I_{XMCD} = I^- - I^+ \tag{6.8}$$

The intensity or the magnitude of the dichroism is dependent on the degree of photon polarisation (P_{photon}), expectation value of the magnetic moment of 3d band $\langle$ m $\rangle$ and the angle (θ) between magnetic moment (m) and angular momentum of photon ($\hbar$), the following equation then shows the dependence of the XMCD intensity

$$I_{XMCD} \propto \; P_{photon}\hbar \tag{6.9}$$

XMCD and XAS are element specific techniques, using sum rules [102] the intensity of experimentally obtained spectra can be integrated to yield the orbital (m_{orb}) and spin (m_{spin}) moments of the individual elements by the following equation.

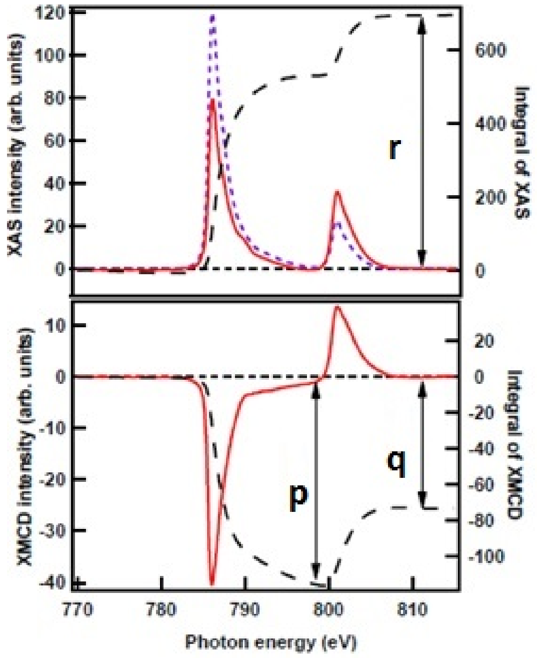

Figure 6.3: The figures above show the intensity (XAS, top) and difference (XMCD, bottom) spectra. p, q, and r that are used in the sum rules are labelled on the integrated MCD data (dashed line) on the right hand side of the graphs. For the XAS data, a linear background is subtracted and then normalised to the post-edge signal (Nielson and McMorrow).

$$m_{orb}[\mu_B/atom] = \frac{-4q(10 - n_{3d})}{3r} \tag{6.10}$$

$$m_{spin}[\mu_B/atom] = \frac{-(6p - 4q)(10 - n_{3d})}{r} \tag{6.11}$$

p, q, and r are the integrated intensities of XAS and XMCD spectra and is shown in fig. 6.3 by dashed lines in black and have been labelled appropriately. n_{3d} represents the number of holes in the 3d ferromagnet. In the case of $3d$ ferromagnets the m_{orb} is quenched and hence the over all magnetic moment in the system is dominated by m_{spin}.

6.5 Results and Discussion I (Magnetic properties)

Magnetic characterization of $Fe_{1-x}Co_xSi$ epilayers were carried out using a vibrating sample magnetometer (VSM) with a sensitivity of 10^{-9} Am^2 and a SQUID magnetometer with a sensitivity of 10^{-11} Am^2. For measurements in the VSM, several pieces of sample cut from the same wafer were stacked up to increase the signal. The temperature dependence of the magnetization of the films was measured with a 10 mT field applied in the film plane, the results are shown in Fig.6.4(a). The critical temperatures for magnetic ordering were determined from these curves. Since $\mathrm{Fe}_{1-x}\mathrm{Co}_x\mathrm{Si}$ is helimagnetic, we refer to an ordering temperature T_{ord}, rather than a Curie temperature. The values of T_{ord} obtained for the various films have been plotted as a function of Co content x and shown in Fig. 6.4(b). When compared with corresponding data for bulk samples,[13; 67] we see that for our $\mathrm{Fe}_{1-x}\mathrm{Co}_x\mathrm{Si}$ epilayers T_{ord} has been significantly increased, and is as high as 77 K for the $x = 0.4$ epilayer. Enhanced ordering temperatures with respect to bulk have also been observed in MnSi epilayers by Karhu *et al.*, [27; 29] and subsequently by Engelke *et al.*[31] and Yokouchi *et al.* in the case of Fe doping.[32]

We attribute this increased stability of the magnetic ordering in our $\mathrm{Fe}_{1-x}\mathrm{Co}_x\mathrm{Si}$ epitaxial films to the epitaxial strain. As shown in Fig. 4.18(e), the biaxial in-plane strain increases the unit cell volume with respect to the bulk. Studies of bulk crystals of $\mathrm{Fe}_{1-x}\mathrm{Co}_x\mathrm{Si}$ under hydrostatic pressure show that compressing the unit cell volume suppresses magnetic order and can even induce a quantum phase transition in the system.[96] Based on this argument, we conclude that the epitaxial strain in these $\mathrm{Fe}_{1-x}\mathrm{Co}_x\mathrm{Si}$ systems stabilizes the magnetic order and increases T_{ord} for the whole range of x.

We determined the magnetic moment at saturation, in units of Bohr magnetons (μ_{B}) per formula unit (f.u.), from these hysteresis loops. The results are plotted as a function of x in Fig. 6.4(c). Our results are comparable to the findings of Manyala *et al.* for bulk crystals,[3] and largely in line with theoretical expectations.[33] As found previously, we see that each Co atom contributes ~ 1 μ_{B} up to a limit of $x \approx 0.25$. Beyond this point, the total moment is roughly constant at ~ 0.25 μ_{B}/f.u. The dashed line in Fig. 6.4(c) represents the ideal result of exactly 1 μ_{B}/f.u. We can see that in the low x range there is a small excess of moment per Co above the ideal result, suggesting that the Co dopants could be weakly magnetizing nearby Fe atoms in this regime. In Fig. 6.5, we show the magnetic moment per electron as a function of x for our epilayer samples. The moment is determined from the magnetometry results in Fig. 6.4(c) and the number of carriers from the Hall effect, as given in Fig. 5.5. The data show a

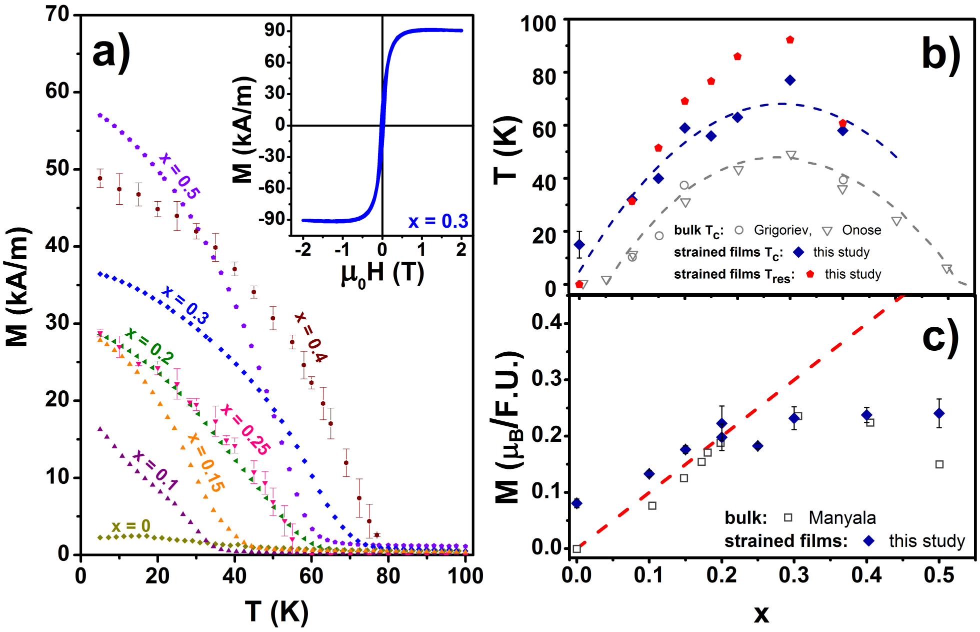

Figure 6.4: Magnetic characterization of the $Fe_{1-x}Co_xSi$ epilayers.(a) Magnetization as a function of temperature in an in-plane 10 mT field. The Co concentration, x, of the films is labeled on the graph. The inset shows a typical magnetization (M versus H) loop for a $Fe_{1-x}Co_xSi$ ($x = 0.3$) film measured at 5 K in an out-of-plane field orientation. Larger error bars correspond to measurements by VSM. b) The ordering temperature T_{ord} of the epitaxial thin films shows an enhancement with respect to that of bulk material.[13; 67] FeSi ($x = 0$) shows weak ferromagnetism with $T_{\mathrm{ord}} \sim 10$ K. T_{res}, determined as discussed in §5.2, is up to 10K higher than T_{ord}. The dashed lines are guide to the eye. (c) The saturation magnetization at 5 K, extracted from hysteresis loops of the films, expressed in Bohr magnetons per formula unit. The value is close to $1 \sim \mu_B$ per cobalt dopant atom (ideal relationship shown by the dashed line), in good agreement with bulk,[3] for $x \lesssim 0.25$.

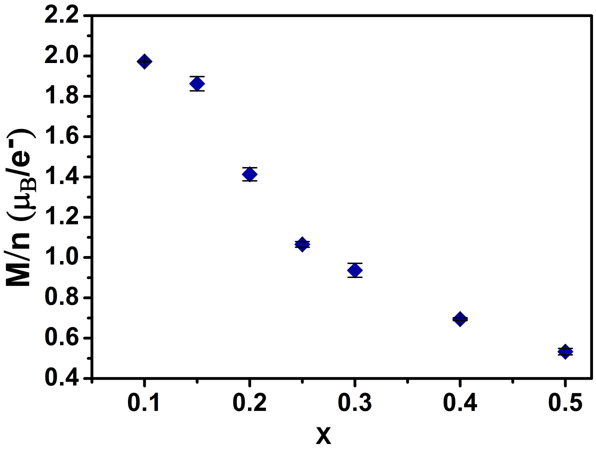

Figure 6.5: Magnetic moment per carrier of the electron gas in $Fe_{1-x}Co_xSi$ as a function of cobalt doping x.

monotonic decrease in this ratio as the Co content x rises.

6.6 Results and Discussion II (XAS and XMCD)

As mentioned before, to investigate the electronic structure and evolution of magnetism in $Fe_{1-x}Co_xSi$ system we used X-ray absorption spectroscopy and X-ray magnetic circular dichroism respectively in total electron yield mode (TEY) to probe the $L_{2,3}$ edges of Fe and Co in $Fe_{1-x}Co_xSi$ thin films. The $Fe_{1-x}Co_xSi$ films used for this experiment were capped in situ with Au (approx. 1.5 nm) to prevent any oxidation and thus surface degradation The films were saturated in the out of plane direction such that the sample magnetisation **M** was parallel to the wave propagation vector **k**. XAS was done in an UHV chamber at room temperature using a linearly polarised light. XAS is an element specific technique, Fig 6.6 shows a set of normalised XAS spectra of both Fe, Co at $L_{2,3}$ edges as a function of varying Fe and Co doping in $Fe_{1-x}Co_xSi$ thin films.

Single sharp peaks at L_2 and L_3 edges indicate the metallic nature of both Fe and Co atoms in $Fe_{1-x}Co_xSi$ epitaxial thin film system. As can be seen from the figure, the spectral weight of L_2, L_3 edges for both Fe and Co atoms are more or less in a constant ratio [103] Also, the relative spectral weight of Fe and Co peaks shift as a function of Fe and Co doping. We observe the Fe edge in FeSi with zero Co doping, it has the highest

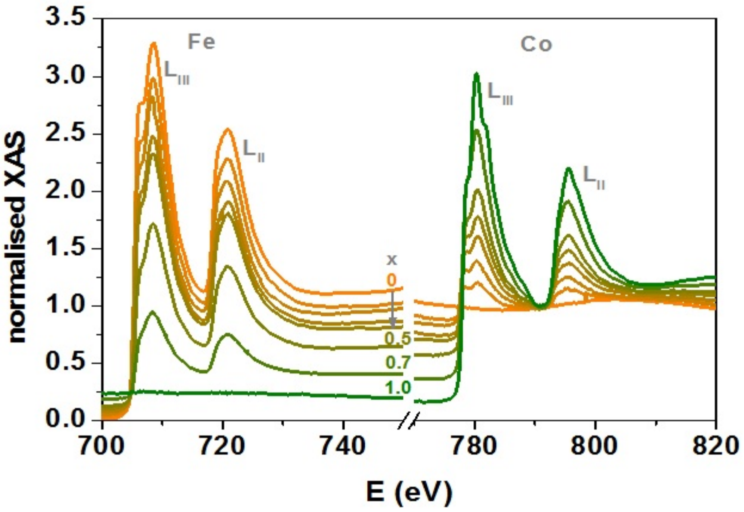

Figure 6.6: XAS spectra of $Fe_{1-x}Co_xSi$ thin films of varying Co and Fe doping. The normalised XAS spectra shows the evolution of characteristic $L_{2,3}$ edges of Fe and Co respectively. Along with the Fe and Co edges a shoulder on L_3 is also observed.

spectral weight. As we dope FeSi with Co, the Fe edge loses spectral weight and it shifts towards Co edge and is the highest for CoSi. This may be attributed to the fact that as we dope Co in FeSi system, each Co atom substitutes Fe atom in the crystal structure and thus slowly dominates the whole spectra when it replaces Fe completely to become CoSi. L_3 edges of Fe and Co atoms are accompanied by a shoulder indicating a hybridisation in epitaxial B20 structure. Evolution of the L_3 edge for both Fe and Co is shown in fig 6.7 and 6.8 respectively.

In fig 6.7, the spectrum at the top has well resolved shoulder and peak for FeSi, as Co doping (**x**) increases or Fe doping decreases the shoulder and the main peak become less resolved until they are no longer distinguishable and vice versa for fig 6.8, where the most well resolved peak is observed for $Fe_{1-x}Co_xSi$ with x = 0.7, and as the Co doping decreases or Fe doping increases the peak and the shoulder are indistinguishable from each other. Additionally, we also observe a shift in the resonance energy level of both $L_{2,3}$ edges of Fe and Co. Both the edges are move by approximately 500 meV indicating a change in the band structure. Since $Fe_{1-x}Co_xSi$ thin films are biaxially strained due to epitaxy, a change in the band structure with changing composition of the film (Co doping) is not necessarily surprising. In order to extract quantitative

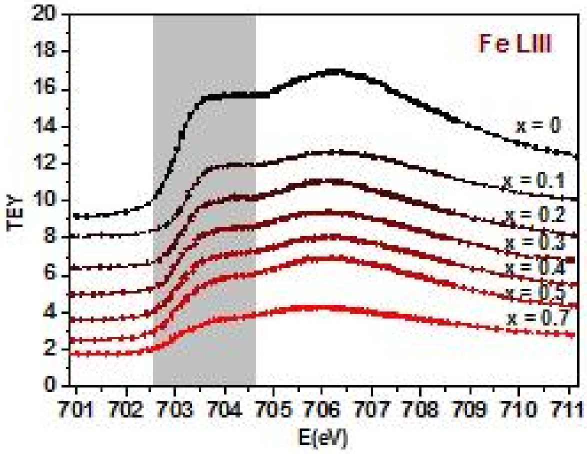

Figure 6.7: XAS spectra of $Fe_{1-x}Co_xSi$ thin film showing the evolution of characteristic L_3 edge of Fe with varying doping content. The shaded area highlights the evolution of the shoulder on the main L_3 edge of Fe, the edges are also shifted by 500 meV, both of which when combined together indicates a modified band structure of the system.

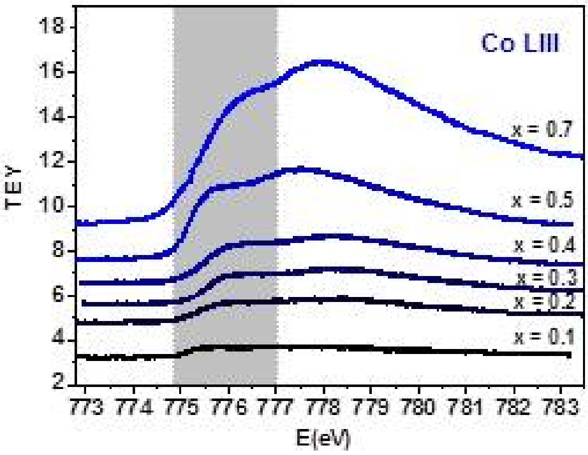

Figure 6.8: XAS spectra of $Fe_{1-x}Co_xSi$ thin film showing the evolution of characteristic L_3 edge of Co with varying doping content. The shaded area highlights the evolution of the shoulder on the main L_3 edge of Co, the edges are also shifted by 500 meV; both of which when combined together indicates a modified band structure of the system.

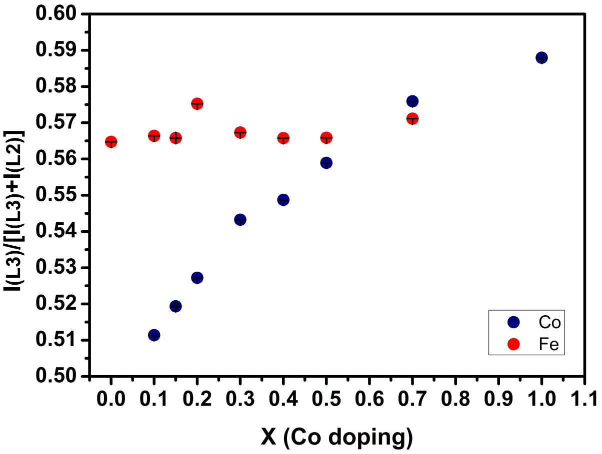

Figure 6.9: The variation in the Branching ratio of Co (blue) and Fe (red)with varying contents in $Fe_{1-x}Co_xSi$ thin films. The branching ratio of Fe remains almost constant (varying little) where as that of Co increases with increasing Co doping. This suggests that the number of core holes associated with Co increases from x=0.1 to x=0.5 where as that associated with Fe changes little.

information from the XAS data and to understand the electronic structure better we calculated the branching ratio. The element specific branching ratio (BR) is calculated by the following 6.6 and the results are shown in fig 6.9

$$BR = \frac{I(L_3)}{I(L_3) + I(L_2)} \tag{6.12}$$

Branching ratios obtained from XAS spectra of Co increases from 0.51 ($x = 0.1$) to 0.56 ($x = 0.5$) and that of Fe deviates little from 0.56. As a function of x, it suggests that the number of core holes associated with Co increases from x=0.1 to x=0.5 where as that associated with Fe changes little. Variation in the occupation states of Fe and Co atoms coupled with shift in $L_{2,3}$ edges ($\sim 500\ meV$) and the evolution of the L_3 edge line shape indicates a modified band structure.

XMCD was done in an identical geometry as XAS but at 6 K and with 70% circularly polarised light. The helicity of the circularly polarised X-rays were preserved and magnetisation (**M**) of the sample was reversed by changing the polarity of the magnets. Dichroism was obtained as a difference of two absorption spectra under different magnet polarities. Fig 6.2 shows XMCD spectra taken in TEY and TFY modes. Qualitatively,

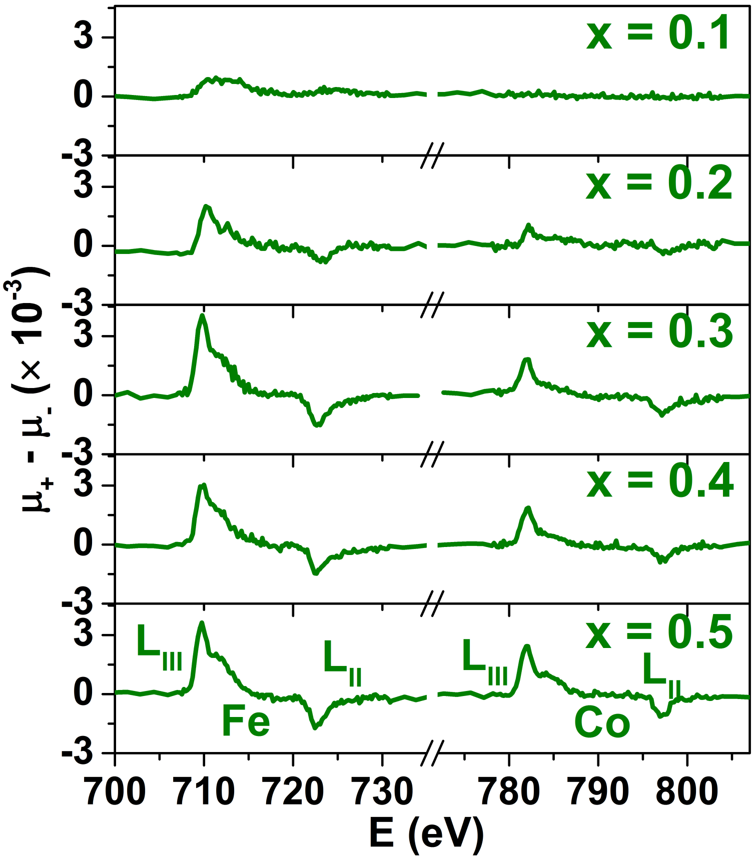

Figure 6.10: Evolution of dichroism on $l_{2,3}$ edges of Fe and Co atom. As the doping increases, the dichroism become more pronounced on both the Fe and Co edges.

the $L_{2,3}$ peaks in both TEY and TFY modes appear the same with similar features indicating that the surface characteristics of the sample is representative of the bulk as TEY arises from the auger electrons ejected close to the sample surface whereas TFY arises from much deeper end of the sample. The fact that both the spectra are identical indicates that the Au capping layer has preserved the sample in its native state and no oxidation has taken place. Fig. 6.10 shows the systematic evolution of dichroism on $L_{2,3}$ edges of both Fe and Co with increasing Co doping ($\mathbf{x}$). The dichroism on Fe L3 edge (TEY) varies from 0.6×10^{-3} for x=0.1 to 1.4×10^{-3} for x=0.5 and that of Co evolves from being negligible for x=0.1 to 1.7×10^{-3} for x=0.5. Whilst the magnetism in the $\mathrm{Fe}_{1-x}\mathrm{Co}_x\mathrm{Si}$ system arises from the Co doping, these asymmetry spectra clearly show that the magnetic moment is delocalised on both Co and Fe sites.

XMCD in combination with the branching ratio calculation throws light on the evolution of magnetism in $\mathrm{Fe}_{1-x}\mathrm{Co}_x\mathrm{Si}$ system but a complete picture can only be obtained with the band structure calculations. When FeSi, which is a non magnetic semiconducting system is doped with Co, Co atom substitutes for an Fe atom in the unit cell. By doing so, the Co atom donates a free d electron and modifies the band structure. More the substitution of Co atom for Fe atom, more the availability of d electrons. The branching ratio of Co supports the same, we see that with increasing Co doping the branching ratio (no. of holes) increases from 0.51 for Co=0 to 0.59 for Co=0.5. When we compare this with the XMCD data, we see that the dichroism associated with Co increases with increasing Co doping. The dicroism on the Fe edge increases slowly with increasing Co doping but after Co doping of 0.3, the dichroism on Fe remains more or less constant but that on Co increases. This indicates that by the time Co doping reaches 0.3, it magnetises all the Fe atoms in the available vicinity. We can deduce from all above is that the Co atom induces magnetisation in the nearby Fe atom. The net magnetisation of the $\mathrm{Fe}_{1-x}\mathrm{Co}_x\mathrm{Si}$ system has contribution not only from Co atom but Fe atom as well. This also explains why magnetic moment was $\geq 1\mu_\mathrm{B}/e^-$. Exchange interaction between Co and Fe atom could be one of the reasons that can be attributed to the increased magnetisation of the system. Also, along with inducing magnetism, the d electron contributed by Co atom can hop locally from one atom to the other in the crystal structure. All of which suggests itinerant magnetism in $\mathrm{Fe}_{1-x}\mathrm{Co}_x\mathrm{Si}$ epitaxial system. Although the previous studies by Ishimoto et al. [69] and DeGrave et al [41] showed that elemental origin of magnetism in system is due to Co atoms. In the case of $Fe_{1-x}Co_xSi$ epitaxial system both Fe and Co edges show evolution of dichroism, along with the branching ratio calculations confirms the presence of itinerant magnetism in FeCoSi system.

6.7 Results and Discussion III (MFM)

MFM imaging of $Fe_{1-x}Co_xSi$ ($x = 0.3$) thin film was carried out at Attocube, Germany using their standard AFM/MFM I scanning probe within a cryogen free attoDRY1000 system. The sample was mounted on a scanning probe stage and glued to it such that the sample plane normal was parallel to the tip. A Point Probe Plus magnetic force Microscopy- Reflex coating (PPP-MFMR) tip with an effective magnetic moment of 10^{-13} emu was used. The magnetisation direction of the tip was parallel to the sample plane normal. This ensured that the tip picked up only the changes in the out of plane direction of the sample plane. The tip resolution was better than 50 nm, effectively it was close to 20 nm. The sample was Zero Field Cooled (ZFC) to 4 K and an external magnetic field was applied in the out of plane direction to the sample plane.

The external magnetic field was varied so as to trace a five segment loop similar to a standard M-H loop, starting from 0 Oe to $\pm 20,000$ Oe (shown in fig. 6.11). The magnetic force gradient of the sample was mapped using the MFM tip and images were acquired at various applied field values. For convenience the five segment loop is described in the table 6.7

Segment Number	Initial magnetic field (Oe)	Final magnetic field (Oe)
1	0	20,000
2	20,000	0
3	-200	-20,000
4	-800	0
5	200	400

A series of MFM images of the same area were taken over a period of time under different applied magnetic field. Variation in both frequency and phase components were recorded. A set of images from segment 3 is as shown in the fig. 6.12. First two columns of the image show the raw images thus acquired.

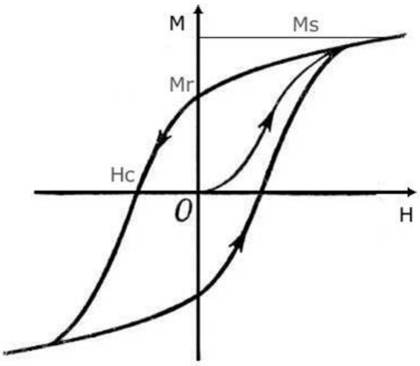

Figure 6.11: A typical M-H loop showing hysteresis. The M-H loop above can be divided into five segments as shown in the table below.

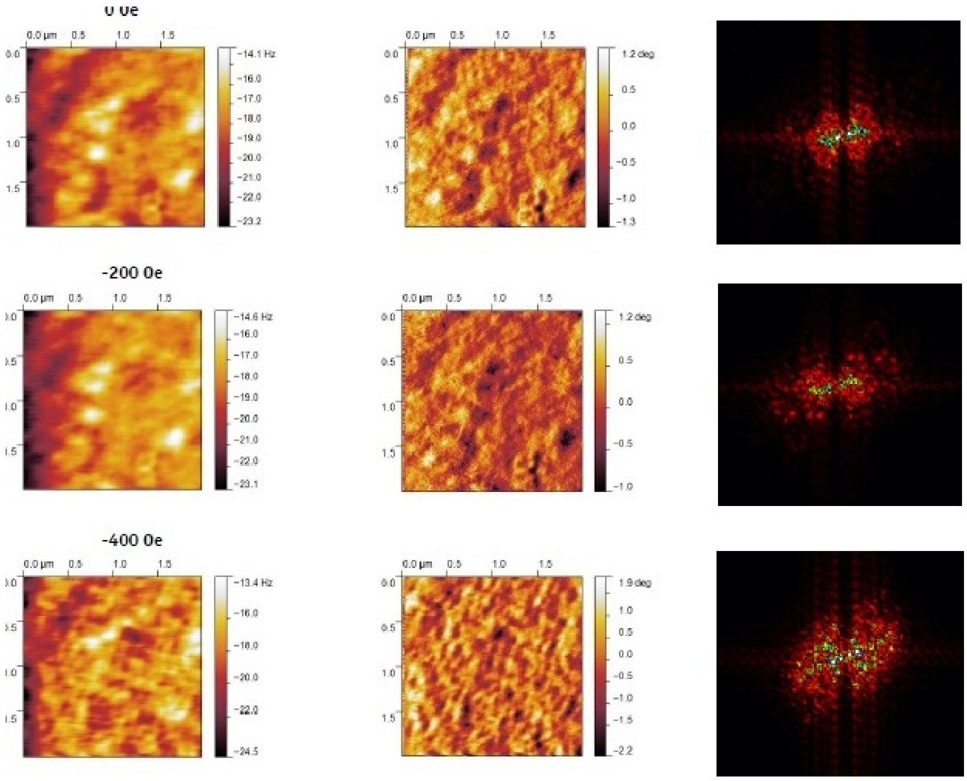

Figure 6.12: The images are obtained from loop 3 (described before in the table) of $Fe_{0.7}Co_{0.3}Si$ thin film for lower field values. The images were mapped as a function of applied magnetic field, the values of which are mentioned at the top of the images in the first column. The first column represents the frequency variation, the second column represents the corresponding phase variation and last column shows the corresponding FFT of the phase component. Figure continued on the next page.

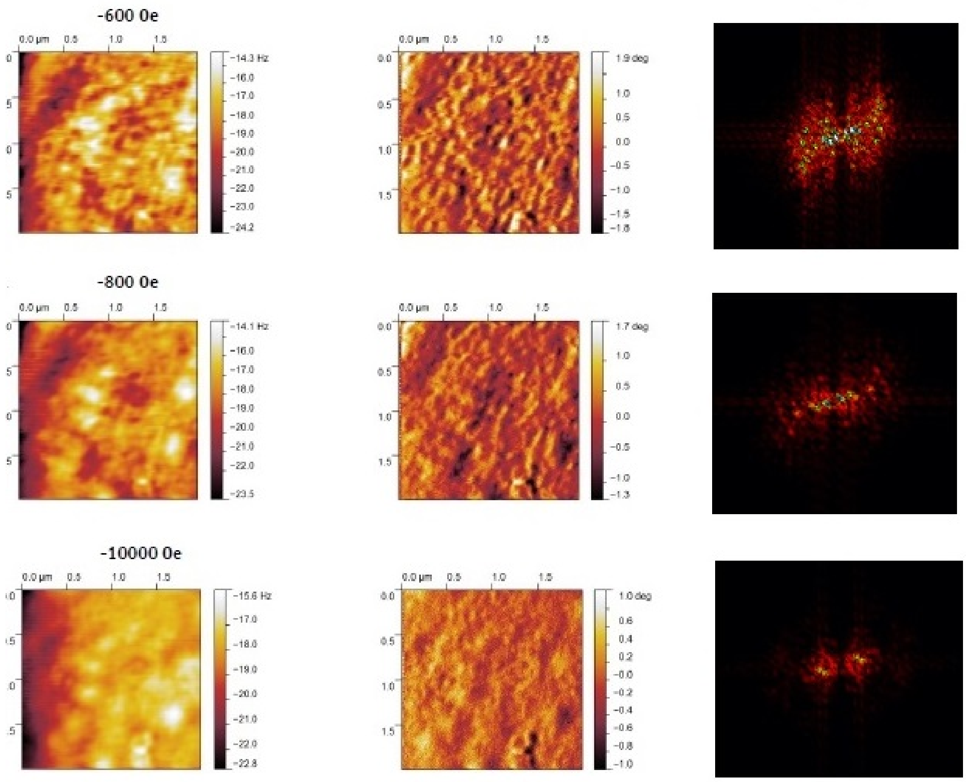

Figure 6.13: The images are obtained from loop 3 (described before in the table) of $Fe_{0.7}Co_{0.3}Si$ thin films for higher field values. The images were mapped as a function of applied magnetic field, the values of which are mentioned at the top of the images in the first column. The first column represents the frequency variation, the second column represents the corresponding phase variation and last column shows the corresponding FFT of the phase component.

Qualitatively, from one image to the other, we observe variation in frequency and phase components as a function of external magnetic field. $Fe_{1-x}Co_xSi$ is a helimagnet in the ground state and as we increase the external magnetic field it changes conformation, saturates at higher fields, and behaves like a ferromagnet. However, to understand and determine the ordering degree we need to quantify the changes. Analytical tools such as auto-correlation and Fast Fourier transform(FFT) that were inbuilt in WSxM image processing software were used for such analyses.

Auto-correlation or self-correlation function has been widely used to analyse scanning probe images. Mathematically, it is essentially a convolution of a function with itself. For analysing images that are spatially defined and are real and bounded, it is equivalent to comparing all the possible pixel pairs in an area and estimating the likelihood that both will be bright as a function of the distance. The equation below elaborates the auto-correlation function used.

$$G(n\delta, m\varepsilon) = \Sigma_{n,m} f(x,y) f(x+n\delta, y+m\varepsilon) \tag{6.13}$$

Here $f(x,y)$ is the raw image matrix and $G(n\delta, m\varepsilon)$ is the auto-correlated image matrix. $f(x,y)$ and f $(x+n\delta, y+m\varepsilon)$ are the measured intensities of the image areas with (x,y) and $(x+n\delta, y+m\varepsilon)$ coordinates respectively, δ and ε are the pixel length along x and y axes, respectively, and n, m are any integer numbers.

The phase component of the MFM images were auto-correlated using the equation above. We next used FFT to analyse the auto-correlated images. In other words we used Wiener-Khinchins theorem which states that the Fourier transform of an autocorrelation function is the power spectrum. The power spectrum helps to understand how the intensity or strength of a signal is distributed in the frequency domain relative to the strength of other signals present. A periodic signal will have peaks at a fundamental frequency and its corresponding harmonics; a quasiperiodic signal will have peaks at linear combination of two or more irrationally related frequencies and appear as a main peak with sidebands; and chaotic dynamics will have broad band components in the spectrum.

An example of such an analysis is as shown in the fig.6.12 where the first column represents the frequency change, the second column represents the phase change, and the third column shows the Fast Fourier Transform of the corresponding auto-correlated images (phasecomponent). We explain the results thus obtained within the limits of the resolution of the MFM tip. As a function of magnetic field we observe changes in both phase and frequency component in the MFM images of $\mathrm{Fe}_{1-x}\mathrm{Co}_x\mathrm{Si}$ ($x = 0.3$). In the first column of fig.6.12, as the magnitude of external magnetic field increases from -200 Oe the frequency distribution of the image changes and slowly reaches the maximum saturation point at around -600 Oe where we observe certain patches or spots that appear saturated and white. Beyond -800 Oe the external magnetic field saturates the film, the white saturated spots disappear and sample shows uniform distribution of frequency again. Similarly in the second column we observe changes in the distribution of phase component. As a function of increasing magnetic field domain like features seem to appear and reinforce themselves between -400 Oe and -800 Oe, the features smooth out at other magnetic fields. For better understanding of the magnetisation dynamics we auto correlated the phase component of the images and obtained the power spectrum by FFT of the auto correlated images, the result is shown in the third column of the same figure 6.12. As the magnetic field increases in magnitude we observe distinctive frequencies appearing. The frequencies seem to appear in a preferential direction, indicating that the ground state or the helimagnetic state has a preferential direction of order. For a well ordered lattice such as that of a skyrmion with six fold symmetry we should observe a hexagonal pattern in the FFT. We, however, observe multiple strong frequencies overlaying the hexagonal pattern (if any, as the MFM tip has limited resolution) so much so that it is difficult to resolve and conclude. We, however, can measure the ordering parameter of the $\mathrm{Fe}_{1-x}\mathrm{Co}_x\mathrm{Si}$ thin film as it undergoes changes under the varying magnetic field. Ordering parameter(OP) can be determined from FFT by the following equation

$$OP = \frac{I}{FWHM} \tag{6.14}$$

where OP is the spatial ordering parameter, I is the intensity of the spot, FWHM is the Full Width at Half Maxima of the peak frequency mapped (line scan through FFT). This ratio has been widely used [104] to extract OP for various images representing various degree of orderliness. To obtain the ratio we did a line scan across the observable frequencies in the FFT and focussed on mapping the OP of the frequency with highest intensity, in the present case it is the frequency at the centre that appears with highest intensity. We chose it as it can be identified in every acquired image unlike the others

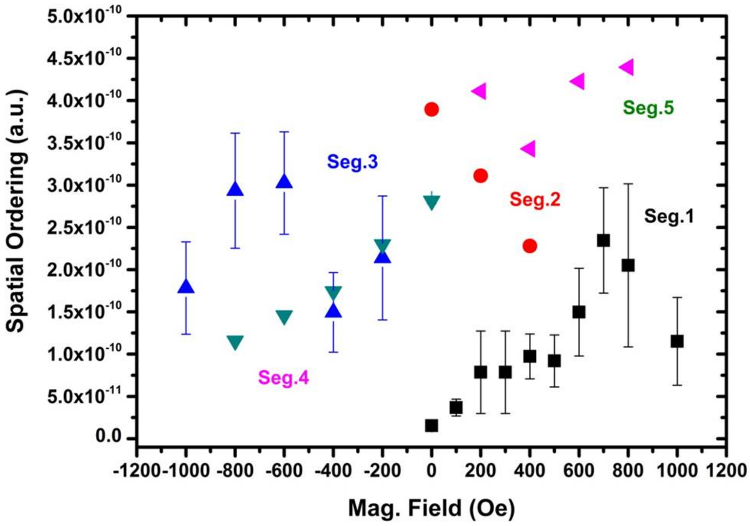

Figure 6.14: The figure above shows the variation of spatial ordering parameter as a function of applied magnetic field. We start with black squares (loop 1), then move to red circle (loop 2), then to blue triangles (loop 3), then to green triangles (loop 4), and finally to pink triangles (loop 5).

that fade away as a function of magnetic field. We then fitted the peak to obtain I and FWHM. The result is shown in fig.6.14.

We observe a pattern in OP as we proceed from segment 1 to segment 5. As the magnitude of the magnetic field is increased from zero to higher up values, the OP increases and reaches a maximum at around 700 Oe and then starts to decrease again, segment 1 and segments 3 follow the same pattern. However, OP follows a monotonic behaviour when magnitude of the magnetic field is decreased from a higher value to zero Oe. We also observe that the frequency pattern at 0 Oe after a cycle does not return to the original ground state that was observed after ZFC. Similar pattern has been observed by Milde *et al* [79]. The highest OP that is observed around ±700 Oe in both 1 and 3 segments are an indication of constructive magnetic ordering in the epitaxial $Fe_{1-x}Co_xSi$ system. Coincidently highest Topological Hall Effect for these system is also observed at around the same field values by Porter *et al* [100]. It can there be explained that when electrons pass through a well ordered chiral structure such as skyrmions, they couple to them and pick up a Berry phase. Each skyrmion has one quantum flux associated with it. The Berry phase of the electrons in the epitaxial $Fe_{1-x}Co_xSi$ system is manifested in the transport measurements as an extra

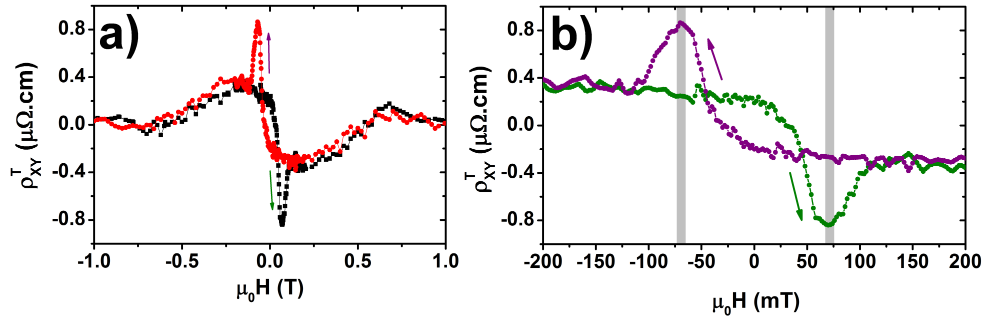

Figure 6.15: The figure above shows the THE contribution from $Fe_{0.7}Co_{0.3}Si$ thin film. The highest THE observed around 70 mT or 700 Oe. The fig. a) on the left shows THE at extended fields where as the fig. b) on the right shows THE at lower fields. The shaded area points to the maximum observed in the data [100].

signal i.e. giant Topological Hall Effect (THE). Therefore the combination of both the data strongly suggests towards a skyrmion like chiral behaviour and ordering in the $Fe_{1-x}Co_xSi$ system.

6.8 Results and Discussion IV (Thickness varying $Fe_{0.8}Co_{0.2}Si$ thin films)

Figure 6.16 shows the magnetisation versus temperature curves of $Fe_{0.8}Co_{0.2}Si$ thin films of varying thickness. The nature of magnetisation curves are very different for films with thickness more than or less than 10 nm. This could possibly be due to the some congregation or cluster formation in the films with lower thickness. But, nevertheless, magnetisation of the film varies with varying temperature and drops off to zero above the ordering temperature. The inset in the figure 6.16 shows the ordering temperatures of the films. The ordering temperature increases as thickness of the film increases from 2.5 nm ($\sim$ 5 K) to 10 nm ($\sim$ 36 K) and then decreases monotonically to 33 K for a 50 nm film. This is a significant result as it has previously been reported by Karhu *et al.* that the ordering temperature of a film does not change at all after reaching the critical thickness. We, however see that it does change, ever so slightly in $Fe_{1-x}Co_xSi$ epilayer, indicating that one can engineer the band structure and hence change the ordering temperature by engineering strain in the $Fe_{1-x}Co_xSi$ epilayers.

Figure 6.17 shows the variation between the ordering temperature and the corres-

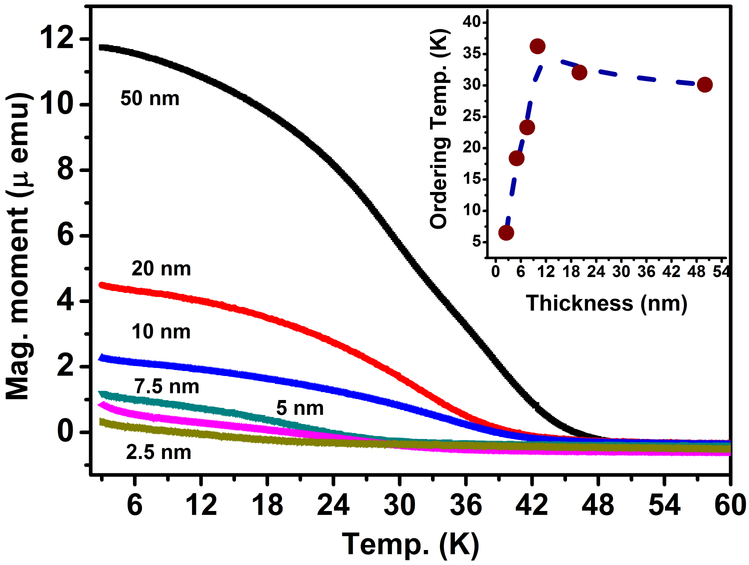

Figure 6.16: The figure above shows the variation in magnetisation as a function of temperature in $Fe_{0.8}Co_{0.2}Si$ thin films of varying thickness. The inset shows the variation in ordering temperature as a function of thickness. The ordering temperature increases as the thickness of the $Fe_{0.8}Co_{0.2}Si$ thin films increases from 2.5 nm to 10 nm, after it peaks at 10 nm, it slowly drops down to lower temperatures for higher thickness. The blue dashed line in the inset is a guide to the eye.

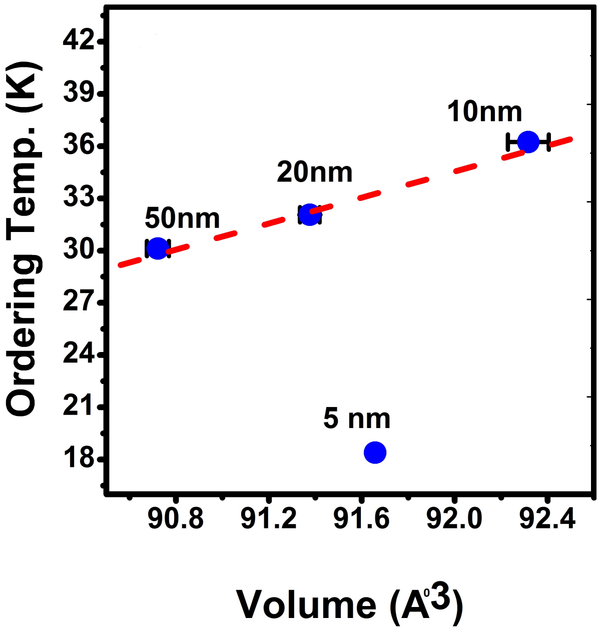

Figure 6.17: The figure above shows the variation in ordering temperature of $Fe_{0.8}Co_{0.2}Si$ thin film as a function of unit cell volume. The data points have been labelled with corresponding thickness of the films. The red dashed line is a guide to the eye.

ponding volume of the unit cell. The graph shows a linear relationship between the Ordering temperature and unit cell volume for films thickness 10nm and above. This indicates that the films are phase pure and that there is no phase change after the critical thickness is reached.

CHAPTER 7

Conclusion

In this thesis I have reported the growth and characterisation of phase pure, high quality ε- $\mathrm{Fe}_{1-x}\mathrm{Co}_x\mathrm{Si}$ thin films (50 nm) by MBE. It has been shown that changing the Co doping changes the band structure, modifies structural, chemical properties, and contributes to a fully spin polarised electron gas in the system. The biaxial strain changes the unit cell structure from cubic to rhombohedral and increases the ordering temperature of these epilayers. Evolution of dichroism on both the Fe and Co edges as shown by XMCD is indicative of itinerant magnetism in $\mathrm{Fe}_{1-x}\mathrm{Co}_x\mathrm{Si}$ epitaxial system. MFM, angle dependent THE, and PNR [100] indicate the presence of chiral or skyrmionic structures in $\mathrm{Fe}_{1-x}\mathrm{Co}_x\mathrm{Si}$ epilayers. The results above are not exhaustive, there is more to explore and understand the physics behind the B20 $\mathrm{Fe}_{1-x}\mathrm{Co}_x\mathrm{Si}$ epitaxial system.

7.1 Summary

In the early report of Manyala *et al.*, the finding of one electron-like carrier and one μ_B of magnetic moment per Co atom dopant in $\mathrm{Fe}_{1-x}\mathrm{Co}_x\mathrm{Si}$ (at least in the regime $x \lesssim 0.25$) was interpreted as indicating the presence of a fully spin-polarized electron gas [3]. This half-metallic state was retrodicted by band structure calculations a few years later,[33] and its presence explains the greater stability of the magnetic order against pressure for low x samples [96]. Other researchers at University of Leeds previously detected evidence for the partial preservation of this state in non-phase-pure sputtered $\mathrm{Fe}_{1-x}\mathrm{Co}_x\mathrm{Si}$ polycrystalline films.[42]

In the chapter on growth and characterisation, I have shown that high quality, phase pure $\mathrm{Fe}_{1-x}\mathrm{Co}_x\mathrm{Si}$ thin films with varying Co doping were grown on a Si [111] substrate by MBE. In-situ LEED, XRD, TEM, and AFM were used to structurally characterise the films. The films were found to be epitaxial with no visible misfits or defects and with a very low surface RMS roughness ($\sim 1\ nm$), all indicating the high quality of the thin films. Upon further analyses films were found to be biaxially strained, making the unit cell rhombohedral rather than cubic. Nevertheless, the films still retained their phase purity as shown by Bragg peaks obtained from XRD and linear relationship between volume strain and shear strain.

The chapter on magnetic characterisation presented the result of $\mathrm{Fe}_{1-x}\mathrm{Co}_x\mathrm{Si}$ epilayers investigated using SQUID, VSM, soft X-ray spectroscopy, and MFM. One of the significant achievement is the enhancement of ordering temperature of $\mathrm{Fe}_{1-x}\mathrm{Co}_x\mathrm{Si}$ epilayers, upto 77K for $x = 0.4$. The dichroism evolving at both Fe and Co edges, probed by XMCD shows that the magnetic moment is not necessarily localised only on the Co atom as previously reported by Degrave *et al.* [41]. The gradual evolution of dichroism at Fe edge with increasing Fe doping indicates that Fe atoms contribute to net magnetisation of the sample. It is therefore possible that the Co atom magnetises the nearby Fe atom, thereby increasing the net magnetic moment per formula unit. A shift in the resonant peak energy accompanied by evolution of shoulder like structure in the resonant peak of the XAS data indicates a modified band structure in $Fe_{1-x}Co_xSi$ epitaxial system. The spatial ordering parameter of $Fe_{1-x}Co_xSi$ epilayers analysed using the MFM images shows the maximum spatial ordering in the system between 650mT -700mT. Within similar range of applied magnetic field highest topological hall effect was observed by Porter *et al.* [100] in the $Fe_{1-x}Co_xSi$ epitaxial system.

The chapter on transport measurements presented the results obtained by measuring the devices made from $Fe_{1-x}Co_xSi$ thin films patterned with Hall bars. Longitudinal resistivity, OHE, and AHE were measured at 5K. The films exhibit characteristic positive magnetoresistance. From OHE, mobility of the charge carriers and carrier density were extracted. From the temperature dependent resistivity, as expected, the films were found to be metallic for high Co doping ($x \geq 3$) and semiconducting like for lower Co doping ($x \leq 0.25$). Huge anomalous Hall coefficient was determined from AHE.

Also, a set of $Fe_{1-x}Co_xSi$ ($x = 0.2$) thin films with varying thickness (t) were grown using the same protocol as described before in the chapter on growth and characterisation. Structural characterisation of the films by in-plane and out of plane XRD reveal that due to heretoepitaxy the films are biaxially strained as a result of which the unit cell is rhombohedral instead of cubic. The volume strain and shear strain relationship exhibit linearity for the films $t \geq 10$nm. 10nm is perhaps the critical thickness for the epitaxial growth of the films, below which the films may not be phase pure.

Combining the results from magnetometry and Hall transport we see that for $x \gtrsim 0.25$, in the metal-like regime, the behaviour of the $Fe_{1-x}Co_xSi$ film is much as expected: the moment per carrier ratio drops, falling to only about 0.5 for $x = 0.5$. The decrease in the spin-polarization for high x has been previously observed and explained as being due to local disorder in the crystal structure induced by addition of Co atoms.[33; 96]. In the low-doping semiconductor-like regime ($x \lesssim 0.25$), the ratio of moment per carrier exceeds unity, arising from the small shortfall in carriers per Co that was found in the data presented in Fig. 5.5(b), and slight excess moment observed in Fig. 6.4(c). Physically, the underlying mechanism is not clear. A plausible picture might be that there are a low number of Co atoms on Si antisites or in interstitial positions, too few to be readily detected by XRD or HRTEM, that act both as charge traps and possess local moments exceeding 1 μ_B (either alone or by weakly polarizing neighbouring Fe sites). More detailed studies, such as *ab initio* calculations, would be required to confirm this scenario. Nevertheless, it is clear that in this regime, we have a highly-polarized electron gas. Another plausible explanation based on the evolution of magnetism in the system (as probed by XMCD) is that the Co atom induces magnetism in nearby Fe atoms and therefore the moment is not only localised over Co atom but Fe atom too and hence Fe atoms contribute to the total magnetic moment of the film.

To summarize, we have grown a set of $\mathrm{Fe}_{1-x}\mathrm{Co}_x\mathrm{Si}$ epitaxial thin films, and studied the variation in the structural, transport, and magnetic properties in the range $0 \leq x \leq 0.5$. The epilayers are ϵ-phase pure, but with a deformation of the B20 unit cell into an rhombohedral form by the epitaxial strain. Qualitatively, the properties of our epilayer samples are similar in many ways to those of bulk crystals. In particular, we found the metal-insulator transition to lie in the middle of this range, with a high spin-polarization in the semiconducting regime ($x \lesssim 0.25$). However there are quantitative differences, the most important of which is the stabilization of magnetic order up to much higher temperatures than in bulk crystals. The availability of thin films amenable to planar processing techniques is an important step to realising spintronic devices based on the remarkable physics of these B20-ordered materials [44; 49; 92].

7.2 Future Outlook

Since the majority of previous studies on the $\mathrm{Fe}_{1-x}\mathrm{Co}_x\mathrm{Si}$ system have been on bulk systems, there is still a vast scope of opportunity left to investigate the epitaxial $\mathrm{Fe}_{1-x}\mathrm{Co}_x\mathrm{Si}$ system. In this thesis, via epitaxial growth of $\mathrm{Fe}_{1-x}\mathrm{Co}_x\mathrm{Si}$ thin films, variation in doping content of Co we have shown that the biaxial strain brings about significant changes in the system. The strain essentially modifies the band structure, as a consequence of which we observe increased stability in magnetic ordering, and evolution of magnetism on both Fe and Co edges (XMCD) etc. Also, the films retain their full spin polarisation upto a certain Co doping ($x \leq 0.3$). These promising results propels us to investigate more about the system and look for interesting physics.

On the lines of investigating the variation of Co doping in $Fe_{1-x}Co_xSi$ epitaxial system, we still need to thoroughly investigate the thickness dependence of $Fe_{1-x}Co_xSi$ epilayers. The results mentioned above are very promising and highlight the need to pursue the investigations further. The thickness varying films may be patterned into standard Hall bars. It would be interesting to measure OHE, AHE and THE in these thin films. Also, following the protocol by Tian *et al.* [105] one could scale AHE properly, isolate the intrinsic contribution and find whether if it is side jump or skew scattering that dominates in $Fe_{1-x}Co_xSi$ system.

One of the major challenges faced by $Fe_{1-x}Co_xSi$ epilayers is the low ordering temperatures. It is well known that Germanides such as FeGe or FeCoGe have much higher ordering temperatures [47] of the order of 270 K. It would therefore be interesting to dope $Fe_{1-x}Co_xSi$ system with Ge, where Ge would replace Si atom in the unit cell, thereby increasing the ordering temperature of the system.

Another area that needs to be investigated is skyrmions in $Fe_{1-x}Co_xSi$ epilayers. The presence of real space skyrmions in bulk $Fe_{1-x}Co_xSi$ has already been shown by Yu *et al.* [21], and the mechanism of skyrmion formation and annihilation has been shown by Milde *et al.* [79] and Kanazawa *et al.* [99] using MFM and nano structured Hall bars respectively. One can therefore use direct imaging below the ordering temperature to probe the skyrmions in $Fe_{1-x}Co_xSi$ epilayers. One could also perhaps pattern the films into nano sized Hall bar devices of varying sizes and measure THE. The discrete or step wise profile of topological hall resistivity would help to understand the dynamics of skyrmions and demonstrate the emergent magnetic quantum flux associated with each skymion that was previously indistinguishable at a macroscopic level[99]. The aforementioned techniques could further be backed up by band structure calculations and micromagnetic simulations. A better understanding of the physics behind the $Fe_{1-x}Co_xSi$ system would not only help us with the fundamental understanding but also help in implementing them into practical applications in spintronics. Current thin film technology is very advanced, a silicide based fully spin polarised system that is readily integrable with the technology available in the microprocessing industry offers some very promising device physics and opens a broader area of investigation.

REFERENCES

[1] H. Ohno, A window on the future of spintronics, *Nature Mater.* **9**, 952 (2010) 2

[2] A. I. Al-Sharif, M. Abu-Jafar and A. Qteish, Structural and electronic structure properties of FeSi: the driving force behind the stability of the B20 phase, *J. Phys.: Cond. Matt.* **13**, 2807 (2001) 2, 22

[3] N. Manyala, Y. Sidis, J. F. DiTusa, G. Aeppli, D. P. Young et al., Magnetoresistance from quantum interference effects in ferromagnets, *Nature (London)* **404**, 581 (2000) 2, 5, 18, 22, 24, 59, 61, 62, 80, 81, 98

[4] G. Wertheim, V. Jaccarino, J. Wernick, J. Seitchik, H. Williams et al., Unusual electronic properties of FeSi, *Phys. Lett.* **18**, 89 (1965) 2

[5] V. Jaccarino, G. K. Wertheim, J. Wernick, L. Walker and S. Arajs, Paramagnetic excited state of FeSi, *Phys. Rev.* **160**, 476 (1967) 2, 21, 58

[6] Z. Schlesinger, Z. Fisk, H.-T. Zhang, M. B. Maple, J. DiTusa et al., Unconventional charge gap formation in FeSi, *Phys. Rev. Lett.* **71**, 1748 (1993) 2

[7] S. Paschen, E. Felder, M. A. Chernikov, L. Degiorgi, H. Schwer et al., Low-temperature transport, thermodynamic, and optical properties of FeSi, *Phys. Rev. B* **56**, 12916 (1997) 2

[8] J. F. DiTusa, K. Friemelt, E. Bucher, G. Aeppli and A. P. Ramirez, Metal-insulator transitions in the kondo insulator FeSi and classic semiconductors are similar, *Phys. Rev. Lett.* **78**, 2831 (1997)

[9] G. Aeppli and J. F. DiTusa, Undoped and doped fesi or how to make a heavy

fermion metal with three of the most common elements, *Materials Science and Engineering B* **63**, 119 (1999) 2

[10] C. Pfleiderer, S. R. Julian and G. G. Lonzarich, Non-fermi-liquid nature of the normal state of itinerant-electron ferromagnets, *Nature (London)* **414**, 427 (2001) 2, 61

[11] N. Manyala, J. F. DiTusa, G. Aeppli and A. P. Ramirez, Doping a semiconductor to create an unconventional metal, *Nature (London)* **454**, 976 (2008)

[12] R. Ritz, M. Halder, M. Wagner, C. Franz, A. Bauer et al., Formation of a topological non-fermi liquid in MnSi, *Nature (London)* **497**, 231–234 (2013) 2

[13] Y. Onose, N. Takeshita, C. Terakura, H. Takagi and Y. Tokura, Doping dependence of transport properties in $fe_{1-x}co_xsi$, *Phys. Rev. B* **72**, 224431 (2005) 2, 5, 22, 24, 59, 61, 62, 80, 81

[14] N. A. Porter, G. L. Creeth and C. H. Marrows, Magnetoresistance in polycrystalline and epitaxial fe$_1$-$x$co$_x$si thin films, *Phys. Rev. B* **86**, 064423 (2012) 2, 5, 42, 61

[15] J. Beille, J. Voiron, F. Towfiq, M. Roth and Z. Y. Zhang, Helimagnetic structure of the fe x co 1-x si alloys, *J.Phys. F: Metal Phys.* **11**, 2153 (1981) 2, 5, 20

[16] J. Beille, J. Voiron and M. Roth, Long period helimagnetism in the cubic b20 fe x co 1-x si and co x mn1-x si alloys, *Solid State Comm.* **47**, 399 (1983) 20, 61

[17] M. Uchida, Y. Onose, Y. Matsui and Y. Tokura, Real-space observation of helical spin order, *Science* **311**, 359 (2006)

[18] S. V. Grigoriev, D. Chernyshov, V. A. Dyadkin, V. Dmitriev, S. V. Maleyev et al., Crystal handedness and spin helix chirality in fe$_{1-x}$co$_x$Si, *Phys. Rev. Lett.* **102**, 037204 (2009) 2, 5, 21

[19] S. Mühlbauer, B. Binz, F. Jonietz, C. Pfleiderer, A. Rosch et al., Skyrmion lattice in a chiral magnet, *Science* **323**, 915 (2009) 2

[20] W. Münzer, A. Neubauer, T. Adams, S. Mühlbauer, C. Franz et al., Skyrmion lattice in the doped semiconductor $fe_{1-x}co_xsi$, *Phys. Rev. B* **81**, 041203 (2010)

[21] X. Z. Yu, Y. Onose, N. Kanazawa, J. H. Park, J. H. Han et al., Real-space observation of a two-dimensional skyrmion crystal, *Nature (London)* **465**, 901 (2010) 3, 25, 101

[22] P. Milde, D. Köhler, J. Seidel, L. M. Eng, A. Bauer et al., Unwinding of a skyrmion lattice by magnetic monopoles, *Science* **340**, 1076 (2013) 2

[23] M. Lee, W. Kang, Y. Onose, Y. Tokura and N. P. Ong, Unusual hall effect anomaly in mnsi under pressure, *Phys. Rev. Lett.* **102**, 186601 (2009) 2, 63

[24] A. Neubauer, C. Pfleiderer, B. Binz, A. Rosch, R. Ritz et al., Topological hall effect in the *a* phase of mnsi, *Phys. Rev. Lett.* **102**, 186602 (2009) 58, 63

[25] R. Ritz, M. Halder, C. Franz, A. Bauer, M. Wagner et al., Giant generic topological hall resistivity of MnSi under pressure, *Phys. Rev. B* **87**, 134424 (2013)

[26] B. J. Chapman, M. G. Grossnickle, T. Wolf and M. Lee, Large enhancement of emergent magnetic fields in MnSi with impurities and pressure, *Phys. Rev. B* **88**, 214406 (2013) 2

[27] E. Karhu, S. Kahwaji, T. L. Monchesky, C. Parsons, M. D. Robertson et al., Structure and magnetic properties of mnsi epitaxial thin films, *Phys. Rev. B* **82**, 184417 (2010) 2, 3, 46, 80

[28] E. A. Karhu, S. Kahwaji, M. D. Robertson, H. Fritzsche, B. J. Kirby et al., Helical magnetic order in mnsi thin films, *Phys. Rev. B* **84**, 060404 (2011) 2, 3

[29] E. A. Karhu, U. K. Rößler, A. N. Bogdanov, S. Kahwaji, B. J. Kirby et al., Chiral modulations and reorientation effects in mnsi thin films, *Phys. Rev. B* **85**, 094429 (2012) 2, 14, 80

[30] Y. Li, N. Kanazawa, X. Z. Yu, A. Tsukazaki, M. Kawasaki et al., Robust formation of skyrmions and topological hall effect anomaly in epitaxial thin films of MnSi, *Phys. Rev. Lett.* **110**, 117202 (2013) 2, 58

[31] J. Engelke, T. Reimann, L. Hoffmann, S. Gass, D. Menzel et al., Spin–spin correlation length in MnSi thin films, *J. Phys. Soc. Japan* **81**, 124709 (2012) 2, 80

[32] T. Yokouchi, N. Kanazawa, a. Tsukazaki, Y. Kozuka, M. Kawasaki et al., Stability of two-dimensional skyrmions in thin films of Mn1 -x Fe x Si investigated by the topological Hall effect, *Physical Review B* **89**, 064416 (2014) 2, 58, 64, 65, 67, 71, 80

[33] J. Guevara, V. Vildosola, J. Milano and A. M. Llois, Half-metallic character and electronic properties of inverse magnetoresistant $\mathrm{Fe}_{1-x}\mathrm{Co}_x\mathrm{Si}$ alloys, *Phys. Rev. B* **69**, 184422 (2004) 2, 3, 5, 22, 24, 80, 98, 99

[34] L. F. Mattheiss and D. R. Hamann, Band structure and semiconducting properties of FeSi, *Phys. Rev. B* **47**, 13114 (1993) 2, 14, 22

[35] V. Anisimov, R. Hlubina, M. Korotin, V. Mazurenko, T. Rice et al., First-Order Transition between a Small Gap Semiconductor and a Ferromagnetic Metal in the Isoelectronic Alloy FeSi1-xGex, *Physical Review Letters* **89**, 1 (2002) 2

[36] G. Strijkers, Y. Ji, F. Yang, C. Chien and J. Byers, Andreev reflections at metal/superconductor point contacts: Measurement and analysis, *Physical Review B* **63**, 1 (2001) 3

[37] N. Manyala, Y. Sidis, J. F. DiTusa, G. Aeppli, D. P. Young et al., Large anomalous hall effect in a silicon-based magnetic semiconductor, *Nature Mater.* **3**, 255 (2004) 3, 5, 24, 25, 48, 64

[38] N. Manyala, B. D. Ngom, A. C. Beye, R. Bucher, M. Maaza et al., Structural and magnetic properties of epsilon -fe[sub 1 - x]co[sub x]si thin films deposited via pulsed laser deposition, *Appl. Phys. Lett.* **94**, 232503 (2009) 3, 24

[39] Y. Ji, G. J. Strijkers, F. Y. Yang, C. L. Chien, J. M. Byers et al., Determination of the Spin Polarization of Half-Metallic CrO2 by Point Contact Andreev Reflection, *Physical Review Letters* **86**, 5585 (2001) 3

[40] B. Nadgorny, I. I. Mazin, M. Osofsky, R. J. Soulen, P. Broussard et al., Origin of high transport spin polarization in La0.7Sr0.3, *Physical Review B* **63**, 184433 (2001) 3

[41] J. P. Degrave, A. L. Schmitt, R. S. Selinsky, J. M. Higgins, D. J. Keavney et al., Spin polarization measurement of homogeneously doped Fe 1-x Co x Si nanowires by Andreev reflection spectroscopy., *Nano letters* **11**, 4431 (2011) 3, 24, 87, 99

[42] S. A. Morley, N. A. Porter and C. H. Marrows, Magnetism and magnetotransport in sputtered Co-doped FeSi films, *Phys. Status Solidi-R* **5**, 429 (2011) 3, 5, 98

[43] N. Nagaosa and Y. Tokura, Topological properties and dynamics of magnetic skyrmions., *Nature nanotechnology* **8**, 899 (2013) 4, 5

[44] F. Jonietz, S. Mühlbauer, C. Pfleiderer, A. Neubauer, W. Münzer et al., Spin transfer torques in MnSi at ultralow current densities, *Science* **330**, 1648 (2010) 3, 100

[45] B.-C. Min, K. Motohashi, J. C. Lodder and R. Jansen, Tunable spin-tunnel contacts to silicon using low-work-function ferromagnets, *Nature Mater.* **5**, 817 (2006) 5

[46] I. Appelbaum, B. Huang and D. J. Monsma, Electronic measurement and control of spin transport in silicon, *Nature (London)* **447**, 295 (2007)

[47] B. Huang, D. J. Monsma and I. Appelbaum, Coherent spin transport through a 350 micron thick silicon wafer, *Phys. Rev. Lett.* **99**, 177209 (2007) 5, 101

[48] N. S. Kiselev, A. N. Bogdanov, R. Schäfer and U. K. Rößler, Chiral skyrmions in thin magnetic films: new objects for magnetic storage technologies?, *J. Phys. D: Appl. Phys.* **44**, 392001 (2011) 5

[49] A. Fert, V. Cros and J. Sampaio, Skyrmions on the track, *Nature Nano.* **8**, 152 (2013) 100

[50] S.-Z. Lin, C. Reichhardt and A. Saxena, Manipulation of skyrmions in nanodisks with a current pulse and skyrmion rectifier, *Appl. Phys. Lett.* **102**, 222405 (2013) 5

[51] J. M. D. Coey, *Magnetism and Magnetic Materials*, Cambridge University Press ((2010)) 11, 12

[52] J. M. D. Coey and S. Sanvito, Magnetic semiconductors and half-metals, *Journal of Physics D: Applied Physics* **37**, 988 (2004) 13

[53] P. Bak and M. H. Jensen, Theory of helical magnetic structures and phase transitions in MnSi and FeGe, *Journal of Physics C: Solid State Physics* **13**, L881 (2000) 14

[54] M. N. Wilson, *Thesis*, Ph.D. thesis (2013) 15

[55] H. Ohno, a. Shen, F. Matsukura, a. Oiwa, a. Endo et al., (Ga,Mn)As: A new diluted magnetic semiconductor based on GaAs, *Applied Physics Letters* **69**, 363 (1996) 17

[56] a. H. MacDonald, P. Schiffer and N. Samarth, Ferromagnetic Semiconductors: Moving Beyond (Ga,Mn)As p. 37 (2005) 17

[57] T. Dietl, A ten-year perspective on dilute magnetic semiconductors and oxides, *Nature Materials* **9**, 965 (2010) 17

[58] R. S. Selinsky, D. J. Keavney, M. J. Bierman and S. Jin, Element-specific magnetometry of EuS nanocrystals., *Applied physics letters* **95**, 202501 (2009) 17

[59] R. S. Selinsky, J. H. Han, E. a. Morales Pérez, I. a. Guzei and S. Jin, Synthesis and magnetic properties of Gd doped EuS nanocrystals with enhanced Curie temperatures., *Journal of the American Chemical Society* **132**, 15997 (2010) 17

[60] M. J. Bierman, K. M. Van Heuvelen, D. Schmeiß er, T. C. Brunold and S. Jin, Ferromagnetic semiconducting EuO nanorods, *Advanced Materials* **19**, 2677 (2007) 17

[61] Y. Song, A. L. Schmitt and S. Jin, Spin-dependent tunneling transport into CrO2 nanorod devices with nonmagnetic contacts., *Nano letters* **8**, 2356 (2008) 17

[62] F. Carbone, *Spectroscopic signatures of electronic correlations in superconductors and magnets*, Ph.D. thesis (2007) 18, 19, 20

[63] F. Mena, D. V. D. Marel and a. Damascelli, Heavy carriers and non-Drude optical conductivity in MnSi, *Physical Review B* pp. 1–5 (2003) 18

[64] O. Nakanishi, a. Yanase and a. Hasegawa, Electronic energy band structure of MnSi, *Journal of Magnetism and Magnetic Materials* **15-18**, 879 (1980) 18, 19

[65] T. Jeong and W. E. Pickett, Implications of the B20 crystal structure for the magnetoelectronic structure of MnSi, *Physical Review B - Condensed Matter and Materials Physics* **70**, 1 (2004) 18

[66] K. Ishimoto, J. Suzuki, M. Arai and M. Furusaka, Small-angle neutron diffraction from the helical magnet Fe 0.8 Co 0.2 Si **6**, 381 (1995) 20

[67] S. V. Grigoriev, V. A. Dyadkin, D. Menzel, J. Schoenes, Y. O. Chetverikov et al., Magnetic structure of $Fe_{1-x}Co_xSi$ in a magnetic field studied via small-angle polarized neutron diffraction, *Phys. Rev. B* **76**, 224424 (2007) 21, 80, 81

[68] J. Beille, D. Bloch and G. Voiron, The low temperature magnetic behaviour of CeSn2, *Physica B+ C* **20**, 231 (1977) 21

[69] K. Ishimoto, M. Ohashi, H. Yamauchi and Y. Yamaguchi, Itinerant Electron Ferromagnetism in Fe 1- x Co x Si Studied by Polarized Neutron Diffraction (1992) 21, 87

[70] M. Chattopadhyay, S. Roy and S. Chaudhary, Magnetic properties of Fe1-xCoxSi alloys, *Physical Review B* **65**, 3 (2002) 21

[71] M. K. Forthaus, G. R. Hearne, N. Manyala, O. Heyer, R. a. Brand et al., Pressure-induced quantum phase transition in Fe 1-x Co x Si, *Physical Review B* **83**, 085101 (2011) 22, 24

[72] H. Morozumi and H. Yamada, Half metallic state of (Fe,Co)Si with B20-type structure, *Journal of Magnetism and Magnetic Materials* **310**, 1048 (2007) 22, 23

[73] M. Punkkinen, K. Kokko, M. Ropo, I. Väyrynen, L. Vitos et al., Magnetism of (FeCo)Si alloys: Extreme sensitivity on crystal structure, *Physical Review B* **73**, 1 (2006) 22

[74] H. Zhi-Hui, First principles study on the electronic structure and magnetism of Fe1-xCo x Si alloys, *Chinese Physics* **3863** (2007) 22

[75] V. V. Mazurenko, a. O. Shorikov, a. V. Lukoyanov, K. Kharlov, E. Gorelov et al., Metal-insulator transitions and magnetism in correlated band insulators: FeSi and Fe 1-x Co x Si (2010) 24

[76] K. Maex, Simply irresistible silicides, *Physics World* **8**, 35 (1995), cited By 0 24

[77] M. A. Chernikov, E. Felder, S. Paschen, A. D. Bianchi, H. R. Ott et al., Low-temperature magnetic and thermodynamic properties of Fe1-xCoxSi, *Physica B* **230**, 790 (1997) 25

[78] M. Arita, K. Shimada, Y. Takeda, M. Nakatake, H. Namatame et al., Angle-resolved photoemission study of the strongly correlated semiconductor FeSi, *Phys. Rev. B* **77**, 205117 (2008) 25

[79] P. Milde, D. Köhler, J. Seidel, L. M. Eng, A. Bauer et al., Unwinding of a Skyrmion Lattice by Magnetic Monopoles, *Science* **340**, 1076 (2013) 25, 93, 101

[80] P. Kandaswamy, Physique des Materiaux Nanostructures Al (Ga) N / GaN pour la optoelectronique intersousbande dans la infrarouge proche et moyen (2010) 27, 28

[81] J. Als-Nielsen and D. McMorrow, *Elements of Modern X-ray Physics*, John Wiley and Sons, Hoboken, New Jersey (2001) 33, 36

[82] A. Petrova, V. Krasnorussky, A. Shikov, W. Yuhasz, T. Lograsso et al., Elastic, thermodynamic, and electronic properties of MnSi, FeSi, and CoSi, *Physical Review B* **82**, 1 (2010) 43

[83] K. S. J.S. Murray, *Molecular Electrostatic Potentials: Concepts and Applications*, Elsevier (1996) 43, 44

[84] A. R. Denton and N. W. Ashcroft, Vegard's law, *Phys. Rev. A* **43**, 3161 (1991) 46

[85] D. Shinoda, Magnetic properties of Co 1-x Fe x Si, Co1-x Mn x Si, and Fe1-x Mn x Si solid solutions, *Physica Status Solidi (a)* **11**, 129 (1972) 48

[86] R. Karplus and J. M. Luttinger, Hall effect in ferromagnetics, *Physical Review* **95**, 1154 (1954) 56

[87] J. Ye, Y. B. Kim, A. J. Millis, B. I. Shraiman, P. Majumdar et al., Berry Phase Theory of the Anomalous Hall Effect : Application to Colossal Magnetoresistance Manganites (1999) 56

[88] N. P. Nagaosa, Naoto and Sinova, Jairo and Onoda, Shigeki and MacDonald, A. H. and Ong, N. Nagaosa, J. Sinova, S. Onoda, a. H. MacDonald et al., Anomalous Hall effect, *Rev. Mod. Phys.* **82**, 1539 (2010) 57

[89] J. Smit, Spontaneous Hall effect in ferromagnetics, *Physica* **24**, 39 (1958) 57

[90] L. Berger, Side-Jump Mechanism for the Hall Fffect of Ferromagnets, *Physical Review B* **2**, 4559 (1970) 57

[91] G. Yin, Y. Liu, Y. Barlas, J. Zang and R. K. Lake, Topological Spin Hall Effect **024411**, 1 (2015) 57

[92] T. Schulz, R. Ritz, A. Bauer, M. Halder, M. Wagner et al., Emergent electrodynamics of skyrmions in a chiral magnet, *Nature Phys.* **8**, 301 (2012) 58, 100

[93] Y. Taguchi, Y. Oohara, H. Yoshizawa, N. Nagaosa and Y. Tokura, Spin chirality, Berry phase, and anomalous Hall effect in a frustrated ferromagnet., *Science (New York, N.Y.)* **291**, 2573 (2001) 58

[94] N. Kanazawa, Y. Onose, T. Arima, D. Okuyama, K. Ohoyama et al., Large Topological Hall Effect in a Short-Period Helimagnet MnGe, *Physical Review Letters* **106**, 1 (2011) 58

[95] S. X. Huang and C. L. Chien, Extended Skyrmion Phase in Epitaxial FeGe (111) Thin Films, *Phys. Rev. Lett.* **108**, 267201 (2012) 58

[96] M. K. Forthaus, G. R. Hearne, N. Manyala, O. Heyer, R. A. Brand et al., Pressure-induced quantum phase transition in fe$_{1-x}$co$_x$si ($x = 0.1, 0.2$, *Phys. Rev. B* **83**, 085101 (2011) 59, 80, 98, 99

[97] B. Raquet, M. Viret, E. Søndergård, O. Cespedes and R. Mamy, Electron-magnon scattering and magnetic resistivity in 3d ferromagnets, *Phys. Rev. B* **66**, 024433 (2002) 61

[98] N. Nagaosa, J. Sinova, S. Onoda, A. H. MacDonald and N. P. Ong, Anomalous hall effect, *Rev. Mod. Phys.* **82**, 1539 (2010) 63

[99] N. Kanazawa, M. Kubota, A. Tsukazaki, Y. Kozuka, K. S. Takahashi et al., Discretized topological Hall effect emerging from skyrmions in constricted geometry, *Physical Review B* **91**, 1 (2015) 64, 65, 66, 68, 70, 71, 101

[100] N. a. Porter, P. Sinha, M. B. Ward, A. N. Dobrynin, R. M. D. Brydson et al., Giant topological Hall effect in strained Fe 0.7 Co 0.3 Si epilayers pp. 1–7 (2013) 65, 93, 94, 98, 99

[101] G. Binnig, C. F. Quate and C. Gerber, Atomic Force Microscope, *Phys. Rev. Lett.* **56**, 930 (1986) 75

[102] C. Chen, Y. Idzerda, H.-J. Lin, N. Smith, G. Meigs et al., Experimental Confirmation of the X-Ray Magnetic Circular Dichroism Sum Rules for Iron and Cobalt, *Physical Review Letters* **75**, 152 (1995) 78

[103] X. Chen, dependence of semiconductor band gaps, *Energy* pp. 2924–2926 (1991) 82

[104] I. Mínguez-Bacho, S. Rodríguez-López, a. Asenjo, M. Vázquez and M. Hernández-Vélez, Self-correlation function for determination of geometrical parameters in Nanoporous Anodic Alumina Films, *Applied Physics A* **106**, 105 (2012) 92

[105] Y. Tian, L. Ye and X. Jin, Proper scaling of the anomalous hall effect, *Physical Review Letters* **103**, 1 (2009) 101